Evaluating Physical and Biogeochemical Controls on Ocean Oxygen, Nitrate, and Carbon in Coupled Biogeochemical Ocean Circulation Models

Andrew John Margolskee

A dissertation

submitted in partial fulfillment of the

requirements for the degree of

Doctor of Philosophy

University of Washington

2022

Reading Committee:

Curtis A. Deutsch, Chair

Steven R. Emerson

Paul D. Quay

Program Authorized to Offer Degree:

School of Oceanography

University of Washington

Abstract

Evaluating Physical and Biogeochemical Controls on Ocean Oxygen, Nitrate, and Carbon in Coupled Biogeochemical Ocean Circulation Models

Andrew John Margolskee

Chair of the Supervisory Committee:

Curtis A. Deutsch

School of Oceanography

The balance of ocean physics and the photosynthetic production and respiratory consumption of O_2 dynamically links oxygen, organic carbon, and nitrate in the ocean. This thesis uses coupled biogeochemical ocean circulation models to explore the physical and biogeochemical controls on the ocean O_2 cycle and its connections to surface nitrate and organic carbon in climate sensitive regions where these mechanisms have not previously been fully characterized. In the North Pacific Oxygen Deficient Zone (Chapter 2), I demonstrate that the physical supply of O_2 is controlled by three processes: the injection of O_2 along its poleward edge by zonal jets, an indirect O_2 supply from Tropical Instability Waves that induce a meridional O_2 supply that is observable as high [O_2] water impinges on the equatorward Oxygen Deficient Zone boundary and a coastal diffusive seasonal O_2 flux. In the North Atlantic, I leverage historical hydrographic data and a hindcast configuration of the Community Earth System Model to show that the historical variability in O_2 that exceeds that expected from temperature-dependent solubility is

explained by the enhancement of growth rates at higher temperatures. Finally, using a high-resolution model of the tropical Pacific (Chapter 4), I demonstrate that a net organic carbon sequestration of 3 mol C m^{-2} yr^{-1} is narrowly constrained by empirical nitrate data. I further show that there are significant regional differences in the fraction of respired carbon production in the tropical Pacific: greater than 5 times more integrated respiration occurs below the depth horizon where water parcels reach the surface in $\leq$2 years in the eastern equatorial Pacific compared to the western equatorial Pacific.

TABLE OF CONTENTS

List of Figures iii

Chapter 1 Introduction 1

Chapter 2 Ventilation Pathways for the North Pacific Oxygen Deficient Zone 5

2.2 Methods 9

2.3 Results 12

2.4 Discussion 21

2.5 Figures 25

Chapter 3 Climatic Changes in North Atlantic O_2 Amplified by Temperature Sensitivity of Phytoplankton Growth 42

3.1 Introduction: 43

3.2 Conceptual Model 45

3.3 Methods 48

3.4 Results 50

3.5 Discussion 60

3.6 Figures 63

Chapter 4 The Strength and Efficiency of the Biological Carbon Pump in the Tropical Pacific . 78

4.1 Introduction 80

4.2 Equatorial Circulation Dynamics 82

4.3 Methods 84

4.4 Results: Part I 91

4.5 Results: Part II 96

4.6 Discussion 102

4.7 Figures 105

4.8 Supplemental Discussion 124

Bibliography 127

LIST OF FIGURES

Figure 2.1. Model comparison to 2013 World Ocean Database (WOD13) O_2 data..... 25

Figure 2.2. Sample [O_2] time series along an Argo float track (float #5901463) and in ROMS.. 26

Figure 2.3. SOM distribution and characteristics in the Eastern Tropical Pacific..... 28

Figure 2.4. Zonal velocity transects at 150°W in ROMS output and Argo float data..... 30

Figure 2.5. Water parcel entry to the ODZ, based on reverse Lagrangian particle tracking. 32

Figure 2.6. The Eulerian O_2 budget in the ROMS ODZ, defined as the region with 5-year mean [O_2] ≤ 5 mmol m^{-3}..... 34

Figure 2.7. The decomposition of O_2 transport into the mean advective O_2 flux ($\nabla \cdot u O2$) and the time-varying eddy flux ($\nabla \cdot u' O2'$).. 36

Figure 2.8. Hovmöller diagram of the seasonal evolution of vertical O_2 distribution, diffusive fluxes, and biological source-sink at a representative location along the eastern boundary of the ODZ (93°W and 15°N) 38

Figure 2.9 Long-range sources of ODZ water back-tracked to boundaries at 30°N and 30°S..... 40

Figure 2.10. The three-dimensional structure of ODZ ventilation 41

Figure 3.1. Conceptual model of the O_2 content in deep water 63

Figure 3.2. The interannual variability of oxygen and temperature in the subpolar North Atlantic..... 64

Figure 3.3. The mechanisms that drive variability in deep preformed O_2 in the subpolar North Atlantic..... 65

Figure 3.4. The spatial and temporal variability of the correlation between nitrate and temperature in the subpolar North Atlantic 67

Figure 3.5. Accounting for ΔO_{2res} with ΔN_{pre} and surface nitrate.. 69

Figure 3.6. Reynolds decomposition of 100-700m annual ΔN_{pre}. 71

Figure 3.7. The ecological driving mechanism of the enhanced spring bloom during warm years 73

Figure 3.8. Subpolar North Atlantic variability correlated with the North Atlantic Oscillation (NAO).. 74

Supplemental Figure 3.1. Number of observations available in the top 0-1000m in the World Ocean Database 2018 for oxygen and nitrate.. 76

Supplemental Figure 3.2. The component of the Reynolds decomposition that corresponds to the annual 100-700m Δf 77

Figure 4.1. Zonal mean net primary productivity in CMIP5 ocean models and two satellite algorithms. 105

Figure 4.2. Annual mean surface characteristics in the equatorial Pacific based on World Ocean Atlas 2018 data.. 106

Figure 4.3. Conceptual model for the tropical Pacific carbon cycle for the full model domain..106

Figure 4.4. Constraining NCP in ROMS with observed NO_3 and $\%O_2$ supersaturation in the World Ocean Atlas 2018 (WOA18). 108

Figure 4.5. The relationship between air-sea CO_2 flux and NCP (mol C m^{-2} yr^{-1}) over the whole model domain (140°E-80°W, 15°S-15°N)..... 109

Figure 4.6. Zonally averaged NCP_{MLD} and NCP_{comp}. NCP_{comp} and NCP_{MLD} are calculated as annual rates $\int_0^{z_{comp}} r_{C:O} J_{O2} dz$ and $\int_0^{z_{MLD}} r_{C:O} J_{O2}\, dz$ where $r_{C:O}$ is the carbon to oxygen Redfield ratio in ROMS-BEC (1.2821) and J_{O2} is the net ecosystem production of O_2. 111

Figure 4.7. Average time that it takes for particles to reach the mixed layer. 112

Figure 4.8. Annual mean ΔDIC *(*$DIC_{bio} - DIC_{abio}$*)* after 30 years. 113

Figure 4.9. The cumulative column integral of J_{DIC*} ($\int_\infty^z J_{DIC*}\, dz$) evaluated at depths from 0-500m.. 114

Figure 4.10. The relative rate and fraction of respired carbon production below the 1-year sequestration timescale horizon. 115

Figure 4.11. The relative fractions of production and consumption of DIC and DOC. 116

Figure 4.12. The amount of respired carbon production that remains out of contact with the atmosphere on timescales of 0 to 2 years..... 117

Supplemental Figure 4.1. : Temperature in ROMS compared to observations 1198

Supplemental Figure 4.2. NO_3 and temperature at 110°W within 5° north and south of the equator from the surface to 250m. 119

Supplemental Figure 4.3. The fraction of particles that reach the mixed layer in 2 years or less. 120

Supplemental Figure 4.4. The rate of net respired carbon production in mol C m^3 s^{-1} (J_{DIC*}, where J_{DIC*} is J_{DIC} in net heterotrophic water). 121

Supplemental Figure 4.5. The relative rate and fraction of respired carbon production below the 2-year sequestration timescale horizon. 122

Supplemental Figure 4.6. The distribution of [DOC] in the tropical Pacific in ROMS. 123

DEDICATION

My dissertation work has been supported through NSF (OCE-1458888, OCE-1737080) and through the University of Washington School of Oceanography GSFEI. My work was possible because of the availability of high-performance computing support from Yellowstone (ark:/85065/d7wd3xhc) and Cheyenne (doi:10.5065/D6RX99HX) provided by NCAR's Computational and Information Systems Laboratory, sponsored by the National Science Foundation.

Without my two advisors, Steve Emerson and Curtis Deutsch, this work would not have been possible. Bouncing back and forth between the two of them was fun, rewarding, and scientifically fruitful even when (and sometimes especially when) they pulled me in different directions. I'm glad I had the chance to work at the interface of empirical data analysis and modeling work. I'll always be surprised by how much I've learned to be able to do in "15 minutes".

The members of my committee, Paul Quay and Steve Riser, have always been supportive and helpful scientifically. Conversations involving all four members of my committee always ended with me coming away feeling like I'd gleaned a new perspective on my own work and its broader context. Paul's insights in one on one conversations are always challenging and I'm glad I had the chance to work alongside everyone on my committee.

Hartmut Frenzel was my lifeline throughout my entire PhD. I sometimes joke that I've learned 80% of what I know about coding from him. The joke is that it's really more like 90%. It's hard to imagine having been able to do any of this work without Hartmut and his tireless effort to

help me at almost any hour. I never would have guessed that I'd be so lucky to have someone like Hartmut around to answer whatever questions I had, whether they were inane or surprisingly complicated. I just hope I've gotten a little closer to his level of technical wizardry after the years I spent peeking over his shoulder. Thanks for all the cake!

My collaborators Taka Ito and Matt Long were crucial to the third chapter of my dissertation and provided CESM-LE output and guidance, along with comprehensive edits and suggestions.

My graduate cohort is full of fantastic scientists and great friends. My office mate, Isaiah Bolden, was always supportive, hilarious, and insightful, whether the conversation was about science or pretty much anything else. The happy hours with Megan Duffy while we crunched through the last bits of our dissertations were great for keeping my head above water and I'm glad to have made such good friends in this program. I'd like to thank my group of educationally-minded colleagues who worked together with me to spend some of our extracurricular time on redesigning curricula – Rosalind Echols, Theresa Whorley, Sasha Seroy, and Christina Renee Miller. The sense of camaraderie from this group and the rest of the graduate students in UW oceanography made me feel like I was never alone.

Lastly, my friends and family have always supported and believed in me. The nights on the phone or typing away on her couch with Tori helped me stay sane. There's nothing quite like always having a famous comedienne to cheer me up and make me laugh.

Chapter 1

INTRODUCTION

The phytoplankton in the ocean are responsible for roughly half of global photosynthesis (Field et al., 1998) and fix 50 Gt C per year. The net production of organic matter by phytoplankton is linked to net O_2 production by photosynthesis in the surface ocean and net O_2 consumption below the euphotic zone, where remineralization of sinking organic matter consumes O_2. During organic matter production, nutrients (such as nitrate) and dissolved inorganic carbon (DIC) are incorporated into organic matter, which can be transported to the deep primarily via sinking particulate organic matter. The release of dissolved inorganic nitrate and carbon during the remineralization of organic matter is stoichiometrically related to respiratory O_2 consumption. This process is often referred to as the biological pump because it results in a net transport of surface nutrients and CO_2 to the deep. The biological pump therefore is a major control on nutrient concentrations in the surface ocean as well as O_2 and dissolved inorganic carbon concentrations in the deep.

The O_2 concentration of a water parcel at an arbitrary location below the surface ocean is a function of its age and the accumulated impact of respiratory O_2 depletion since the last time it was at the surface. In areas where high rates of organic matter production in the surface ocean overlie old water with slow ventilation rates, such as along eastern boundary upwelling system, low oxygen concentrations are maintained in large regions of each ocean basin. The most intense of these low O_2 regions are referred to as Oxygen Deficient Zones (ODZs; $[O_2] < 5$ mmol m^{-3}) and they have historically been poorly represented in ocean models (Cabre et al., 2015). In chapter 2, I show results from a high-resolution coupled physical/biogeochemical ocean model (the Regional

Ocean Modeling System, ROMS; Shchepetkin & McWilliams, 2005) that quantify the supply pathways of O_2 to the large ODZ located in the North Pacific.

Roughly half of the horizontal supply of O_2 to the ODZ can be attributed to oxygen intrusions at depth (termed Secondary Oxygen Maxima) that penetrate the core of the ODZ and are the result of the shear between two zonal currents that are only resolved in high resolution models. The Northern Equatorial Undercurrent Jets (Cravatte et al., 2017; Firing et al., 1998; Qiu et al., 2013; Tsuchiya, 1975) supply an additional 25%, while seasonal upwelling-downwelling cycles along the eastern boundary account for the remainder. To my knowledge, the eddy-driven O_2 supply that is characterized by Secondary Oxygen Maxima has not been reported previously.

Marine O_2 is expected to decline in the future as the climate warms. The physical mechanisms that drive future deoxygenation in a warmer climate are reduced oxygen solubility and enhanced stratification, which inhibits ventilation of the interior ocean. Changes in gas solubility are straightforward to predict and models agree on the sign of the stratification-induced changes in ocean ventilation. However, models disagree on the sign of the response of the ocean's biological systems to warming temperatures and the regional response to deoxygenation (Bopp et al., 2013; Deutsch et al., 2011; Gnanadesikan et al., 2012).

In chapter 3, I evaluate the historical response of thermocline O_2 to changes in temperature in the subpolar North Atlantic, a region responsible for mode water formation. Using historical trends and a hindcast configuration of the Community Earth System Model, I demonstrate that during warmer periods in the past 50 years, enhanced nutrient depletion accounts for up to 40% of the historical oxygen response to changes in temperature. Historical annual oxygen variability (ΔO_2) can be fully accounted for by the combination of $\Delta O_{2\mathrm{pre}}$ and $\Delta O_{2\mathrm{res}}$, which are the variability in preformed O_2 and respired O_2, respectively. $\Delta O_{2\mathrm{pre}}$ can be calculated directly in

CESM by using an O_{2pre} tracer and it accounts for 60% of historical O_2 variability. By leveraging historical nitrate variability(ΔN_{surf}) and an N_{pre} tracer in CESM, we show that the remainder of the historical oxygen variability ΔO_{2res} can be accounted for by variability in ΔN_{pre}. I demonstrate that the historical N_{pre} variability is controlled by variability in surface nitrate and not variability in endmember mixing of different water fractions. Surface nitrate is a fingerprint for of climatic oxygen variability on interannual timescales in the subpolar North Atlantic. Ultimately, the enhanced drawdown of nitrate in warm years is driven by enhanced growth rates at warmer temperatures. Even though the relative changes in growth rates are quite small (2.1%-5.7% for a ΔT of 5% at 10^{o}C), the exponential nature of phytoplankton growth drives significant changes in total biomass accumulation during the growing season.

In chapter 4, I combine empirical observational data of nitrate and $\%O_{2sat}$ to constrain net community production in a tropical Pacific configuration of ROMS with a 25km resolution with model boundaries at 15^{o}N and 15^{o}S and climatological forcing. I also conducted extensive sensitivity tests with various ecosystem parameters (e.g. the degradation timescale of dissolved organic matter, the half saturation constant of iron uptake, the maximum growth rate of phytoplankton, etc.) in order to produce a simulation that falls within the observational constraints. I show that a carbon sequestration of 3 mol C m^{-2} yr^{-1} in the tropical Pacific is necessary in ROMS to match the observed nitrate distributions.

The amount of carbon that remains sequestered (i.e. away from the atmosphere) is a matter of timescale. To evaluate how much carbon is sequestered in the tropical Pacific, I used Lagrangian particle tracking experiments to evaluate how long it takes for water in the top 500m of the model to reach the surface. Particles were tracked for up to 2 years and were used to define depth horizons that correspond to particle upwelling timescales. For example, if water parcels at 100m on average

took 1 year to reach the mixed layer anywhere along their path, then 100m is the 1-year timescale horizon (τ_z^{1yr}). Up to 77% of respired carbon production in the western equatorial Pacific is above τ_z^{2yr} and is therefore unlikely to contribute to carbon sequestration on long timescales. In contrast, as much as 63% of respired carbon production occurs below τ_z^{2yr} in the eastern equatorial Pacific, which is a carbon flux of 3.4 mol C m^{-2} yr^{-1}. I show that these regional differences can be explained by 1) differences in regional respired carbon production: the east in general has more organic matter production and therefore a higher particulate organic carbon flux and 2) differences in circulation: despite more rapid upwelling rates in the eastern Pacific, deeper mixed layers and a deeper core of the EUC conspire to bring water parcels carrying respired carbon to the surface more quickly in the west than in the east below 100m.

The work described in this dissertation uses various combinations of many chemical tracers (e.g. preformed and regenerated oxygen and nitrate, carbon, etc.) with physical tracers (e.g. dye and particle tracking experiments, temperature, etc.) to evaluate the underlying mechanisms that control the biogeochemical cycles of carbon, nitrate, and oxygen in the low latitude Pacific and high latitude North Atlantic oceans. I set out to understand the mechanisms that control regions of the ocean that have a profound impact on O_2, carbon, and nitrogen biogeochemistry. I hope that this work helps to shed a bit of light on the role of physics and biogeochemistry in controlling the ocean's mean state (chapters 2 & 4), as well as its response to changing temperature (chapter 3).

Chapter 2

VENTILATION PATHWAYS FOR THE NORTH PACIFIC OXYGEN DEFICIENT ZONE

Abstract

Oxygen deficient zones (ODZs) in the tropical ocean exert a profound influence on global biogeochemical cycles, but the factors that regulate their long-term structure and sensitivity to oceanic change remain poorly understood. We analyzed hydrographic observations and a high-resolution physical/biogeochemical model to diagnose the primary pathways that ventilate the tropical Pacific ODZs. Historical and recent autonomous observations reveal pronounced and widespread O_2 peaks, termed Secondary Oxygen Maxima (SOMs), within the depths of the broader O_2 minimum layer, especially at the equatorward edge of both northern and southern ODZs. In the northern ODZ, Lagrangian particle tracking in an eddy-permitting numerical model simulation attributes these features to intrusions of the Northern Subsurface Countercurrent (NSCC) along the equatorial edge of the ODZ. Zonal subsurface jets also ventilate the poleward edge of the northern ODZ but induce a smaller O_2 flux and do not yield detectable SOMs. Along the ODZ's eastern boundary, oxygenation is achieved by the seasonal cycle of upwelling of low-O_2 water onto the continental shelf, followed by downwelling of O_2-replenished near-surface waters back into the ODZ. Waters entering the northern Pacific ODZ originate from the extra-tropics in both hemispheres, but two thirds are from the southern hemisphere and arrive later and with a wider range of transit times. These results suggest that predicting future changes in the large Pacific ODZs will require a better understanding of the narrow zonal jets and seasonal dynamics of coastal upwelling that supply their O_2.

2.1 Introduction

The availability of dissolved O_2 is a key metabolic constraint for marine ecosystems, restricting habitat of aerobic animals (Wishner et al., 2018), while favoring anaerobic microbial metabolisms when O_2 concentrations are low (Lam et al., 2009; Kondo & Moffett, 2013; Penn et al., 2016; Ward et al., 2009). The large-scale O_2 distribution of the ocean interior is driven by the subduction of waters from the surface ocean and the subsequent consumption of O_2 via respiration of organic matter. The accumulated O_2 removal by heterotrophic respiration leads to strongest O_2 depletion in the Oxygen Minimum Zones (OMZs) found throughout the Pacific, Atlantic, and Indian Oceans at thermocline depths of 100-1000m. The OMZs vary in size, intensity, and depth, but generally reach their lowest [O_2] and shallowest depths in tropical upwelling regions where thermocline waters have been isolated from the atmosphere for the longest time.

The cores of the most intense tropical OMZs have concentrations of O_2 that reach levels low enough to slow or inhibit the aerobic microbial metabolisms that dominate the ocean's respiration. We define Oxygen Deficient Zones (ODZs) as that part of the broader OMZ in which [O_2] <5 mmol m^{-3}, a value chosen because it is low enough to induce anaerobic microbial metabolism (e.g. Devol, 1978; Kalvelage et al., 2011) and high enough to be mapped in climatological data. The ODZs occupy only 0.35% of the ocean (Karstensen et al., 2008) but have an outsized impact on global biogeochemical cycles. The ODZs regulate the global inventory of bioavailable nitrogen by removing ~50% of the ocean's N via denitrification and anammox (DeVries, et al., 2013; DeVries et al., 2012). The low O_2 regions in and around ODZs account for about half of marine N_2O production, a potent greenhouse gas whose net production could respond strongly to climate change (Codispoti, 2010). The ODZs also represent a source of redox-sensitive

trace metals like dissolved ferrous iron (*d*Fe(II)), due to the lack of oxidant in low [O_2] waters (Heller et al., 2017; Kondo & Moffett, 2013).

The OMZs, and especially the ODZs, exhibit both highly sensitive and variable climate responses, resulting in an uncertain future for marine nitrogen cycling and metal redox cycling (Deutsch et al., 2011; Gnanadesikan et al., 2013). Uncertainty in future projections of low O_2 regions is reflected in the difficulty that existing climate models have in accurately reproducing the 3-D spatial structure of O_2 in the Eastern Tropical Pacific, where most of the suboxic waters are currently found. Although observations reveal two distinct hypoxic zones separated by the equator, many ocean models produce an OMZ that spans the entire eastern tropics (Figure 1; see also Cabré et al., 2015). These model biases reflect the sensitivity of low O_2 regions to numerous biological influences, including microbial community structure (Penn et al. 2016), organic matter stoichiometry (DeVries & Deutsch, 2014) and the depth scale of its remineralization (Cram et al., 2018; Van Mooy et al., 2001). Physical processes that ventilate the OMZs, including strong zonal circulation (Aumont et al., 1999; Dietze & Loeptien, 2013; Duteil, et al., 2014) and associated isopycnal stirring (Getzlaff & Dietze, 2013; Gnanadesikan et al., 2013) are also poorly represented in coarse global resolution models. The response of ODZs to climate change is likely to be governed by the relatively small residual of compensating physical and biological mechanisms within the tropics (Gnanadesikan et al., 2012; Ito & Deutsch, 2013), as well as extra-tropical climate forcings, including wind and buoyancy driven ventilation changes in mid-latitudes (Takano et al., 2018).

The subsurface circulation in the Eastern Tropical Pacific is dominated by alternating zonal currents that are well documented in the literature (Cravatte et al. 2017; Firing et al., 1998; Qiu et al., 2013; Tsuchiya, 1975). Among the subsurface currents of potential importance to the eastern

tropical ODZs, the Equatorial Undercurrent is the best studied and is considered a source of water and O_2 to Pacific ODZs on both sides of the equator (Toggweiler, et al., 1991). The Northern Subsurface Countercurrent at 5°N (NSCC) has also been shown to be a source of O_2 to the Eastern Tropical Pacific (Stramma et al., 2010). However, both of these eastward-flowing currents are too far equatorward to directly ventilate either of the ODZs. Thus, the physical processes by which O_2 is supplied to even the world's largest ODZ, in the Eastern Tropical North Pacific (ETNP), remain poorly understood.

We investigated the ventilation of the Eastern Tropical Pacific using a combination of observations and numerical model simulations. Using data from Argo floats and the World Ocean Database, we document the existence of high O_2 anomalies within the OMZs and describe the distribution, magnitude, and frequency of these Secondary Oxygen Maxima (SOMs) throughout the Eastern Tropical Pacific. Using Lagrangian particle tracking in an eddy-permitting ocean circulation model, we demonstrate that these SOMs reflect the major role of zonal deep jets in ventilating the northern ODZ at its open ocean boundaries. We compute the supply of oxygen throughout the northern ODZ, revealing distinct mechanisms of ODZ ventilation acting along each of its equatorial, subtropical, and eastern boundaries. By tracking ODZ water parcels back to their extra-tropical origins, we find that the Southern Hemisphere accounts for up to two thirds of water entering the northern ODZ on multi-decadal timescales, while the Northern Hemisphere exerts a more pronounced short-term influence on ODZ source waters with characteristic transit times of 30 years or less.

2.2 Methods

2.2.1 Hydrographic Observations

Hydrographic profiles with O_2 obtained from the 2013 World Ocean Database (hereafter WOD13, Boyer et al., 2013) and Argo floats were first binned onto a regular grid (Figure 2.1). A typical open ocean O_2 profile in the eastern Pacific has high [O_2] at the surface, intermediate values in deep water, and a minimum at thermocline depths (~200-1000m) due to the cumulative effect of respiration. However, we also find that within the depths of the O_2 minimum zone, peaks of high [O_2] are also present. These pronounced secondary oxygen maxima (SOMs) are commonly found at a depth of about 250m in the Eastern Tropical Pacific in both Argo float data and ROMS model output (Figure 2.2a and 2.b). While typical oceanic O_2 profiles are characterized by a positive curvature (i.e. second derivative) in [O_2] versus depth, profiles with SOMs will have curvature that changes sign from positive near the surface to negative in some depth interval (Figure 2.2c).

We mapped the frequency, magnitude, and distribution of SOMs in the eastern Pacific by identifying individual profiles that exhibit alternating second derivatives in the WOD13 database (Figure 2.3a and b). We define SOMs as O_2 features within the density range of 1026-1027.5 kg m^{-3}. A SOM is considered detectable only if the O_2 anomaly is at least 5 mmol O_2 m^{-3} above background [O_2], calculated as the linear interpolation between the local minima above and below each SOM (Figure 2.3c and d). We only consider 1° by 1° grid cells with binned [O_2] profiles in at least 3 months in the WOD13 time period (1955-2013). An identical procedure is applied to model simulated data (see below).

2.2.2 Ocean Model

To better understand the pathways and fluxes of O_2 to the ODZ, we use an eddy-permitting Regional Ocean Modeling System (ROMS, Shchepetkin & McWilliams, 2005) with an embedded ecosystem model (BEC, Moore et al., 2004). The model has been extensively validated against numerous observations in the eastern North Pacific (Durski et al., 2017; Renault et al., 2016). The model domain covers the whole Pacific north of ~40°S, with a horizontal resolution of 25 km and 32 vertical sigma levels. The ecosystem model has three functional groups of phytoplankton (small phytoplankton, diatoms, and diazotrophs), with multiple growth-limiting nutrients (nitrate, phosphate, ammonium, silicate, and iron), zooplankton grazers, and an implicit particle flux (Armstrong et al., 2002). The boundary conditions are from Simple Ocean Data Assimilation (Carton & Giese, 2008) and the World Ocean Atlas 2013 (WOA13, Garcia et al., 2014) for biogeochemical tracers. Monthly climatological surface winds and buoyancy forcing are from CORE2 reanalysis (Large & Yeager, 2004). The model is run for 20 years, until the ODZ volume reaches a steady state.

To evaluate the model's ability to reliably depict and quantify ODZ ventilation, we compared the two critical distributions - velocity and O_2 - to observations in the eastern tropical Pacific. The distribution of OMZ water becomes increasingly uncertain as the O_2 threshold of interest falls below ~10 uM. We therefore compared the observed and simulated pattern of waters with $[O_2] \leq 30$ mmol m^{-3}, which reveals distinct OMZs on either side of the equator but is relatively free of biases. The boundary of the model OMZ is in very good agreement with the observations (Figure 2.1), with distinct OMZ lobes north and south of the equator. Because the ODZs are not spatially or temporally well resolved in climatological data, we evaluated model ODZs by computing annual mean ODZ volume in WOA13, with and without the linear empirical correction

of Bianchi et al. (2012). The estimated volume for the North Pacific ODZ is 6.9-16.8 x 10^{14} m^3 and the South Pacific ODZ is 4.7-14 x 10^{13} m^3. The ROMS ODZs are 50% larger than the calibrated WOA13 estimates in the Northern Hemisphere, an apparent bias that is smaller than the uncertainty in the empirical estimate. The bias in the Southern Hemisphere is larger, but the volume estimate from gridded data there is even more uncertain (Paulmier & Ruiz-Pino, 2009).

The close correspondence between the observed and simulated boundaries of the OMZ suggests that the model reproduces the circulation that ventilates these water masses. To directly evaluate the model circulation at locations relevant to the eastern tropical ODZs, we examined the meridional and depth structure of alternating zonal jets in the North Pacific, which have been recently estimated using Argo data (Qiu et al., 2013). The observed location and structure of deep zonal jets is well represented in ROMS (Figure 2.4), although the absolute magnitude of each zonal jet is somewhat weaker than in observations.

2.2.3 Lagrangian Particle Tracking

To track the near-field and far-field origins of northern ODZ water, we computed water parcel trajectories in an offline Lagrangian particle tracking model, Pyticles (Gula et al., 2014). Pyticles uses a 4th-order Runge-Kutta scheme to calculate the 3D advection of massless and dimensionless particles. The position (*P*) of a water 'particle' at time *i+1* is computed from its position and velocity at time *i*:

$$P(x,y,z)_{i+1} = P(x,y,z)_i + \vec{u}(x,y,z)_i * dt \qquad (2.1)$$

where $\vec{u}(x,y,z)$ is the interpolated 3D velocity, $P(x,y,z)_i$ and $P(x,y,z)_{i+1}$ are the initial and final particle positions for each internal timestep (*dt*) of 120 seconds. The interpolation scheme

used to calculate velocities uses both past and future velocities from 5-day archived flow fields to calculate more accurate velocities at the time that the particle position is updated.

Because we are interested in how waters get into the ODZ, we tracked particles backwards in time by flipping the sign of the *dt* term in Equation 2.1 and reversing the order of input velocity time series. Using reverse tracking, we seed every grid cell along the outer perimeter of the ODZ with one particle each (for a total of 17214 particles) and then trace water parcels supplying the ODZ back to the region of their origin. The ODZ perimeter used for particle seeding corresponds to the outermost model grid cells that have a time mean $[O_2] \leq 5$ mmol m^{-3}. Particles released in each month for a year (for a total of 206,568 particles), did not yield qualitatively different trajectories, thus our results are shown independent of the time of release.

2.3 Results

2.3.1 Secondary Oxygen Maxima

To investigate the mechanisms that ventilate the subtropical Pacific OMZs, we analyzed observations from gridded historical hydrocasts and profiling floats (see Section 2.1). To search for features indicative of O_2 ventilation, we first investigated Argo profiles, because their high vertical and temporal resolution can capture small-scale features. Vertical $[O_2]$ profiles captured by Argo floats in both the Eastern Tropical North Pacific (ETNP) and Eastern Tropical South Pacific show pronounced secondary O_2 maxima that occur at 200-250m (σ = ~1026.5 kg m^{-3}, ETNP float shown in Figure 2.2a). While Argo floats provide excellent temporal coverage, the spatial coverage of Argo floats is inadequate to trace the origin and extent of these features.

To evaluate the frequency, amplitude, and spatial distribution of SOMs, we searched for these features in historical observations in WOD13. SOMs are abundant along equatorward boundaries of both ODZs (Figure 2.3a) at potential densities of ~1026.5 kg m^{-3}. The existence and

persistence of SOMs implies that there is enhanced lateral ventilation at this density especially associated with the off-equatorial zonal jets, which drives dynamic mid-depth O_2 variability even in the ODZs. In contrast to the equatorward boundaries, SOMs are largely absent from the poleward edges of both Pacific ODZs. In the South Pacific, SOMs appear at the density of Antarctic Intermediate Water (~1027.1 kg m^{-3}) in both ROMS and WOD13 and indicate the presence of recently ventilated water from the surface outcrop. The few coastal SOMs present in the northern ODZ may be caused by subducted mode water eddies that carry anomalously high O_2 into the region. SOMs in the eastern Pacific therefore fall into three general categories: 1) SOMs associated with the equatorial current system that are abundant between 10°N and 10°S, 2) SOMs associated with Antarctic Intermediate Water in the Southern Hemisphere, and 3) coastal SOMs possibly associated with eddy-induced subduction of near-surface O_2.

The distribution and frequency of SOMs in the model simulations is consistent with the patterns detected in the historical hydrographic data (Figure 2.3a and b). In both model and observations, SOMs span the entire equatorward boundary of the northern ODZ and profiles with no SOMs are primarily located north of 10°N as well along the eastern edge of the basin south of 10°N. SOMs near the continent rarely occur in ROMS, but these coastal features may require a higher resolution model to capture eddy generation and subduction off the shelf (Frenger et al., 2018). There is an eastward intensification of SOM frequency and SOM magnitude in ROMS, but it is difficult to see this trend in the observations, given the number of profiles available in WOD13 (Figure 2.3a-d). We cannot rule out the possibility that the model produces SOMs in areas that the real ocean does not have them (e.g. the region bounded by 115°W, 100°W, 0°N, and 10°N). However, given that SOMs are not permanent features, and in light of data sparseness, the apparent differences between model and observations may not be significant.

The presence of SOMs along the southern boundary of the northern ODZ suggests that the lateral ventilation mechanism of interest is associated with an oxygenated current at its equatorward edge. This is consistent with previous studies that identify the Northern Subsurface Countercurrent (NSCC) as a major source of O_2 to the Eastern Pacific (Stramma et al., 2010). The distinct lack of SOMs along the ODZ's northwestern edge highlights a difference in the mechanisms that control circulation and O_2 supply in the two open boundaries. Furthermore, the symmetry of the SOM distribution around the equator between 10°S and 10°N suggests that they contribute to ODZ ventilation in both hemispheres in both WOD13 and ROMS. However, we focus the remainder of our analysis of the northern ODZ.

2.3.2 Water Parcel Trajectories to the Northern ODZ

We use Lagrangian particle tracking to identify all ventilation pathways that carry water into the northern ODZ, regardless of whether they are associated with SOMs. For a complete diagnosis of the regions that supply water to the ODZ, we defined four simple planar boundaries (Figure 2.5a): 1) the northwestern boundary, a plane stretching from the surface to the bottom (2000m) from the continent at 23°N to the southwestern tip of the ODZ, 2) the top (50m), 3) the bottom (2000m), and 4) the southern boundary (8°N, 85°W-160°W). We tracked particles seeded along the outer perimeter of the ODZ backward in time until they reached any of these predefined boundaries. When a particle crossed any boundary for the first time, the boundary crossing location was stored, and the particle was considered to be outside of the ODZ. Only 1.6% of particles entered the ODZ vertically from either the top (1.2%) or the bottom (0.4%). Approximately 70.8% of particles entered from the southern boundary (Figure 2.5c) via the Northern Subsurface Countercurrent (NSCC) and 27.6% entered from the northwestern boundary (Figure 2.5b) via the North Equatorial Undercurrent Jets (NEUC jets) at 13°N and 16°N. The dominant sources of water

to the northern edge of the ODZ occur south of 18°N, with a small (2%) portion entering along the eastern boundary around 25°N.

Over 50% of particles that enter the ODZ travel along the core of the NSCC at 4-5°N, indicating that the NSCC likely plays an important role in ventilating the Eastern Tropical North Pacific ODZ. Most of the particles that originate in the NSCC enter the ODZ along the entire length of the southern boundary, with some entering as far west as 140°W. Some of these southern boundary particles (~15%) follow the NSCC eastward until they encounter the westward flowing South Equatorial Current near the eastern edge of the NSCC at around 90°W. Particle entries into the ODZ are frequent along the 1026.5 kg m^{-3} isopycnal (Figure 2.5c) and are carried into the ODZ by intrusions of water between the eastward flowing NSCC and westward flowing SEC. These features account for the prevalence of SOMs along the southern boundary of the ODZ.

The underlying mechanisms behind SOM production likely involve a complex interplay between the NSCC, eddies generated along the coast, eddies associated with Tropical Instability waves (TIWs), and exchange between the NSCC and the SEC. TIWs are an important mechanism for horizontal heat transport in the Equatorial Pacific (Jochum & Murtugudde, 2006) and likely also play an important role in the horizontal transport of O_2 in this region. Perturbations in [O_2] along the southern edge of the NSCC often closely match sea surface temperature and sea surface height anomalies in ROMS. However, no close correspondence was observed between these periodic perturbations at the southern edge of the NSCC from TIWs, and the O_2 fluctuations associated with SOMS at the northern NSCC edge. Moreover, the seasonal strength of TIWs (Contreras, 2002) was not reflected in particles entering the ODZ from the core of the NSCC nor in the regional O_2 budget (see section 3.3 below). This lack of seasonality suggests that TIWs do not exert complete control over SOM generation.

2.3.3 O_2 Budget of the Northern ODZ

Lagrangian particle tracking reveals how water enters the ODZ, but it does not directly translate into an O_2 flux. For that, we turned to an Eulerian framework to compute the regional O_2 budget, which can be written as:

$$\frac{dO_2}{dt} = J_{O_2} + \nabla \cdot uO_2 + D(O_2) \quad (2.2)$$

where J_{O_2} is O_2 production or consumption by the ecosystem model, $\nabla \cdot uO_2$ is the divergence of the O_2 flux into each grid cell by the resolved flow (u; a 3D velocity), and D(O_2) is the mixing of O_2 by unresolved physical flows, which are characterized by down-gradient diffusion. There is no prescribed horizontal diffusion in the model and vertical diffusion is computed using the KPP scheme (Large et al., 1997). The O_2 budget is computed in a constant control volume consisting of all grid cells in which 5-year mean [O_2] ≤ 5 mmol m^{-3}.

Modeled diffusive O_2 flux is typically an order of magnitude smaller than horizontal advective fluxes, except along the coast where high rates of vertical diffusion are driven by steep vertical [O_2] gradients (see below). Similarly, while J_{O_2} represents the net biological source minus sink, modeled O_2 production by photosynthesis within the ODZ is negligible compared to consumption via respiration. Thus, the O_2 budget of the ODZ is controlled by two primary fluxes: the biological respiration of sinking organic matter and the physical supply of O_2 via ocean circulation. The sum of the advective and (vertical) diffusive flux of O_2 into each grid point in the model (Figure 2.6b), is nearly balanced by J_{O_2} (Figure 2.6a and b), with residual differences arising from non-steady state trends in local [O_2].

Locations in the ODZ that have high net physical O_2 supply should coincide with regions of high J_{O_2}, which must be sustained by high particulate organic carbon fluxes. SOMs along the

southern boundary of the ODZ in the model are accompanied by high ecosystem respiration rates (Figure 2.6a) and relatively high O_2 flux (Figure 2.6b), indicating that there must be a lateral ventilation mechanism at this density. The high O_2 transport at the southeastern edge of the ODZ is balanced by high respiration rates associated with the degradation of organic matter flux from the Costa Rica Dome, which is a hotspot for both net primary production and surface nitrate in the model (Kessler, 2006; Wyrtki, 1964). There is also substantial particulate organic carbon (POC) export along the eastern margin, consistent with the classical view that eastern boundary upwelling systems are highly productive regions (Figure 2.6c).

The fluxes of O_2 to the ODZ are concentrated at its boundaries, with distinct mechanisms operating at the northern, southern, and eastern (continental) sides. The regions of high O_2 supply along the northwestern boundary are coincident with the NEUC jets at 13°N and 16°N, which carry relatively oxygenated water from the subtropical gyre eastward into the ODZ (Figure 2.6b). These eastward flowing zonal jets along the northwestern ODZ boundary supply approximately one quarter of the total without producing SOMs. The dominant supply of O_2 to the ODZ occurs in a small region bounded by 12°N and the southern ODZ boundary at 10°N. This southern flux is associated with high SOM frequency in the eastern edge of the basin and accounts for approximately half of the entire O_2 supply to the ODZ (Figure 2.3a and b). The remaining ~1/4 of the O_2 supply occurs at the eastern margin, through seasonal cycle of low-O_2 upwelling and high-O_2 downwelling (see below).

Partitioning the total O_2 transport into the mean advective O_2 flux ($\bar{u} \cdot \overline{O_2}$) and the time-varying "eddy flux" ($\overline{u'O_2'}$) further highlights differences in the O_2 supply mechanisms along the southern and northwestern boundaries. To diagnose the eddy component of the O_2 flux, we first computed the O_2 flux associated with the time-mean flow by computing the 5-year mean velocity

($\bar{u}$) and O_2 concentration ($\overline{O_2}$), and subtracting the product, $\bar{u} \cdot \overline{O_2}$, from the total transport of O_2 diagnosed by ROMS (Equation 2.3; Figure 2.8):

$$uO_2 = \overline{u'O_2'} + \bar{u} \cdot \overline{O_2} \quad (2.3)$$

The time-varying O_2 flux in Equation 3 includes seasonal and higher frequency variability. We evaluated regional differences between the supply mechanism of O_2 to the southern region of the ODZ (south of 11°N) and a northwestern region of the ODZ (north of 11°N, excluding ODZ cells within a few hundred km of the coast).

The mean advective supply of O_2 in the northwestern ODZ region accounts for up to three quarters of the total transport through that boundary (Figure 2.7a). The strength of the NEUC jets in ROMS oscillates seasonally, driving the large seasonal signal in O_2 flux in the northwestern region of the ODZ. The southern ODZ region, however, exhibits very little seasonality and the mean advective flux accounts for less than 5% of total O_2 supply (Figure 2.7b). These results further demonstrate that the main supply pathways of O_2 are the seasonal NEUC jets in the northwest via advection and non-seasonal instabilities of the NSCC that generate SOMs along the southern boundary.

In contrast to the southern and northern edges of the ODZ, the long stretch of the suboxic eastern margin is not adjacent to oxygenated water, except at the upper and lower interface, preventing strong lateral advective O_2 fluxes to this region. Lagrangian particle tracking did not reveal frequent intrusions of water from above or below that could oxygenate the ODZ. It can therefore be inferred that diffusive rather than advective processes are responsible for the O_2 flux that sustains the high rates of biological respiration in this region. This significant O_2 flux was not indicated by Lagrangian particle tracking because it is associated with a large diffusive O_2 flux and particle trajectories are unaffected by diffusion.

We diagnosed seasonal vertical [O_2] gradients, vertical diffusion rates, and associated biological consumption inside the climatological ODZ boundary along the eastern ocean margin on the continental shelf (Figure 2.8). As the water along the eastern boundary upwells seasonally, the vertical gradients in [O_2] become very strong, with [O_2] falling as much as 100 mmol m^{-3} over 50 meters (Figure 2.8a). The gradients are largely attributable to the shoaling of the suboxic water, which is accentuated by the photosynthetic O_2 production in the overlying photic zone. While the isopycnals near the top of the ODZ are not directly oxygenated by photosynthesis at this location, the steep [O_2] gradients drive a large downward diffusive flux (~0.2 x 10^{-5} mmol O_2 m^{-2} s^{-1}, Figure 2.8b) along much of the eastern boundary. When upwelling conditions relax and the isopycnals deepen back into the mean ODZ, they carry enough O_2 to account for aerobic respiration within the permanent ODZ. Budget analysis (Figure 2.8b) reveals that diffusion provides more than enough to balance respiration rates during seasonal downwelling (~-0.5 x 10^{-6} mmol O_2 m^{-2} s^{-1}). The additional O_2 supplied by vertical diffusion that is not consumed locally can then be advected even further westward into the ODZ interior, to fuel the high respiration rates apparent in the Eulerian O_2 budget.

2.3.4 Extra-tropical connections

The ventilation of the ODZ is achieved through the combined influence of water parcels that originated in different parts of the surface ocean at different times and that have traveled a wide variety of trajectories. We extended Lagrangian particle tracking to identify the pathways that water takes to reach the ODZ from the extra-tropical latitudes. This allowed us to identify the major circulation pathways that influence the ODZ on timescales ranging from decades to centuries.

To produce the long-term velocity fields used for this analysis, we used 10-year intervals of 5-day resolution velocity fields from ROMS, repeated 25 times. While this does not produce a true 250-year velocity record, it is useful as an approximation of the long-term mean flow in the model. We tracked particles backwards from the ODZ boundaries to their subtropical origins at 30°N and 30°S (Figure 2.9). We chose boundaries at 30°S and 30°N because the boundaries of the model domain limit our ability to track particles all the way to their outcropping regions south of 50°S. By computing the percentage of particles that cross these boundaries, we can identify where ODZ water originates in the subpolar regions. The time it takes for a particle to travel from 30^{o} latitude in either hemisphere to the ODZ allowed us to quantify the transit times of particles originating at different densities (Figure 2.9a and c) and to compute the fraction of particles that enter the ODZ on different time scales (Figure 2.9e).

After 250 years of reverse tracking, 32.9% of particles had crossed the northern boundary (30°N), while 60.2% of particles had crossed the southern boundary (30°S). Thus, the Southern Ocean would play a larger role in the ODZ's long-term climate response, even for the northern ODZ. Many of the particles pass through narrow currents along the western edge of the basin before they enter either the NSCC or the NEUC jets to enter the ODZ (Figure 2.9c). The dominant supply of particles from the Southern Ocean is via AAIW at around 1027 kg m^{-3}, with a mean transit time from the southern boundary to the northern ODZ of around 80 years (Figure 2.9c and e).

The particles arriving at the northern ODZ from the southern hemisphere departed at a wide range of times, from a decade to over two centuries. This implies that the climate signal from a southern source would impact the ODZ for well over a hundred years. While there is a more substantial supply of particles from the Southern Hemisphere, there is a shorter transit from the

northern boundary to the ODZ, as seen in the clustering around a transit time of 30 years (Figure 2.9a and 2.8c). The particles that originate in the Northern Hemisphere have a mean transit time of about 60 years and exhibit a more pronounced short-term impact, which is associated with the broad northern source that spans 180°E to 80°W with densities ranging from 1026-1026.5 kg m^{-3} (Figure 2.9a). By 110 years, over 90% of particles that start at 30°N reach the ODZ, with a relatively short tail at 1027 kg m^{-3} from the western boundary currents at 140°E (Figure 2.9a). Areas where particle crossings are densely concentrated (e.g. around 175°W) correspond well with the location of equatorward flows in ROMS. Deep poleward currents that bring particles into the tropics at these latitudes are supported by observations of alternating equatorward and poleward currents (Whitworth III et al., 1999). The long tail for particles traveling from 30°N to the ODZ can be partially explained by the fact that 30% of particles originate in the Northern Hemisphere, while only 20% enter from the northwestern ODZ boundary. This result implies that a third of the particles originating in the Northern Hemisphere that enter the ODZ must arrive via a more circuitous route through the near-equatorial jets. The water that follows this long route must get incorporated into the NSCC, since that is the dominant supply mechanism for water and O_2 along the southern ODZ boundary.

2.4 Discussion

We have demonstrated that narrow zonal jets, their instabilities, and seasonal downwelling of oxygenated water along the eastern boundary are important controls on the physical supply of O_2 to the Eastern Tropical North Pacific ODZ. These pathways and mechanisms that supply O_2 to the ODZ in ROMS would not be well resolved in coarse resolution models and may explain the difficulty those models have in reproducing the mean ODZ structure. To quantify the O_2 supply associated with each source (the NSCC, the NEUC jets, and seasonal upwelling cycles), we

divided the ODZ into three regions: 1) an "NSCC" region corresponding to all O_2 fluxes south of 11°N, 2) an eastern boundary region that corresponds to the shoreline where O_2 supply rates exceed 25 mmol s^{-1} m^{-1} and 3) the area remaining after the eastern boundary region and NSCC region are removed. The horizontal supply of O_2 to the ODZ is ~50% attributable to SOMs produced by the NSCC which penetrate the core of the ODZ with an additional ~25% due to zonal advection of O_2 from the NEUC jets at 12°N and 16°N, while the remaining ~25% O_2 supply is due to the vertical flux from seasonal upwelling-downwelling cycles along the eastern boundary (Figure 2.10).

The prevalence of SOMs as a ventilation mechanism suggests that they likely are an important control on the microbial processes in the ODZ. The SOMs ventilating the ODZ may support additional organic matter degradation through aerobic respiration and thus suppress denitrification. The westward flowing NEUC jets likely also play a significant biogeochemical role in the transport of strongly N-depleted waters out of the ODZ.

Earth System Models robustly predict more pronounced declines in oceanic [O_2] in the mid-latitude North Pacific compared to the South Pacific in response to rising global temperatures (Bopp et al., 2013), but it is uncertain how these long-range influences impact the North Pacific ODZ, and over what time scales. Our particle tracking results suggest that extra-tropical O_2 anomalies originating in both hemispheres would produce a long-term ODZ response (i.e. after ~30 years) dominated by the Southern Hemisphere, which contributes many particles with long transit times, while the short-term ODZ response (i.e. before ~30 years, Figure 2.9e) would be dominated by anomalies originating in the Northern Hemisphere. This partitioning implies that moderate Southern Hemisphere deoxygenation likely plays an important long-term role in ODZ maintenance, while extreme Northern Hemisphere deoxygenation likely impacts the ODZ on timescales as short as 30 years. The Northern Hemisphere influence which accounts for up to two-

thirds of particles that travel to the ODZ from 30°N in the first 50 years would fall off quickly and would be replaced by signals arriving from the Southern Hemisphere, which would continue to influence the ODZ for more than a century. The complex combination of time-lagged influences on decadal to centennial timescales will compound trends of similar time-scales that have been attributed to tropical winds (Deutsch et al., 2014).

Observations of how these pathways in the real ocean vary over time and a characterization of their mean O_2 supply would provide an empirical basis for evaluating ROMS and other models' ODZ ventilation schemes. In particular, the magnitude of the seasonal upwelling and downwelling that infuses O_2 along the eastern edge of the ODZ in the model signifies a potentially important source of O_2 to the ODZ, but a complete analysis of this source requires more empirical constraints. Similarly, rates of O_2 consumption (and therefore O_2 supply to the ODZ) inside of a SOM could be obtained by tracking a SOM in real time with an Argo float, providing an observational constraint for evaluating the transition from aerobic to anaerobic metabolism and its representation in microbial ecosystem models (Penn et al. 2019). Time series observations in locations along the shelf where there are steep vertical O_2 gradients would enable us to evaluate and constrain the eastern boundary O_2 supply in the model.

Our results indicate a significant time-varying eddy flux along the southern, northwestern, and eastern boundaries of the ODZ. These fluxes are likely also subject to both natural (i.e. ENSO, PDO, etc.) and anthropogenic variability on interannual and interdecadal timescales (Ito & Deutsch, 2013; Duteil et al., 2018). The ODZ's time-varying response is further complicated by the fact that the broad spectrum of ventilation timescales act to smear climate signals over many decades before even arriving to the tropical ODZ. A full description of climate change's influence

on the ODZ will require models that resolve the narrow zonal jets that supply O_2 as well as long-term trends in extra-tropical forcing.

2.5 Figures

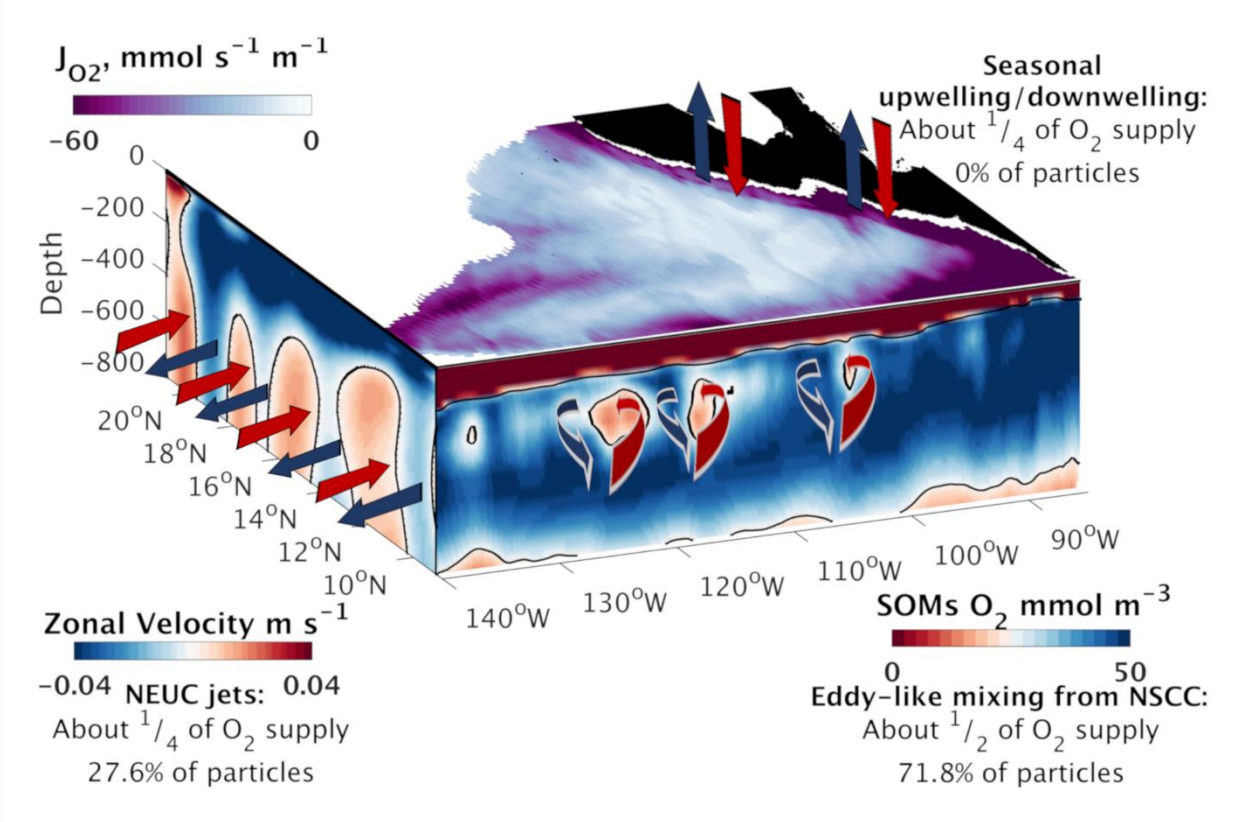

Figure 2.1. Model comparison to 2013 World Ocean Database (WOD13) O_2 data (Boyer et al., 2013). All O_2 concentrations are interpolated to 350 m. The colored points include all 1°x1° grid cells in which binned measurements from the WOD13 contain $O_2 \leq 30$ mmol m^{-3} and all colored lines correspond to the 30 mmol O_2 m^{-3} contours in four CMIP5 models (MPI-ESM-LR, HADGEM2-ESM-LR, IPSL-CM5A-LR, and GFDL-ESM2M; Taylor et al. 2012) and the Regional Ocean Modeling System (ROMS, black line) used in this study (see Section 2.2).

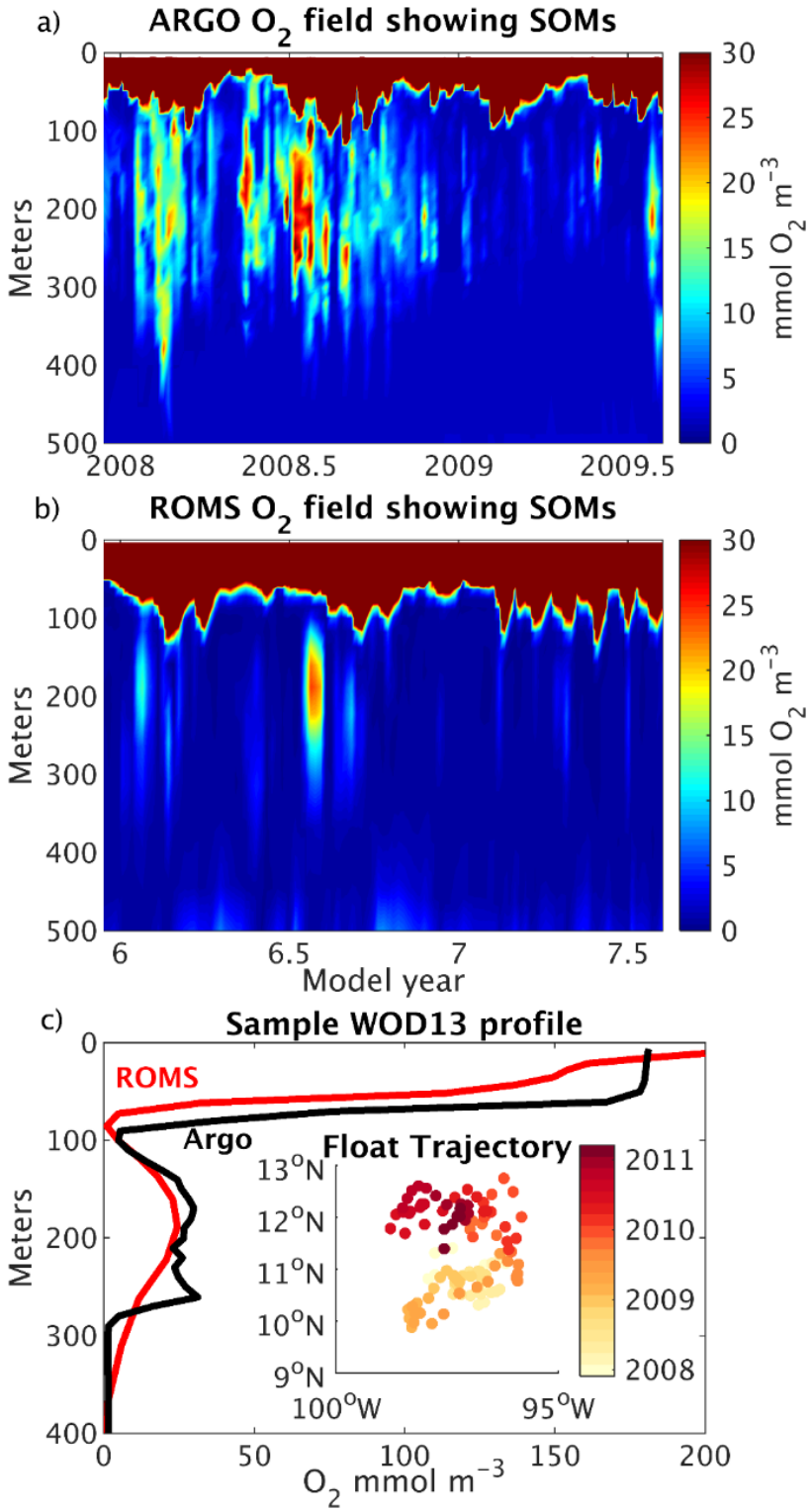

Figure 2.2. Sample [O_2] time series along an Argo float track (float #5901463) and in ROMS. Secondary Oxygen Maxima (SOMs) appear in the Oxygen Deficient Zone (ODZ) at around 200-

300m in the Eastern Tropical Pacific in Argo data (a, raw [O_2] data). Sampling ROMS in a similar location reveals similar features in the model (b). (c) a sample profile through a SOM in both WOD13 and ROMS (~11°N, 98°W). (c, inset) the Argo float trajectory with color corresponding to the times that the float reported data, which shows higher SOM frequency during the first few years when the float is closer to the southern limit of the ODZ. ROMS O_2 fields are shown with 5-day averaging. We found no difference in SOM magnitude or frequency between calibrated and uncalibrated data, so we use uncalibrated Argo data with no time averaging to maximize the number of available profiles. The latitudes sampled in ROMS are at a 1° offset to the south to compensate for more rapid drop-off from south to north in SOM magnitude.

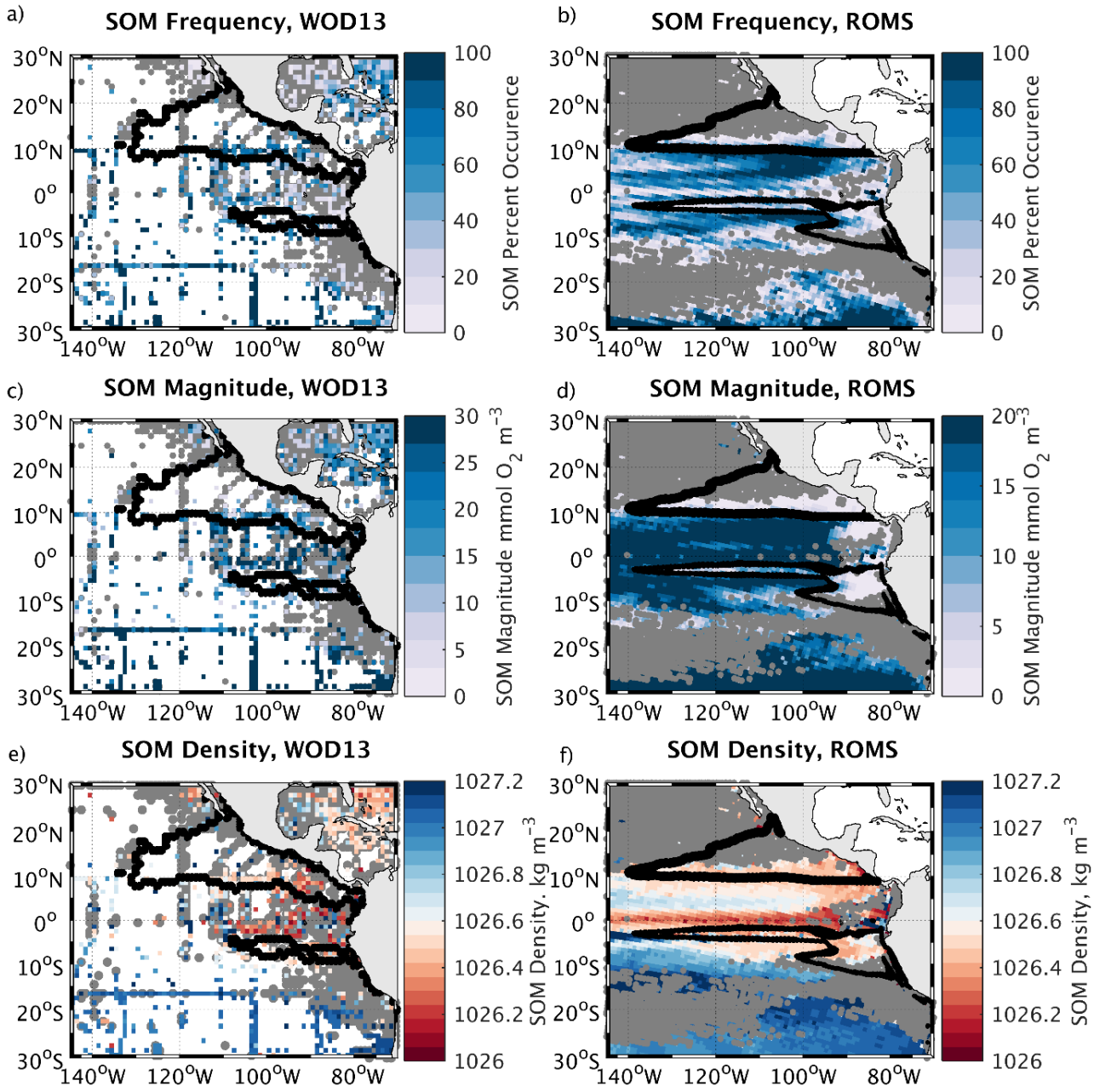

Figure 2.3. SOM distribution and characteristics in the Eastern Tropical Pacific. SOMs are widespread and frequent features in the Eastern Tropical Pacific in WOD13 (a,c,e) and in ROMS (b,d,f), especially along the equatorward borders of the ODZs (the black outlines). Analysis of the data was done by identifying peaks in each vertical profile within the 1026 – 1027.5 kg m^{-3} density range where there are at least 3 profiles in the same grid cell. The white space in the data indicates

regions with fewer than 3 separate profiles, while the grey dots indicate grid cells that have 3 or more profiles but no SOMs. The percent of profiles that have a SOM in the 1026 – 1027.5 kg m^{-3} density range is shown in WOD13 (a) and ROMS (b). SOM magnitude is shown in WOD13 (c) and ROMS (d), calculated as the difference between the maximum oxygen anomaly minus the background concentration (a linear average between the minima on either side). The mean density at which these anomalies occur is shown in (e) and (f). The black ODZ outlines are the perimeters of the 5 mmol O_2 m^{-3} region in ROMS (b,d,f) at 350m and in World Ocean Atlas 2013 (a,c,e; Garcia et al., 2014) where $[O_2] \leq 5$ mmol m^{-3} at 350 meters in at least two months in the climatology. The symmetry of SOM occurrence on either side of the equator suggests similar mechanisms are at work in both hemispheres.

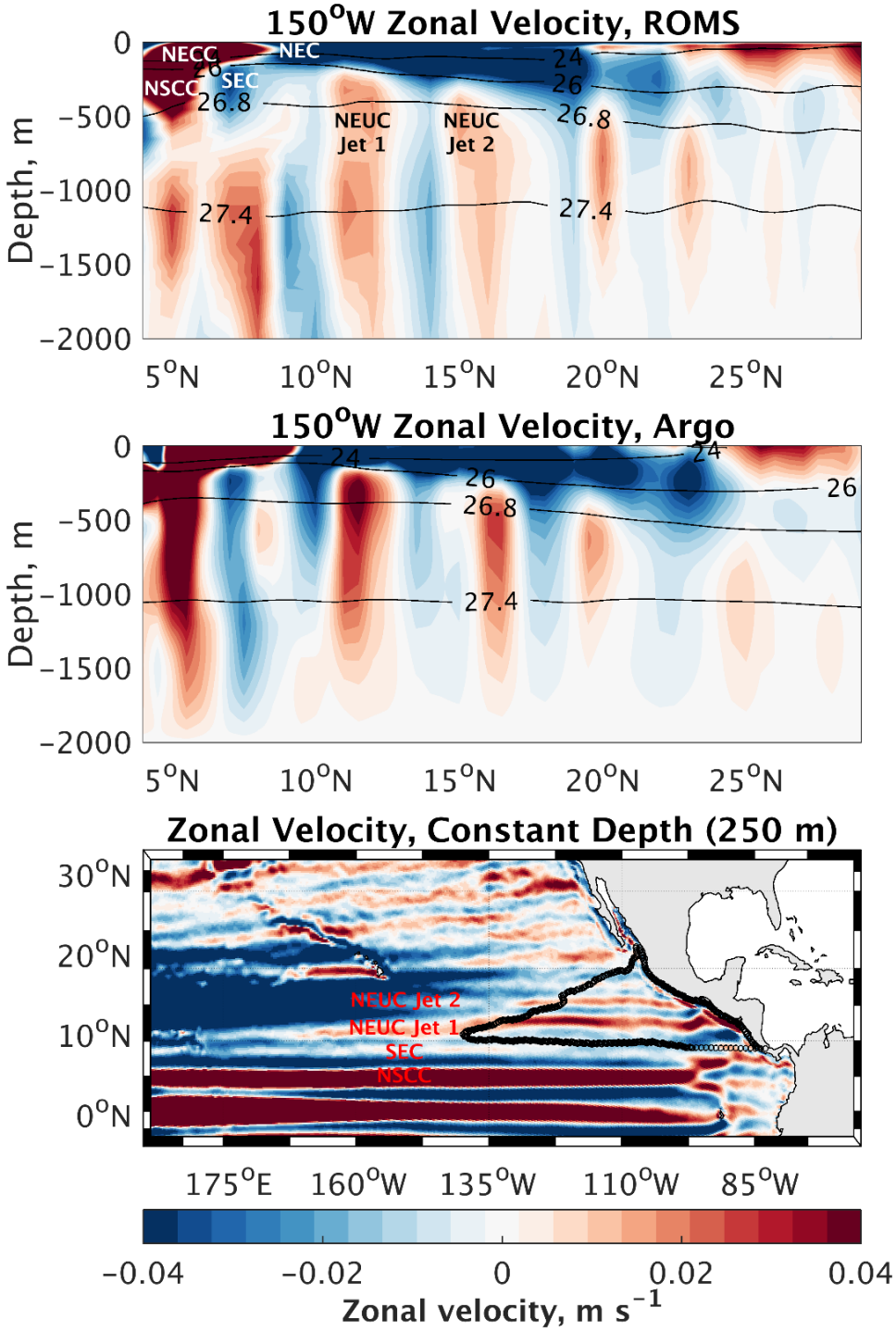

Figure 2.4. Zonal velocity transects at 150°W in (a) ROMS output and (b) Argo float data (Qiu et al. 2013). ROMS zonal velocity interpolated to 250m is shown in (c). Eastward zonal velocities are positive (red) in all maps and all model velocities are averaged over two years. The eastward

flow at around 5°N is comprised of two connected currents: the near-surface North Equatorial Countercurrent (NECC) and the deeper Northern Subsurface Countercurrent (NSCC). Zonal jets at 13°N and 16°N (the North Equatorial Undercurrent jets or NEUC jets) also carry oxygen eastward into the ODZ.

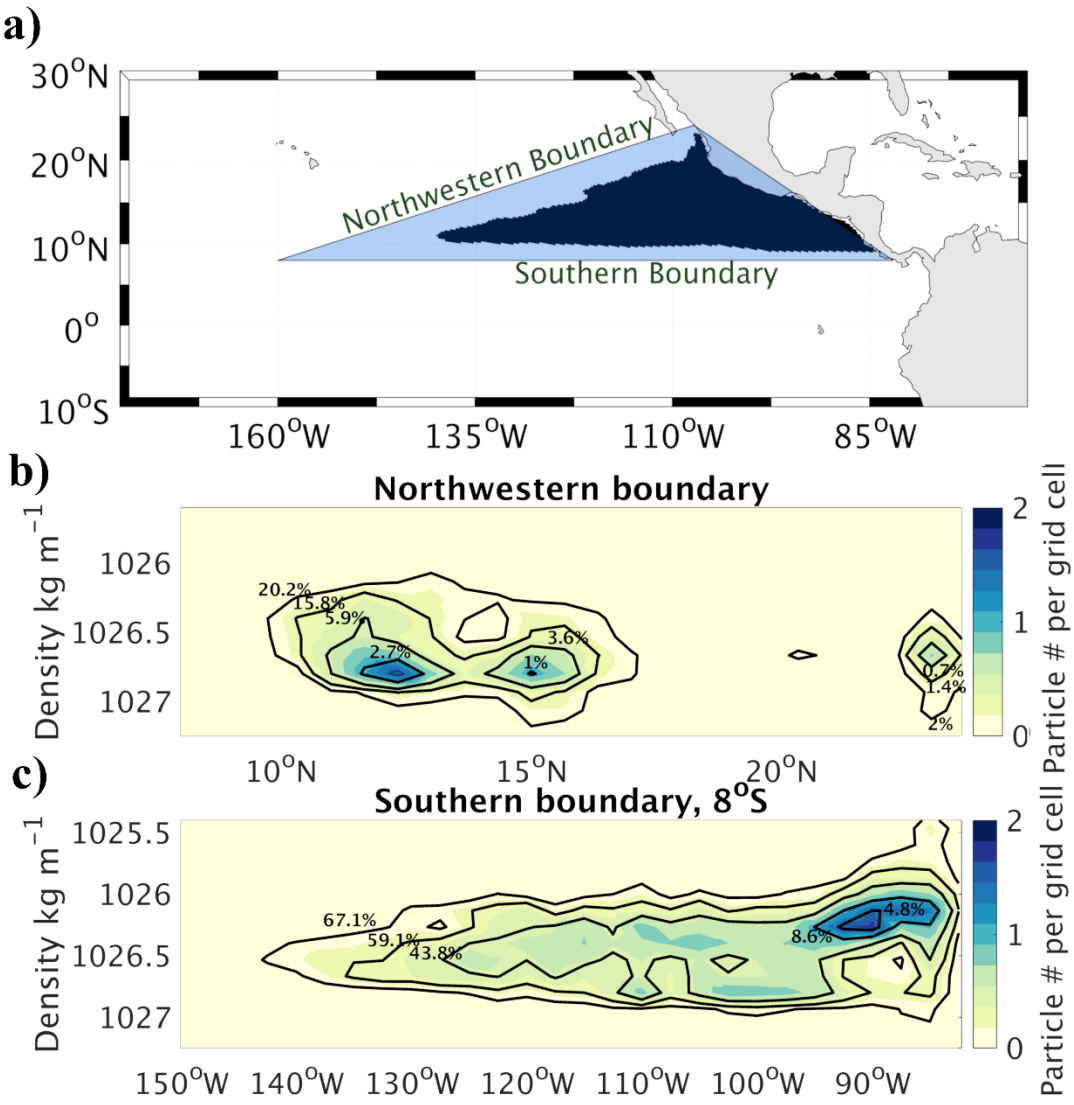

Figure 2.5**.** Water parcel entry to the ODZ, based on reverse Lagrangian particle tracking. Because the ODZ has a complex shape, we define simple boundaries (blue shading in panel a) to determine which waters enter from the top (50m), bottom (2000m), south (8°N), and northwest (8°N to 25°N,). By integrating the number of particle crossings within each closed contour in (b) and (c), we calculate the percent of the total number of particles (17214) that enter the ODZ from each boundary. 10.2% of particle crossings (5.4% in b and 4.8% in c) fall outside of the chosen contours and 1.6% of particles enter the ODZ from above (1.2%) or below (0.4%). 70.8% of particles enter

the ODZ along the entire southern boundary, while the northwestern boundary supplies 27.6% of particles via the NEUC jets at ~13°N and 16°N.

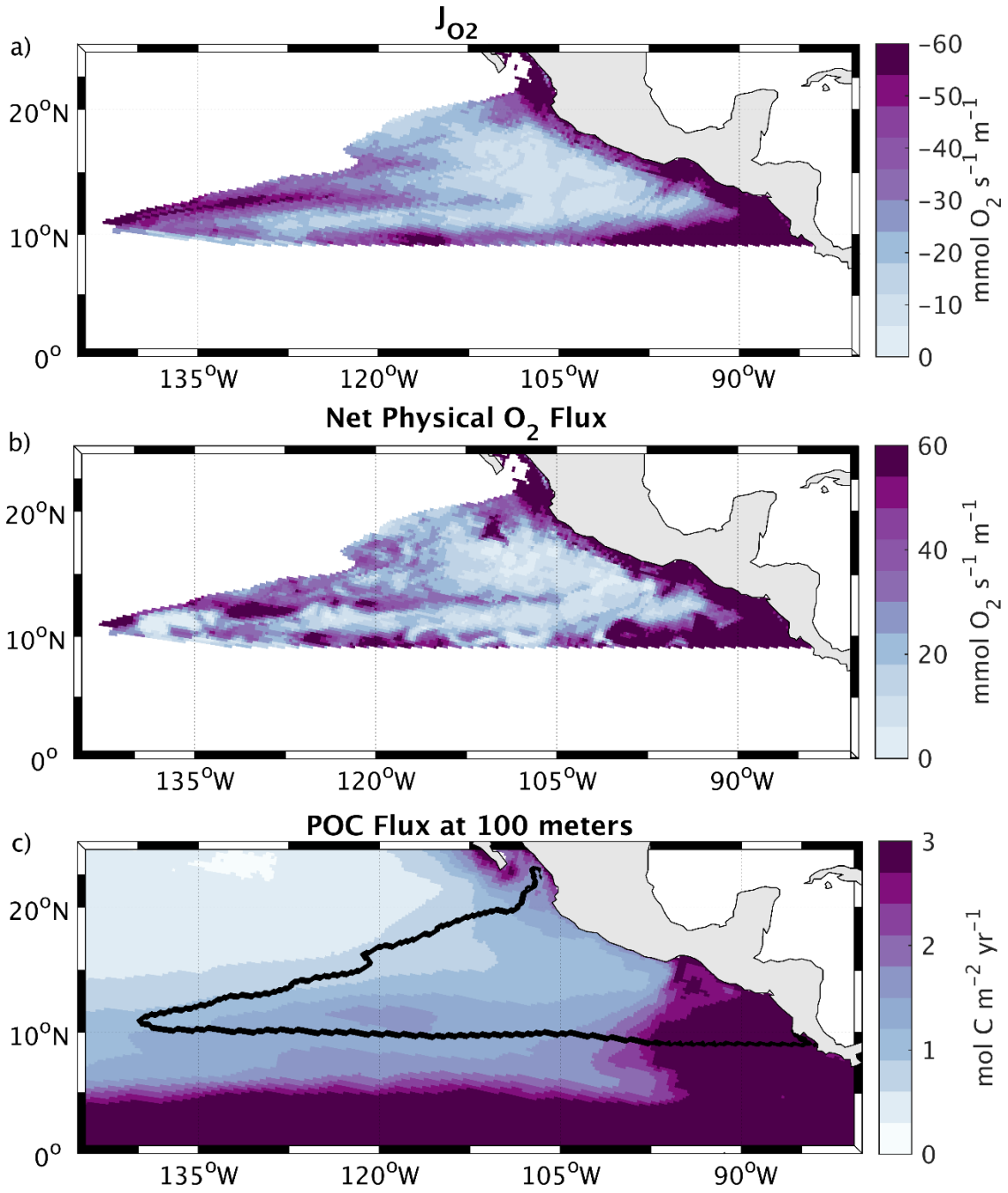

Figure 2.6. The Eulerian O_2 budget in the ROMS ODZ, defined as the region with 5-year mean $[O_2] \leq 5$ mmol m^{-3}. Rates of (a) the integrated ecosystem derived J_{O2} ($O_{2,production}$ - $O_{2,consumption}$), and (b) the divergence of the O_2 flux into each model grid cell, are integrated over the depth of the ODZ and divided by its thickness. (c) the particulate organic carbon (POC) flux that supports the

high respiration rates inside the ODZ. Relatively high O_2 fluxes are present in the eastward flowing zonal jets at 13°N and 16°N, as well along the equatorward boundary at 10°N and the eastern boundary along the coast.

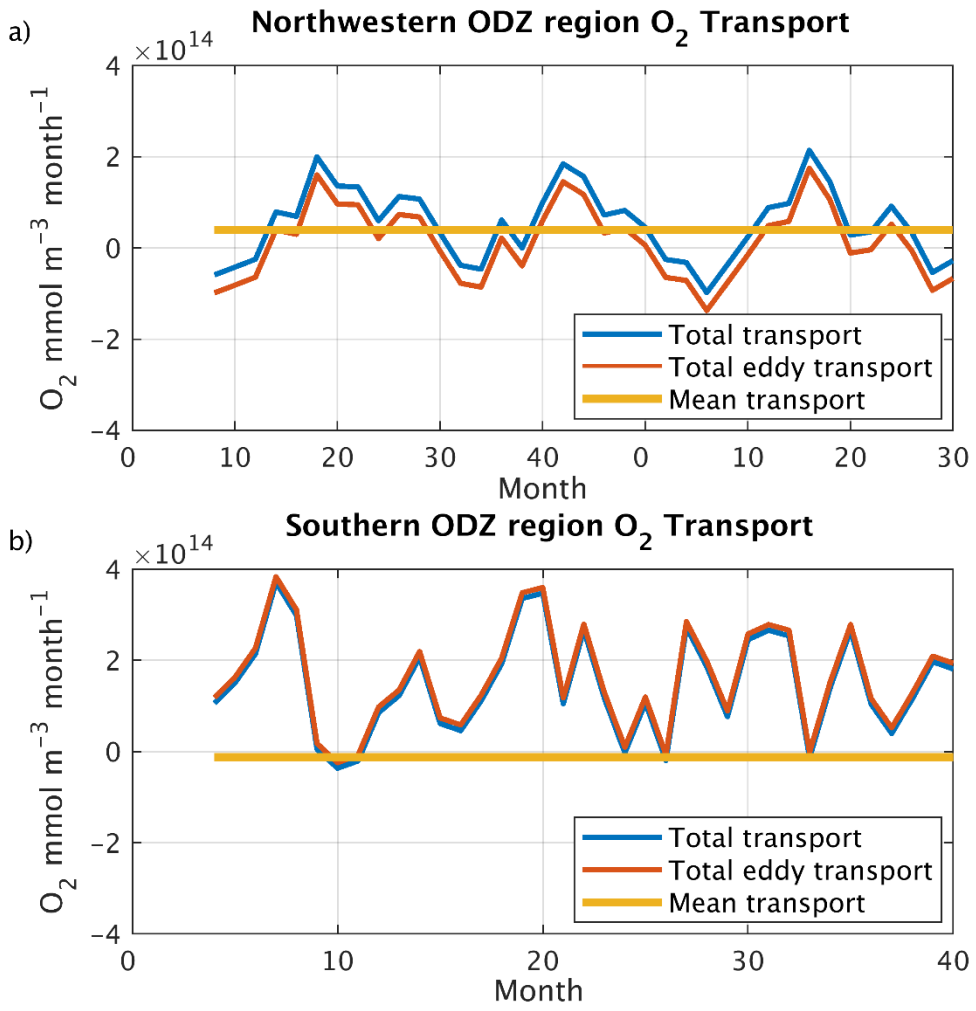

Figure 2.7**.** The decomposition of O_2 transport into the mean advective O_2 flux ($\nabla \cdot \overline{uO_2}$) and the time-varying eddy flux ($\nabla \cdot \overline{u'O_2'}$). The blue line in each panel corresponds to the total supply (flux convergence) of O_2, the yellow line is the mean advective flux into each region calculated using 5 year mean velocities and $[O_2]$, and the orange line is the difference between the total transport and the O_2 transport by the mean flow. (a) the transport time series for a subsection of the ETNP ODZ north of 11°N and a few hundred kilometers west of the coast, (b) the transport time series for the subsection of the ETNP ODZ south of 11°N. The northwestern region exhibits strong seasonality and receives its O_2 predominantly from the mean flow (about three quarters), whereas the southern

ODZ region receives its O_2 almost entirely from the time-varying flux of O_2 (over 95%) and with very small O_2 fluxes driven by the mean flow.

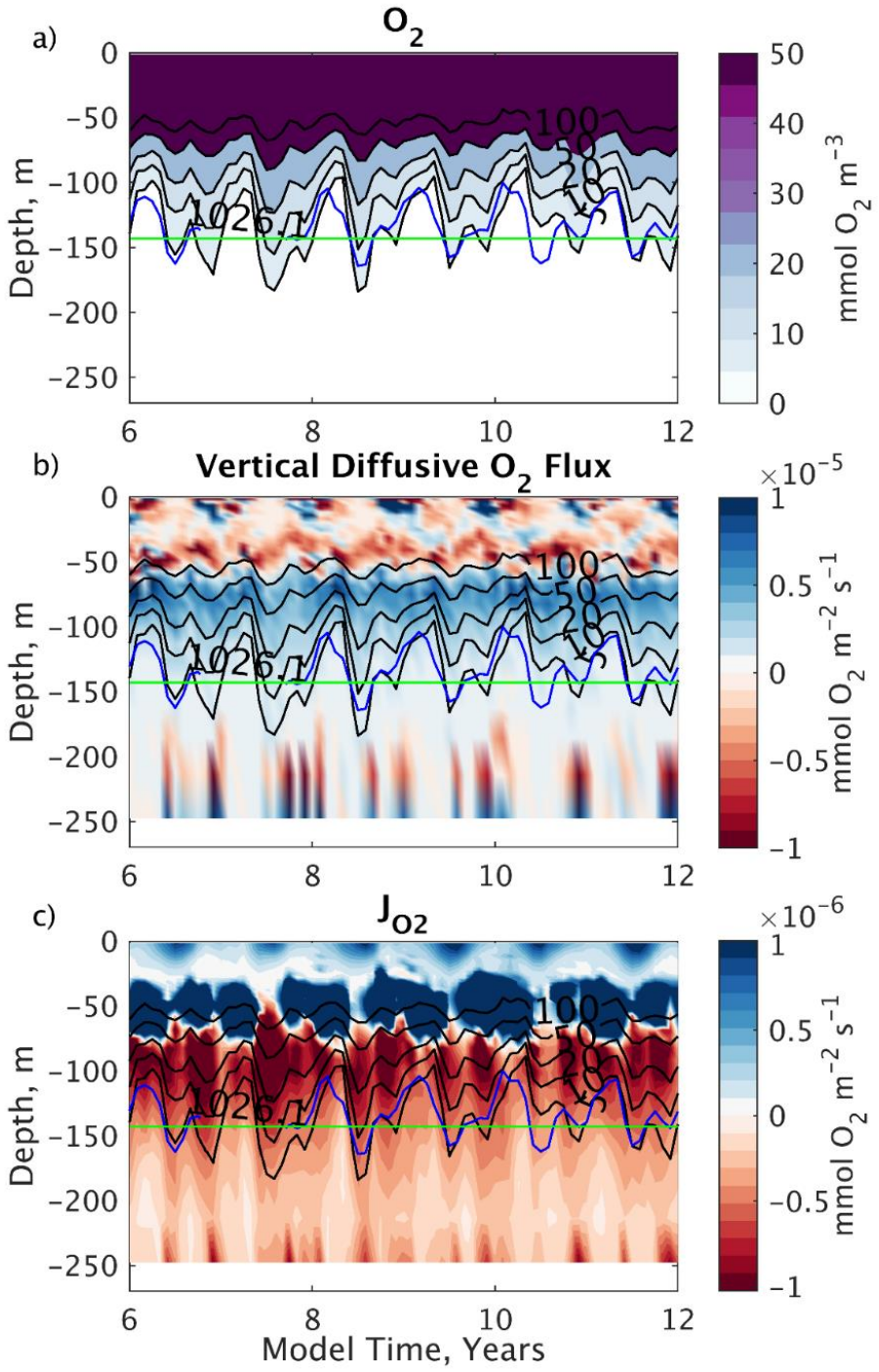

Figure 2.8**.** Hovmöller diagram of the seasonal evolution of (a) vertical O_2 distribution, (b) diffusive fluxes, and (c) biological source-sink at a representative location along the eastern boundary of the ODZ (93°W and 15°N). The black contours in (a), (b), and (c) correspond to [O_2]

of 5, 10, 20, 50, and 100 mmol m^{-3}, while the blue contour is the depth of the 1026.1 kg m^{-3} isopycnal, and the green line is the top of the climatological ODZ boundary at this location. Seasonal upwelling lifts isopycnal surfaces and O_2 deficient water near the photic zone (a), where high vertical diffusive fluxes replenish the O_2 (50-100m; panel b). Seasonal downwelling brings the high [O_2] water back into the ODZ, where it supports seasonally high respiration rates (c). This rectified seasonal upwelling flux is the dominant mechanism of O_2 supply along the eastern boundary, which accounts for approximately ¼ of total O_2 supply to the ODZ.

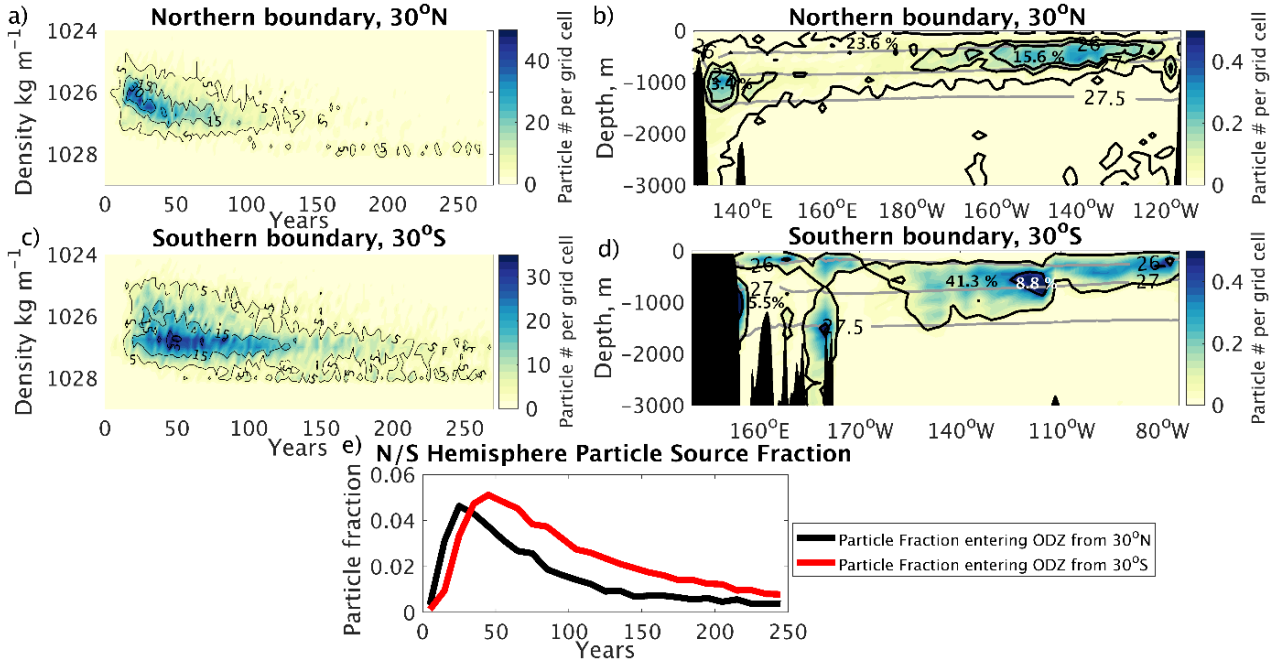

Figure 2.9. Long-range sources of ODZ water back-tracked to boundaries at 30°N and 30°S. As each particle crosses each boundary, we store its density and transit time (a and c), as well as its depth and longitude (b and d). Particle crossings are binned for plotting, as in Figure 2.5. We integrate the absolute particle number within select contours and calculate the fraction of the total particle number (17214) in (b) and (d). About ~30% of the total particle flow across the boundaries in (b) and (d) is very diffuse and is therefore not easily captured by closed contour mapping. The fraction of particles that cross each boundary in 10-year bins (panel e) shows characteristic transit times from both hemispheres. Fitting an inverse Gaussian to the transit time distributions in (e) yields fit parameters $\mu_{north} = 82.6$; $\lambda_{north} = 97.1$ and $\mu_{south} = 102.9$; $\lambda_{south} = 180.9$ (e.g. Seshadri, 1999) The ratio of $\frac{\mu_{north}}{\lambda_{north}} / \frac{\mu_{south}}{\lambda_{south}}$ is greater than one, which implies a lower Peclet number and therefore stronger mixing relative to advection, flow from 30°S to the ODZ.

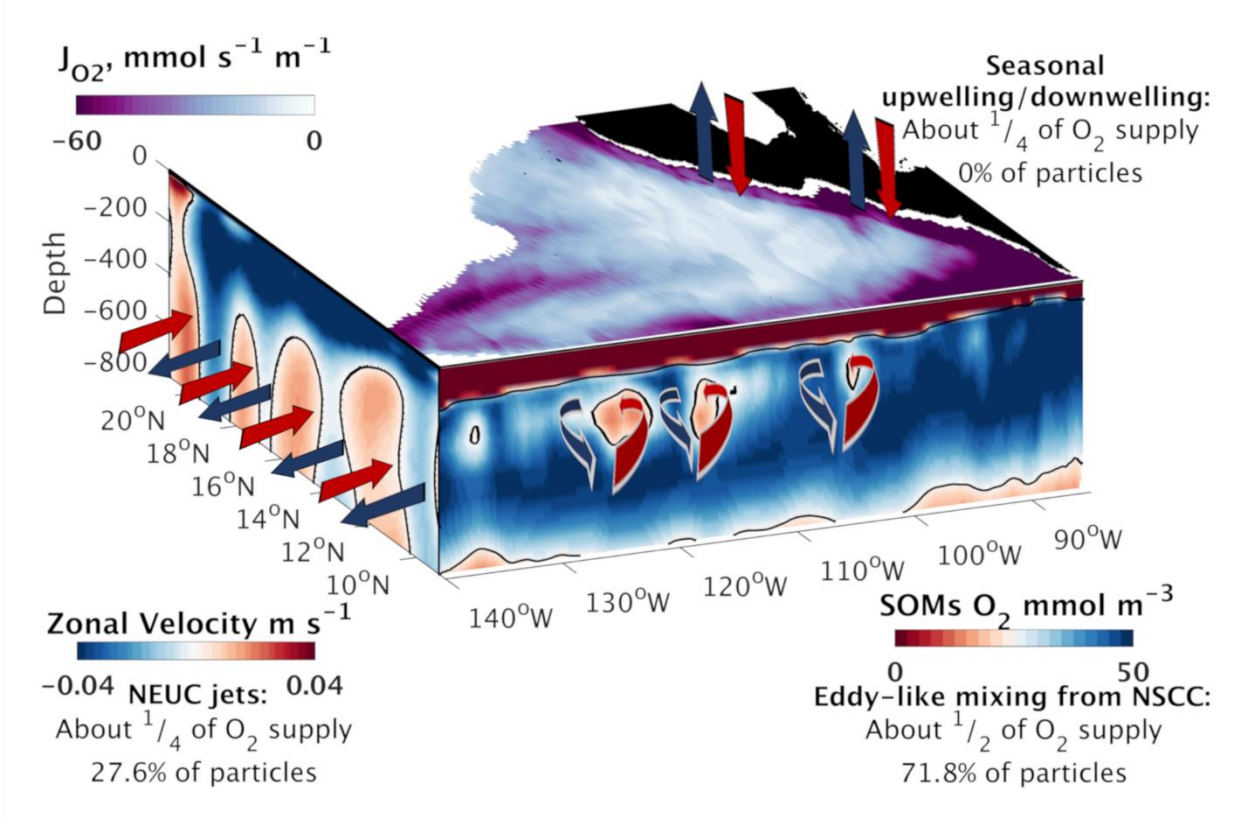

Figure 2.10**.** The three-dimensional structure of ODZ ventilation. Red arrows in the figure depict the flow of oxygenated water into the ODZ, while blue arrows depict the flow of O_2 depleted water out of the ODZ. (Top panel) J_{O2}, (left panel) zonal velocities at 150°W, and (front panel) [O_2] at 10°N in ROMS. Roughly a quarter of total O_2 supply (27.6% of particles) is characterized by eastward flowing zonal jets at 12°N and 16°N along the northwestern boundary. About half of the total O_2 supply (70.8% of particles) is supplied by the time-varying eddy flux ($\overline{u'O_2'}$, Figure 2.7b) along the southern boundary. Seasonal downwelling of high [O_2] from above accounts for about a quarter of O_2 supply (0% of particles). The mismatch in volume transport and O_2 supply highlight mechanisms of O_2 delivery not associated with the mean flow of water, particularly for the eastern boundary, where O_2 supply is achieved via vertical diffusion and isopycnal heaving.

Chapter 3

CLIMATIC CHANGES IN NORTH ATLANTIC O_2 AMPLIFIED BY TEMPERATURE SENSITIVITY OF PHYTOPLANKTON GROWTH

Abstract

Ocean warming is associated with a decline in global O_2 inventory, but the ratio of O_2 loss to heat content gain is poorly understood. We analyzed historical variability in temperature, O_2, and nitrate in hydrographic observations and model simulations of the North Atlantic, a well-sampled region that is important for deep ocean ventilation. Multidecadal fluctuations of deep water O_2 are correlated with changes in the heat content of those waters, with a slope 40% higher than that expected from temperature-dependent solubility. The additional component of O_2 variation is correlated with observed decadal changes in the nitrate in surface waters throughout the subpolar North Atlantic. Surface nitrate varies by 1 mmol m^{-3} per degree of surface temperature implying a biological transfer of nutrients from the surface ocean to deep water and accompanying respiratory depletion of deep water O_2 during warm years. In model simulations, increased nutrient depletion during warm periods is driven by an early start of the phytoplankton growing season and faster phytoplankton growth rates at higher temperatures. Our results highlight the key role that phytoplankton temperature-dependent growth rates play in driving approximately one third of observed O_2 variability in the North Atlantic.

3.1 Introduction:

Observations indicate declining global ocean oxygen since the 1980's in parallel with rising global ocean heat content (Ito et al., 2017; Oschlies et al., 2017; Schmidtko et al., 2017) and ocean models predict this deoxygenation trend will continue into the future (Bopp et al., 2017). The global magnitude and regional distribution of deoxygenation in the future is uncertain (Bopp et al., 2013; Deutsch et al., 2011; Gnanadesikan et al., 2012; Keeling et al., 2009). Moreover, there are indications that Earth system models simulate oxygen declines over recent decades that are weaker than observed (Long et al., 2019). Current model simulations of ocean oxygen exhibit a broad range of global oxygen decrease in response to increased global ocean heat content in the past, which results in even more broad range of predictions for future ocean oxygen content (Keeling et al., 2009). The inter-model spread in the relationship between ocean oxygen and heat content contributes to uncertainty in the magnitude of the future oceanic O_2 response to warming in this region (Bopp et al., 2013; Laffoley & Baxter, 2019). Understanding the relationship between ocean heat uptake and deoxygenation is of central importance to the carbon cycle and marine ecosystem health. The O_2 depletion in deep water is directly tied to the ocean's reservoir of biologically sequestered carbon (Matear & Hirst, 2003) and the combination of warming and O_2 loss imposes interacting metabolic constraints on marine ecosystems. (Deutsch et al., 2015) Oxygen loss can stress biota in or near habitats with already persistently low oxygen concentrations, like oxygen minimum zones (Diaz & Rosenberg, 2008; Stramma et al., 2008) and eastern boundary current systems (Howard et al., 2020).

Ocean O_2 loss is linked to rising temperature through a combination of three known mechanisms: declining gas solubility at the surface, reduced thermocline ventilation, and changes in the biological production and consumption of O_2 in surface and deep water, respectively. While

these three mechanisms are known, their relative contribution to observed O_2 variability is unknown and is complicated by the dynamic linkages between overturning, ventilation, nutrient supply to the surface, and remineralization of sinking organic matter. (Bopp et al., 2013; Eddebbar et al., 2017; Takano et al., 2018; Ito et al., 2019). The flux of oxygen into the main thermocline depends on the rate of exchange of surface water with the interior and the thermodynamically-saturated O_2 concentration at the ocean surface, which are both expected to decrease with warming as the ocean becomes more stratified (Li et al., 2020; Liu et al., 2020). Warming-induced stratification also reduces the rate of nutrient supply to the surface ocean, potentially decreasing biological O_2 production and subsequent organic carbon export. Higher metabolic rates at warmer temperatures enhance the microbial degradation rate of organic matter, especially near the surface where microbial populations are larger, which has the potential to influence the efficiency of carbon export by vertically redistributing respired O_2 consumption. Attributing the cause of low frequency multidecadal oscillations to specific mechanisms is a critical step toward understanding how global ocean oxygen content will change in the future.

The North Atlantic is uniquely suited to constraining the interacting mechanisms through which climate impacts ocean oxygenation. First, it plays a critical role in deep water formation and therefore is responsible for ventilating a large volume of water with O_2 and storing anthropogenic CO_2 (Gruber et al., 2019; Sabine et al., 2004). Second, the North Atlantic is a high-nutrient, low-chlorophyll region, where surface waters bear unused nutrients that could fuel additional productivity and deep respiration even with no change in ventilation. Third, the dominant mode of regional climate variability - the North Atlantic Oscillation (NAO, Hurrell et al., 2003) - provides natural ‘experiments’ that can be used in conjunction with an ocean model to evaluate the biogeochemical response to changing surface temperature, circulation, and deep winter mixing on

interdecadal timescales. Fourth, the extensive suite of historical observations available in the North Atlantic provide empirical constraints on the mechanistic controls over oxygen variability.

Long term trends in the North Atlantic O_2 have been described previously, with a focus on the period from 1960 to 2009, revealing long term trends of opposite signs and complex spatial pattern (Stendardo & Gruber, 2012). Here, we use interdecadal fluctuations of O_2 and their relationships to both temperature and nutrients to diagnose the causes of historical O_2 changes in the observational record. Using a hindcast configuration of the Community Earth System Model (CESM), we are able to reproduce and evaluate the observed interdecadal variability of thermocline O_2 in the subpolar North Atlantic: the only region of deep-water formation with adequate historical observations of oxygen, nitrate, and temperature over the past 50 years. We evaluated the relative contributions of temperature induced changes in gas solubility, biological uptake of nutrients, and circulation and find that the efficiency of the biological pump in the subpolar North Atlantic is tied to temperature-sensitive growth rates and accounts for almost half of the observed interdecadal response to temperature.

3.2 Conceptual Model

To understand the causes of changing O_2, we analyze both observations and numerical simulations using a simple Lagrangian model in which changes in deep water can be traced back to surface properties most directly influenced by regional climate. Within the surface mixed layer, O_2 is controlled by temperature-dependent gas exchange with the atmosphere, biological productivity, and exchange with the underlying deep water. As water exits the mixed layer, it carries a record of surface temperature and an associated 'preformed' O_2 (O_{2pre}), which is conserved during transport in the ocean interior. Below the surface, neither photosynthesis nor gas exchange can replenish oxygen, so the water parcel's in situ oxygen concentration declines with

time through the cumulative effect of organic matter degradation via microbial respiration, which we denote O_{2res}. Oxygen in deep water can be considered the sum of these preformed and respired components, and its fluctuations over time (denoted by D) can be written as:

$$\Delta O_2 = \Delta O_{2pre} + \Delta O_{2res} \quad \text{Eqn 1}$$

This separation has been widely used to estimate the direct contribution of temperature changes to O_2, by assuming that the O_2 at the time of water mass formation is equilibrated with the atmosphere (i.e. $O_{2pre} \approx O_{2sat}$). Under this assumption, the oxygen consumption due to the biological pump can be estimated as the difference between in situ O_2 and O_{2sat}, which is commonly referred to as the Apparent Oxygen Utilization (AOU = $O_2 - O_{2sat}$). In reality, however, O_2 disequilibrium in the surface ocean is not trivial, especially in regions of strong surface cooling and deep convection where the residence time of surface water is shorter than the timescale of gas equilibration (Ito et al., 2004).

Changes in ΔO_{2res} driven by respiration and remineralization will also be reflected in macronutrients, due to the close coupling between the cycling of O_2 and nutrients. As organic matter is remineralized, oxygen is consumed and inorganic nitrogen is released into the water column as regenerated nitrate (N_{reg}) in an average ratio of -150 O_2:16 N ratio (the Redfield ratio, Anderson & Sarmiento, 1994; Körtzinger et al., 2001). Deep ocean nutrients are subject to the same conceptual separation as for O_2 (Eqn 1) such that $\Delta N = \Delta N_{pre} + \Delta N_{res}$. Addition of nitrate via nitrogen fixation has the potential to complicate the attribution of surface nitrate changes, but it can be accounted for by evaluating interannual changes in the N inventory over time (ΔN). ΔN is close to zero in this region in CESM, which confirms that nitrogen fixation is not a significant driver of interannual nitrogen variability in the model. Any mole of nitrate still present in a water parcel at the surface when it is subducted directly corresponds to a mole of nitrate that was not

incorporated into organic matter and therefore cannot have incurred any O_2 loss. This surface nitrate signature is preserved in subducted water parcels as preformed nitrate (N_{pre}) and is determined by the balance of upwelled nitrate from below during wintertime convection and algal removal of nitrate over the course of the growing season. Local changes in phytoplankton uptake can therefore result in synchronous changes of opposing signs in N_{pre} and N_{reg} that can be converted into ΔO_{2res} via the Redfield ratio.

$$\Delta O_2 = \Delta O_{2pre} + r(\Delta N - \Delta N_{pre}) \qquad \text{Eqn 2}$$

While the preformed concentrations in deep water (Eqn 2) are represented as single quantities, they can more generally be the result of a complex mixture of waters that originate from different surface regions with distinct concentrations. An interior water parcel's preformed concentration of any arbitrary tracer, C_{pre}, therefore can be defined as a linear combination of n endmember source water locations, each with time varying surface concentrations, $C_{surf,,i}(t)$, and contributing a time-dependent fraction, $f_i(t)$, of the total volume in a deep water mass, such that $C_{pre} = \sum_i(f_i(t)C_i(t))$, where the sum of all mixing ratios at any given time is 1 (i.e. $\sum_i f_i(t) = 1$).

$$\Delta C_{pre} = \sum_i(\Delta f_i(t)\overline{C_{surf}} + \bar{f}\Delta C_{surf,i}(t)) \qquad \text{Eqn 3}$$

The first term (Eqn 3) represents changes in the end-member proportions, and the second term represents changes in their chemical composition. Changes in proportions and composition are assumed to be smaller than their mean values, so that the simultaneous anomalies in both ($\Delta f_i(t)\Delta C_{surf,i}(t)$) can be neglected.

In the context of the deep water mass of the North Atlantic, the surface origins of these endmembers could be locally contained in the subpolar North Atlantic (e.g. f_{surf} in Figure 3.1) or from outside of the subpolar North Atlantic (e.g. f_{ext} in Figure 3.1). This means that regional

changes in preformed concentrations can be driven by changes in the relative contribution of different endmember water masses, or by carrying C_{pre} anomalies from remote source locations. This decomposition provides a framework for analyzing the extent to which observed N_{pre} variability (and therefore N_{reg}) are controlled by biological uptake locally in the subpolar North Atlantic as opposed to water mass shifts or changes in N_{pre} originating outside the North Atlantic.

3.3 Methods

We investigated the O_2, NO_3, and temperature variability in the high latitude North Atlantic in the "deep" (100-700m, 35°W-15°W and 50°N-64°N) and the surface (0-50m, 30°W-15°W and 56°N-64°N) through a combination of direct observations and model simulations. We used historical hydrographic observations in the 2018 World Ocean Database (WOD18, Boyer et al. 2018), to quantify spatial and temporal variability. To aid in the interpretation of these observations and elucidate the mechanisms driving variations, we make use of simulations conducted with the Community Earth System Model (CESM). Hindcast simulations with CESM successfully reproduced the observed variations and were used to analyze the relationships between tracers and their decadal changes. The construction of observational anomalies and model simulations is described here.

The subpolar North Atlantic is among the most frequently sampled regions of the world ocean (Fig S1), particularly among those regions where deep-water formation occurs. In the surface region we analyzed, an average of 21 monthly nitrate observations are available in WOD18 per year, with a maximum of 88 in a single year. The 1950's and 1960's are the most sparsely sampled decades with only 39 monthly observations combined, but the other decades average 246 observations with a low of 103 (in the 2000's) and a high of 351 (in the 1970's).

The magnitudes of both the latitudinal gradient and the seasonal cycle of nitrate in our study region are large, so imperfect spatiotemporal sampling has the potential to bias analysis of regional changes over time. Nitrate concentrations reach 12 mmol m^{-3} in the winter and fall to 2 mmol m^{-3} in the summer, while the latitudinal gradient in annual sea surface nitrate is ~0.4 mmol m^{-3} per degree latitude (Fig S2). To minimize biases that could be introduced by uneven spatiotemporal sampling over time, we first binned hydrographic profiles onto a regular grid in order to calculate the monthly anomaly in nitrate, oxygen, and temperature for each observation in WOD18 relative to the climatological month at that location in the World Ocean Atlas 2018 (WOA18, Garcia et al. 2018). Using these climatological anomalies, we then compute $\frac{\Delta O_2}{\Delta T}$ and $\frac{\Delta N}{\Delta T}$ regression slopes, which represent the response of oxygen to warming or cooling temperatures and are controlled by both physical and biological processes. The spatial patterns of that variability are used to identify regions over which temporal variability is coherent enough to permit analysis of average regional trends in each tracer and the relationships between them.

To complement and deepen the analysis of direct observations, we use hindcast model simulations that reproduce both the mean state and overall trends in the variables of interest (Fig S2). The model output used for this study was from a "hindcast" integration of the Community Earth System Model (CESM; Yeager et al., 2018) with an ocean component integrated at a nominal horizontal 1^ox1^o resolution (the Parallel Ocean Program, version 2; Danabasoglu et al., 2012) with CORE2 physical surface forcing (Yeager & Large, 2008). The Biogeochemical Elemental Cycle ecosystem model simulates three explicit phytoplankton functional groups (diatoms, diazotrophs, and "small" picophyto-plankton/nanophytoplankton), and one implicit group (calcifiers; Moore et al., 2004) that experience multiple nutrient colimitation (N, P, Si, and Fe), although only N acts to limit growth in the North Atlantic. Bioavailable N in the well-lit surface is comprised of NO_3^- and

NH_4. Since nitrification is suppressed when photosynthetically active radiation exceeds 5.0 W m^{-2}, the source of nitrate to the surface is from vertical mixing, while NH_4 is produced by nitrogen fixation, phytoplankton mortality (e.g. grazing), remineralization, and excretion. The maximum phytoplankton growth rate (3.1 d^{-1}) is limited by nutrient availability via Michaelis-Menten kinetics, and is modified by T through $Q_{10}^{(\frac{T-30}{10})}$, where Q_{10} is 2.0 (Doney et al., 1996; Moore et al., 2004). We reduced the maximum growth rate of phytoplankton from 4.8 d^{-1} to 3.1 d^{-1} because we observed that NO_3 was reaching 0 mmol m^{-3} in summer, which does not coincide with available observations near Iceland in our study region.

By interpolating CESM output onto the 1°x1° WOD18 grid with its 102 depth levels, we are able to subsample CESM at the same temporal and spatial frequency available in the data. Using this subsampled model output, we compute the sensitivity of the $\frac{\Delta O_2}{\Delta T}$ and $\frac{\Delta N}{\Delta T}$ regression slopes to subsampling biases inherent in the empirical data.

3.4 Results

Historical observations reveal pronounced interdecadal fluctuations in subpolar North Atlantic thermocline oxygen content (Figure 3.2a) that are broadly similar to the patterns observed in the global upper ocean O_2 inventory (Ito et al., 2017). In the first decades of observations in the North Atlantic, annually averaged oxygen increased, reaching a peak in the 1980's before beginning a decline that has persisted since. Oxygen in the subpolar North Atlantic in CESM exhibits a similar multidecadal pattern to that of the historical observations. In both observations and model simulations, the temporal variability of O_2 averaged over the upper subsurface ocean (100-700m) of the North Atlantic is strongly correlated with anomalies in the heat content of those waters (Fig. 2b). The $\frac{\Delta O_2}{\Delta T}$ regression slopes are spatially coherent and of the same sign throughout

most of the subpolar North Atlantic; CESM captures these observed relationships quite well (Fig. 2c-d). $\frac{\Delta O_2}{\Delta T}$ represents the sensitivity of deep O_2 anomalies to changes in temperature and can be evaluated by rewriting Equation 2 as the sum of regression slopes $\frac{\Delta O_{2pre}}{\Delta T}$ and $\frac{r(\Delta N - \Delta N_{pre})}{\Delta T}$. Both terms can be directly evaluated in the model and when combined must equal the total $\frac{\Delta O_2}{\Delta T}$ relationship. We start by computing $\frac{\Delta O_{2pre}}{\Delta T}$ to determine how much of the thermocline oxygen variability in the subpolar North Atlantic can be accounted for by the subduction of oxygen anomalies driven by surface processes, including temperature-driven changes in gas solubility.

3.4.1 Preformed Oxygen

A significant fraction of deep oxygen anomalies originates in the upper ocean when the water parcels that comprise deep water were last at the surface. The oxygen concentration of any water parcel in the surface ocean (O_{2surf}) is set by the balance of photosynthesis, respiration, and gas exchange between the atmosphere and the ocean. On seasonal time scales, deepening mixed layers entrain old, biologically O_2-depleted water from below, replenishing O_2 as oxygen enters the surface ocean from the atmosphere. In the limit of infinitely fast gas exchange, O_{2surf} would be exactly equal to the thermodynamically saturated O_2 concentration (O_{2sat}) according to Henry's Law. However, the oxygen concentration of a water parcel at the surface is driven both by thermodynamic saturation (O_{2sat}) and a kinetic disequilibrium (hereafter O_{2diseq}). In a region that is dominated by deep wintertime convection, such as the subpolar North Atlantic, the timing and duration of deep convection determines which months most strongly transfer their surface oxygen signatures to the interior as O_{2pre}.

To evaluate which months control O_{2pre} in the deep North Atlantic in the model, we designed a passive dye tracer experiment where the tracer concentration in the deep at the end of

each month corresponds to the monthly f_{surf} in Figure 3.1. The tracer is continuously set to 1 in the surface cells in the region 60°W-0°W and 50°N-64°N and is then reset to 0 in every cell in the last time step of the month, which means any nonzero passive tracer concentrations present in the subsurface had to have been generated during that month. With this tracer construction, a monthly average concentration of 1 below the surface indicates complete equilibration between the subsurface cell in question and the surface ocean, while a concentration 0 indicates a complete lack of mixing. The average dye concentration in the depth range of 100-700m reaches almost 70% at its peak and shows that the most vigorous mixing occurs during winter when the mixed layer is deep from January through April. Exchange between the surface and the deep occurs throughout the whole year, but months with shallow mixed layers have very low, although nonzero, dye concentrations of less than 10%.

O_{2surf} anomalies in different months over the observational record from 1955-2010 therefore have varying degrees of impact on deep O_2 variability. Combined with the unequal importance of different months to the formation of O_{2pre}, the sensitivity of an arbitrary month's O_{2surf} to temperature anomalies between years also varies significantly ($\frac{\Delta O_{2surf}}{\Delta T}$, Figure 3.3b; black line). To partition the impact of changes in O_{2surf} on deep water O_2 into surface O_{2sat} anomalies and surface O_{2diseq} anomalies, we implemented a O_{2pre} tracer in the model: a biologically inert tracer that is set equal to [O_2] in the surface cell of the model that is then circulated by model physics. A water parcel's O_{2pre} in the model is exactly equal to the water parcel's initial surface O_2 concentration and is therefore the result of both thermodynamic forcing and the disequilibrium of gas exchange. The months that contribute the most to deep water formation have the largest influence on thermocline $\frac{\Delta O_{2pre}}{\Delta T}$ and coincide with periods where thermocline $\frac{\Delta O_{2pre}}{\Delta T}$ and $\frac{\Delta O_{2surf}}{\Delta T}$ regression slopes overlap (Feb-April, Figure 3.3a, b). Since $\frac{\Delta O_{2pre}}{\Delta T}$ does not change much over the

course of the year (Figure 3.3b, pink line), the $\frac{\Delta O_{2surf}}{\Delta T}$ signal that originates during the period of deep wintertime mixing is preserved as $\frac{\Delta O_{2pre}}{\Delta T}$ in the deep for the rest of the year.

Variability in monthly $\frac{\Delta O_{2surf}}{\Delta T}$ regression slopes (Figure 3b, black line) must be driven by more incomplete equilibration of deep winter mixed layers with the atmosphere during cold years ($\frac{\Delta O_{2diseq}}{\Delta T}$) because the change in equilibrium oxygen associated with surface temperature anomalies ($\frac{\Delta O_{2sat}}{\Delta T}$) does not vary much over the course of the year (Figure 3.3b, dashed black line). In colder years, the upwelled water is even more undersaturated because the thermodynamic O_{2sat} is higher, driving enhanced disequilibrium between O_2 in the surface ocean and O_2 predicted by saturation. This results in a disequilibrium effect that is acting in the opposite direction of the $\frac{\Delta O_{sat}}{\Delta T}$ relationship and therefore has a positive slope (Figure 3.3c). The combined influence of the disequilibrium effect and the change in gas solubility due to temperature results in a $\frac{\Delta O_{2pre}}{\Delta T}$ relationship of -5.8 in CESM and is comprised of $\frac{\Delta O_{2diseq}}{\Delta T}$ and $\frac{\Delta O_{2sat}}{\Delta T}$ of 0.7 mmol O_2 m^{-3} $^oC^{-1}$ and -6.5 mmol O_2 m^{-3} $^oC^{-1}$ respectively. The $\frac{\Delta O_{2pre}}{\Delta T}$ regression slope presented here accounts for 58% of observed interdecadal O_2 variability.

3.4.2 Nitrate variability in the North Atlantic

Below the surface, out of contact with the atmosphere and below the euphotic zone, a water parcel's oxygen can still change as a function of the respiration of organic matter (ΔO_{2res}). The ultimate source of this organic matter is photosynthesis at the surface, which results in a drawdown of surface nutrients that can be used to quantify the impact of local productivity on deep ΔO_{2res}. To evaluate the role of nutrient drawdown in the decadal O_2 changes, we analyzed historical observations of surface NO_3 (Fig. 4). In a broad swath of subpolar surface waters, annual NO_3

concentrations peak in the 1980's, along with cooler than average surface temperatures. Wintertime nitrate concentrations vary minimally year-to-year, but more stratification during warm years results in relatively lower summertime nitrate concentrations than in cooler years, suggesting that the net removal of nitrate from the surface may be a useful temperature sensitive metric for biological uptake on both seasonal and interdecadal timescales. Nitrate in the surface ocean is high at the surface in this region due to the upwelling of water with high concentrations of regenerated nitrogen. Much of that upwelled nitrate is carried into the subpolar North Atlantic via the nutrient stream that transports subsurface nitrate from the subtropics (e.g. in the density range $26.8<\sigma<27.5$, Williams et al., 2011).

Nitrate in the surface ocean of the subpolar North Atlantic is controlled by the balance of the physical nitrate supply and biological nitrate utilization that acts to remove nitrate from the surface. While nitrogen fixation and denitrification generally have the potential to influence surface nitrate, neither nitrogen fixation nor denitrification produce significant changes in surface nitrate here ($\Delta N \approx 0$ in Eqn 2), so the driver of surface N variability is therefore the balance of algal N uptake during growth and N supplied primarily via entrainment. To evaluate both of these temperature-sensitive mechanisms that can impart N_{surf} variability, we computed $\frac{\Delta N_{surf}}{\Delta T}$ regression slopes with climatological anomalies using the same strategy as described above for O_2. $\frac{\Delta N_{surf}}{\Delta T}$ varies month to month in CESM (-0.5 to -2, Figure 3.4a, black line) and to assess whether seasonal N variability in the model falls within empirical parameters, we identify months where $\frac{\Delta N_{surf}}{\Delta T}$ in the data is statistically significant. We spatially averaged the climatological anomalies of $[NO_3]$ and temperature to identify months where $p<0.05$ in WOD18 (black dots in Figure 3.4a). In

6 of the 8 months that have statistically significant relationships between nitrate and temperature, the $\frac{\Delta N_{surf}}{\Delta T}$ regression slope confidence intervals agree with observations (Figure 3.4c).

The data available in WOD18 in the top 50m in our study region in WOD18 (black dots, Figure 3.4b) has a $\frac{\Delta N_{surf}}{\Delta T}$ regression slope of -1.4±0.5, which coincides with the 95% confidence interval of the $\frac{\Delta N_{surf}}{\Delta T}$ slope in CESM. Although subsampling CESM based on the data availability in WOD18 reduces the $\frac{\Delta N_{surf}}{\Delta T}$ slope by ~30%, the subsampled model output is not significantly different from observations (Figure 3.4c). The relative sparseness of nitrate data in our study region (black box, Figure 3.4b, d) also makes it difficult to assess any spatial structure in the $\frac{\Delta N_{surf}}{\Delta T}$ in observations, although estimates using spatial averages and subsampling (Figure 3.4a, b) suggest that nitrate variability in CESM is not out of line with observations.

3.4.3 Preformed Nitrate: A tracer to evaluate O_{2res}

The drawdown of surface NO_3 during warm years and its export and subsequent remineralization in deeper water would account for an additional loss of deep O_2 during those periods. To diagnose the contribution of this process to the deep $\frac{\Delta O_2}{\Delta T}$ relationship, we estimate the slope of the relationship between T and both total N and N_{pre} in CESM, whose difference measures regenerated N (Eqn 2). We find that total NO_3 exhibits no significant variation with T in the deep water, indicating that any variations in N_{reg} (and thus O_{2res}) must be approximately equal in magnitude but opposite in sign to the changes in N_{pre}. To diagnose variations in preformed N in deep water and its connection to the overlying surface, we directly simulated a N_{pre} tracer. The N_{pre} tracer is set equal to NO_3 in surface grid boxes at each model time step and is transported conservatively elsewhere, identical to the simulation of O_{2pre} above. The simulated N_{pre} variations,

converted to O_2 units using the Redfield ratio closely correspond to the residual changes in ΔO_{2res} (Figure 3.5a).

ΔN_{pre} in the deep is ultimately driven by nitrate anomalies at the surface in months when deep water is being formed. To evaluate which months control ΔN_{pre}, we compute monthly linear regression slopes, $\frac{\Delta N_{pre}}{\Delta T}$, and compare them to the $\frac{\Delta N_{surf}}{\Delta T}$. In the same way that O_{2pre} is controlled by months with deep mixed layers and vigorous vertical mixing, the $\frac{\Delta N_{surf}}{\Delta T}$ values that most closely match $\frac{\Delta N_{pre}}{\Delta T}$ are during winter and the early spring (Figure 3.5b). As the mixed layer shoals from >500m in April to ~20m in July, $\frac{\Delta N_{surf}}{\Delta T}$ and $\frac{\Delta N_{pre}}{\Delta T}$ diverge because of enhanced stratification. However, even though mixing between the surface and deep is relatively weak during the summer, it is not completely shut off (refer to Figure 3.3a), so $\frac{\Delta N_{pre}}{\Delta T}$ is still influenced by biological activity even in the peak of the growing season.

Although $\frac{-r\Delta N_{pre}}{\Delta T}$ and $\frac{\Delta O_{2pre}}{\Delta T}$ together account for the entire $\frac{\Delta O_2}{\Delta T}$ slope (Figure 3.5c), changes in the contribution of remote waters from outside the North Atlantic could contribute to N_{pre} variability (and ultimately $\frac{\Delta N_{pre}}{\Delta T}$), even if surface nutrients were to remain constant (Eqn. 2). To separate the effect of remote forcing from local surface nitrate variability, we reconstruct N_{pre} using a simple end-member mixing model, where we write ΔN_{pre} as the sum of the fraction of each endmember (*f*) times the N_{pre} concentration along each boundary, $\Delta N_{pre} = fN_{surface} + fN_{subtropics} + fN_{deep}$. We added passive dye tracers to quantify the mixing ratios (*f*) of water from each of the boundaries of our deep North Atlantic box: the subtropics (set to 1 everywhere south of 50N and from 100-700m), the surface (set to 1 at 100m for the full North Atlantic from 50N-64N) and the deep (set to 1 at 700m over the full North Atlantic). When any dye passes

through a region associated with any of the other dye regions, it is set to 0 to eliminate double counting that could be caused by recirculation. After running the simulation to reach steady state with respect to the long-term dye inventories, the dye concentrations in the deep box then correspond to the fractional input of each endmember, where the sum of the dye concentrations is very close to one and the residual corresponds to the fourth endmember (the Arctic, north of 50N, which accounts for only a tiny fraction of total dye input).

The physical redistribution of water masses via mechanisms such as varying gyre speed could feasibly impart its own $\frac{\Delta N_{pre}}{\Delta T}$ because each endmember has different mean [NO_3]. Here, we use a Reynolds decomposition to separate fluctuations in N_{pre} associated with changes in water mass mixing ratios f ($\bar{N}\Delta f$) or changes in the [NO_3] of each endmember ($\bar{f}\Delta N$). The nitrate anomaly driven by the water redistribution effect ($\sum \Delta f \bar{N}$; Figure 3.6b, dashed blue line) cannot explain the interdecadal variations in N_{pre}, nor do any of its individual components exhibit variability that is synchronous with nitrate, temperature, or oxygen. Instead, the ΔN_{pre} time series is well captured by changes in endmember composition $\sum \bar{f}\Delta N$ (Figure 3.6b, dashed purple line). These changes can largely be accounted for the combination of $\bar{f}\Delta N_{surface}$ and $\bar{f}\Delta N_{subtropics}$ (Figure 3.6c), with only a small contribution from $\bar{f}\Delta N_{deep}$. It is unlikely that the incoming subtropical water would exhibit the same $\frac{\Delta N_{surf}}{\Delta T}$ as a region with deep wintertime mixing, so a large part of the incoming subtropical signal must be due to recirculation of the signal imparted to the water from the surface drawdown in the subpolar North Atlantic. The main mechanism is therefore simply variations in the magnitude of surface nutrient drawdown in the region of deep winter mixing, which is the spatially coherent $\frac{\Delta N_{surf}}{\Delta T}$ signal described above. Since the water mass redistribution effect is not a significant source of ΔN_{pre} interdecadal variability, then ΔO_2-ΔO_{2pre}

must therefore be driven by the combined influence of biological uptake and stratification on [N_{surf}].

3.4.4 Interdecadal variability in biological signal:

The efficiency of biological surface nitrate utilization is a key component of surface nitrate variability that drives most of the deep ΔN_{pre} (and therefore ΔO_{2res}). The difference in surface nitrate between warm and cold years ($\Delta N_{surf} = N_{surf,warm} - N_{surf,cold}$) reaches up to 1-2 mmol m^{-3} by the early spring (Figure 3.7a, black line) and is maintained for the rest of the growing season. Analogous to O_{2pre}, not all months are weighted equally: ΔN_{surf} in months with the highest surface-deep exchange ultimately controls ΔN_{pre}. To highlight which months are critical for ΔN_{pre}, we calculate $\bar{F}\Delta N_{surf}$ (Figure 3.7a, blue line), where $\bar{F}$ is the long-term mean mixing ratio of surface water in the deep diagnosed by the dye tracer experiment described above (e.g. Figure 3.3a). $\bar{F}\Delta N_{surf}$ highlights the significant influence of early phytoplankton nitrate uptake (April-July) in contrast with later months of the year that still have nontrivial ΔN_{surf}, but weak surface-deep exchange (low $\bar{F}$; August-November). The most pronounced difference in mixed layer depth between warm and cold years coincides with the largest $\bar{F}\Delta N_{surf}$ signal in May when the mixed layer is more than 100m shallower in warm years (Figure 3.7a, gray line).

Biological uptake of nitrate (J_{NO3}) is enhanced in warm years and drives ΔN_{surf} (Figure 3.7b, black line), which could be the result of decreased losses or increased production. However, enhanced JNO_3 coincides with higher rates of net primary production (μB; Figure 3.7b, green line), and so it is a result of enhanced growth and not reduced losses (e.g. through lower grazing rates). The accumulation of biomass in cold years starts approximately one month later (Figure 3.7c, green line) and reaches a maximum combined diatom and small phytoplankton biomass (B) ~20% smaller than in warm years. Phytoplankton growth in CESM is a function of light, temperature,

and nitrate, the limiting nutrient in the simulated North Atlantic. Computing μ by holding two of the three growth-controlling factors constant (nutrient limitation, light limitation, and temperature-dependent growth), we can evaluate μ anomalies produced by each factor. Stronger limitation of growth by both nutrients and light drive anomalously low NPP ($\mu\overline{B}$) in warm years (Figure 3.4). The warming intensifies light limitation through the self-shading effect of higher biomass in warm period, while the nutrient limitation gets stronger because of the nutrient drawdown itself. Thus, these factors work to oppose stronger N uptake in warm years and are consequences rather than causes of that trend.

The only remaining factor that can drive a positive Δμ in the early spring of warm years is temperature itself. Phytoplankton growth rates in CESM accelerate with temperature with a Q_{10} of 2.0 (Doney et al., 1996; Moore et al., 2004), resulting in a fractional increase, $\frac{\Delta\mu_T}{\mu_T}$, of approximately 5% per degree C (Figure 3.7c, gray line). The positive $\frac{\Delta\mu_T}{\mu_T}$ causes biomass to begin to accumulate as the mixed layer shoals at the onset of spring, resulting in larger NPP because the positive ΔB outweighs the negative $\Delta\mu$ associated with the concurrent nutrient and light limitation. Using a simple growth model to integrate the growth rate equation over 30 days $B_t = B_0 + \int_1^t \mu_{max} Q_{10}^{\frac{T-30}{10}} f_{nut} B_{t-1}$, it is straightforward to demonstrate that with CESM-like conditions (a total limitation term, f_{nut} = 0.85 and μ_{max} = 3.1 d^{-1}), a ΔT of 5% at 10°C is enough to produce a fractional increase, $\frac{\Delta\mu_T}{\mu_T}$, of 3.5% and a corresponding 50% increase in biomass by the end of the month. The exponential growth component of the growth equation causes seemingly small growth rate anomalies to produce substantial increases in biomass over the course of a single month. Empirical estimates of Q_{10} typically have a broad range, and a Q_{10} range from 1.5-3 produces a range of $\frac{\Delta\mu_T}{\mu_T}$ from 2.1%-5.7% for a ΔT of 5% at 10°C.

3.5 Discussion

Historical hydrographic observations in the subpolar North Atlantic reveal significant interdecadal changes in surface nitrate that mirror those in subsurface O_2: periods of warmer SST and OHC exhibit lower sea-surface nitrate along with reduced upper ocean oxygen content (Figure 3.8b,d-e). Our results suggest that the drawdown of surface nutrients during periods of warm upper ocean account for a substantial fraction of deoxygenation on decadal timescales. Differences in algal nitrate uptake associated with this interdecadal biomass variability drives corresponding preformed nitrate and O_{2res} anomalies and provides a mechanism for evaluating the sensitivity of the North Atlantic biological pump and oxygen to future changes in temperature. Future warming is expected to be accompanied by increased upper ocean stratification and our results predict the biological response to this warming could produce thermocline deoxygenation on the order of 4 mmol O_2 per degree.

The major factors that appear to have driven recent O_2 variability in the North Atlantic are coordinated through the North Atlantic Oscillation (NAO, Figure 3.8a), a low frequency climate mode of sea level pressure variability (Hurrell et al., 2003). The NAO shifted from a mostly negative phase at the beginning of the 50-year period we analyzed to a mostly positive phase in the latter half, accompanied by typically colder spring sea surface temperatures (Figure 3.8b) and deeper mixed layers at the onset of the spring bloom (Figure 3.8c). The correlation between the NAO and sea surface temperature in the North Atlantic is well documented (Bjerknes, 1964; Hurrell et al., 2003; Visbeck et al., 2001) and this low frequency temperature variability is a primary component of the $\frac{\Delta O_2}{\Delta T}$ and $\frac{\Delta N}{\Delta T}$ regression slopes that we have evaluated. Especially in the early 2000's, some SST and MLD anomalies do not perfectly covary with NAO, however, the SST/deep O_2 and MLD/NO_3 pairs remain tightly coupled over the entire time period.

A key underlying factor in this analysis is the value of 2.0 chosen for Q_{10}, which reduces growth rates at low temperatures typically associated with high latitudes (Moore et al., 2004). Empirical estimates of Q_{10} have a wide range and this formulation does not distinguish between community-level or species-level responses. Instead, the metabolic rates of all phytoplankton size classes (and zooplankton) vary synchronously. Despite the relative simplicity of Q_{10}, CESM produces an empirically reasonable $\frac{\Delta N_{surf}}{\Delta T}$ relationship that drives ~40% of the decadal variability in the simulation generated by temperature-driven changes in growth rates.

$\frac{\Delta N_{surf}}{\Delta T}$ may in fact drive more than 40% of the decadal variability in the real ocean because the empirical $\frac{\Delta N_{surf}}{\Delta T}$ derived from WOD18 data appears to be more negative than $\frac{\Delta N_{surf}}{\Delta T}$ in CESM. Incomplete monthly data coverage makes this comparison difficult, since the more negative $\frac{\Delta N_{surf}}{\Delta T}$ occurs in months with proportionally fewer data points. The largest discrepancy between $\frac{\Delta N_{surf}}{\Delta T}$ in WOD18 and CESM is in January and March, where $\frac{\Delta N_{surf}}{\Delta T}$ in WOD18 is very negative. However, if the real ocean's ΔN_{surf} was more temperature sensitive than that of CESM, then WOD18 should have a corresponding enhanced $\frac{\Delta O_2}{\Delta T}$ slope in the observations, but it does not. Along similar lines, there exists a two-fold range in the carbon to nitrogen ratio in suspended particles in the North Atlantic that is correlated with phytoplankton size and temperature that could enhance the sensitivity of nitrogen to temperature variability (Martiny et al. 2013). However, since the model has constant carbon to nitrogen ratios across phytoplankton species and a $\frac{\Delta O_2}{\Delta T}$ slope consistent with observations, this effect was not addressed explicitly in this analysis.

According to the textbook explanation for the onset of the spring bloom in the North Atlantic (Sverdrup, 1953), the period of rapid growth coincides with a period of stratification

where less vigorous vertical mixing of phytoplankton throughout the water column elevates photosynthetically active radiation above the light requirements for sustained growth. Analyses of satellite and float data in the North Atlantic have revealed that while phytoplankton growth still occurs when mixed layers are much deeper than the Sverdrup critical depth, the rapid shoaling of the mixed layer acts to accelerate biomass accumulation in the early spring (Mignot et al., 2018). Here, we have expanded on these recent results by demonstrating that variability in the timing and strength of the spring bloom driven by 1 degree C temperature anomalies can explain the variability in biomass accumulation on interdecadal timescales. The sensitivity of ΔO_{2res} to temperature-driven μ anomalies suggests an important consideration for other high latitude regions with high productivity, such as the Southern Ocean where historical data is relatively sparse.

3.6 Figures

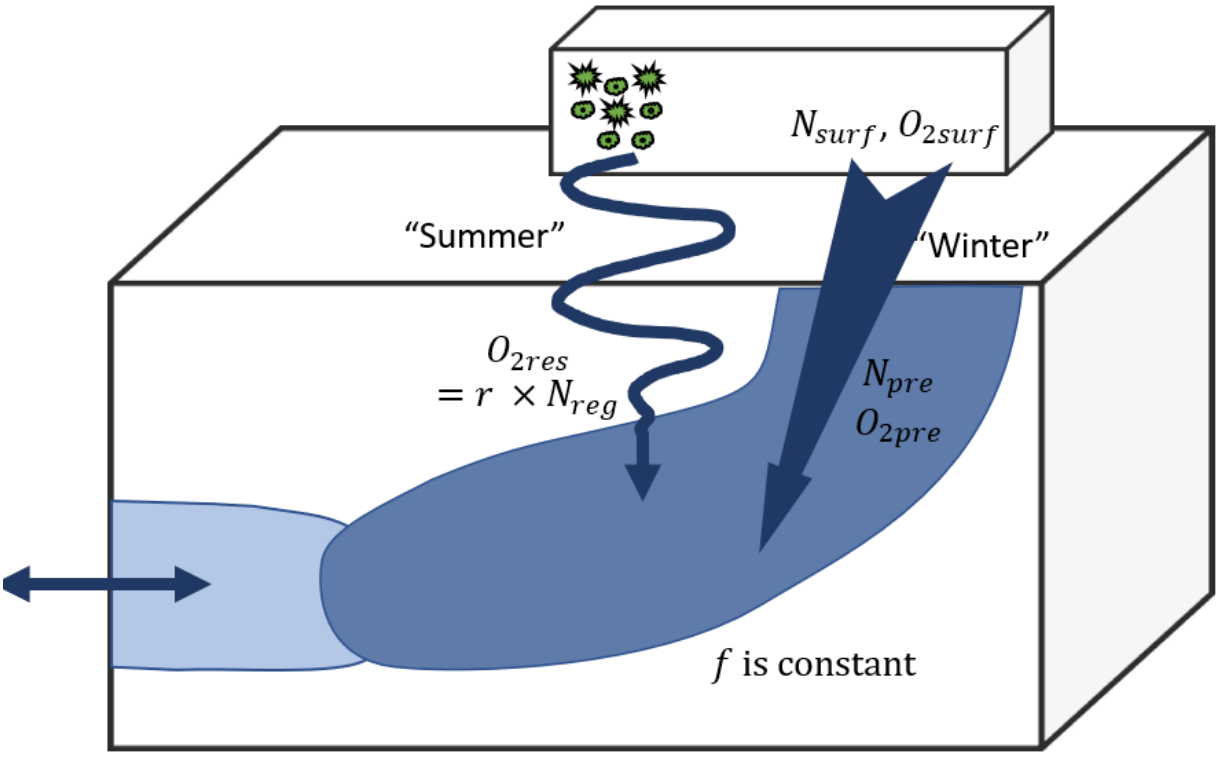

Figure 3.1**.** Conceptual model of the O_2 content in deep water. Deep water formation (primarily in winter) accounts for a fraction (f_{surf}) of deep water volume and carries the "pre-formed" concentrations of both O_2 and nutrients (N_{pre}) from surface waters to depth. Production of organic matter by phytoplankton (primarily in summer) is exported to deep water where it consumes O_2 and releases N_{reg} in an average ratio of -150:16 (r). The concentrations of the preformed tracers in the deep are the linear combination of surface water with water from outside the subpolar North Atlantic (f_{ext}).

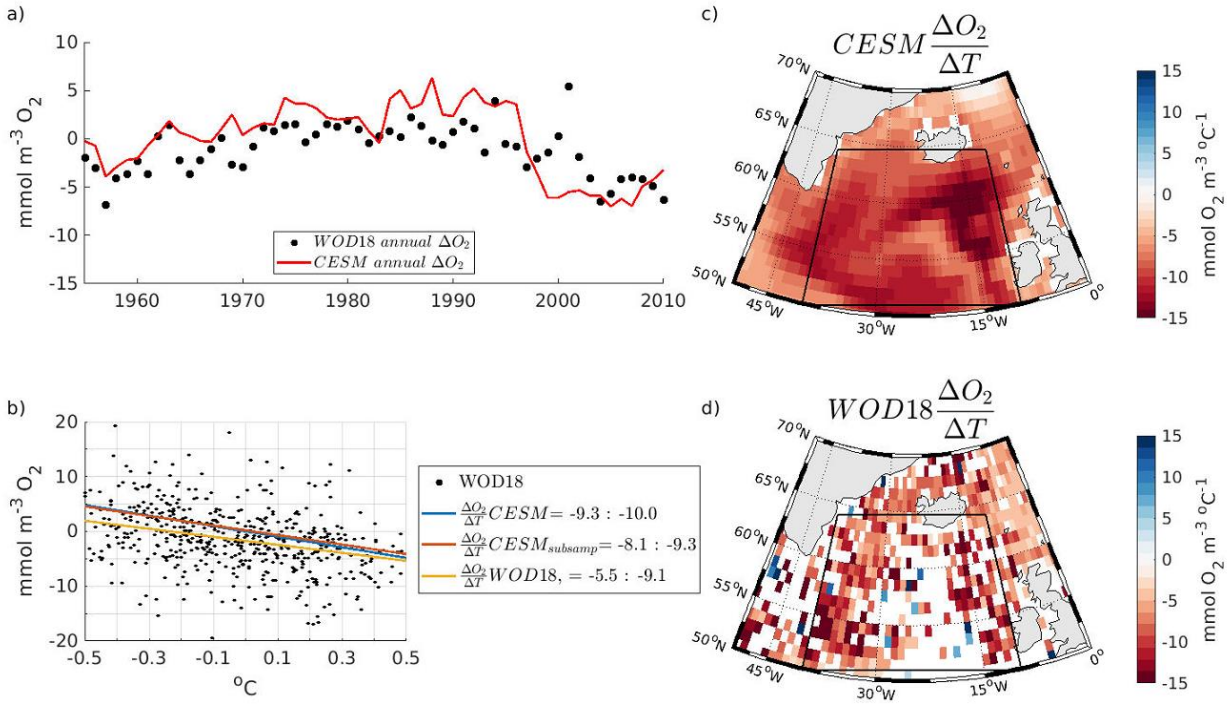

Figure 3.2. The interannual variability of oxygen and temperature in the subpolar North Atlantic. (a) [O_2] annually averaged from 0-700m in the subpolar North Atlantic from 35°W-15°W and 50°N-64°N in observations (WOD18, black dots) and the model (CESM, red line). (b) The change in oxygen associated with a change in temperature ($\frac{\Delta O_2}{\Delta T}$) calculated via linear regression from 0-700m using climatological anomalies as described in the text. The locations in WOD18 where the interannual $\frac{\Delta O_2}{\Delta T}$ regression slope is statistically significant (p<0.05) are shown (b, black dots). The range in the legend corresponds to the 95% confidence interval of $\frac{\Delta O_2}{\Delta T}$. $\frac{\Delta O_2}{\Delta T}$ is shown for WOD18 data, (-5.5:-9.1 mmol O_2 m^{-3} $^oC^{-1}$, yellow line), the full monthly CESM output (-9.3:-10.0 mmol O_2 m^{-3} $^oC^{-1}$, blue line) and CESM subsampled based on WOD18 data availability (-8.1:-9.3 mmol O_2 m^{-3} $^oC^{-1}$, orange line). Subsampling weakens the $\frac{\Delta O_2}{\Delta T}$ slope by roughly 10%, but both model estimates agree with the observed slope (b, yellow line). (c,d) $\frac{\Delta O_2}{\Delta T}$ averaged over the top 700 meters in CESM (c) and WOD18 (d).

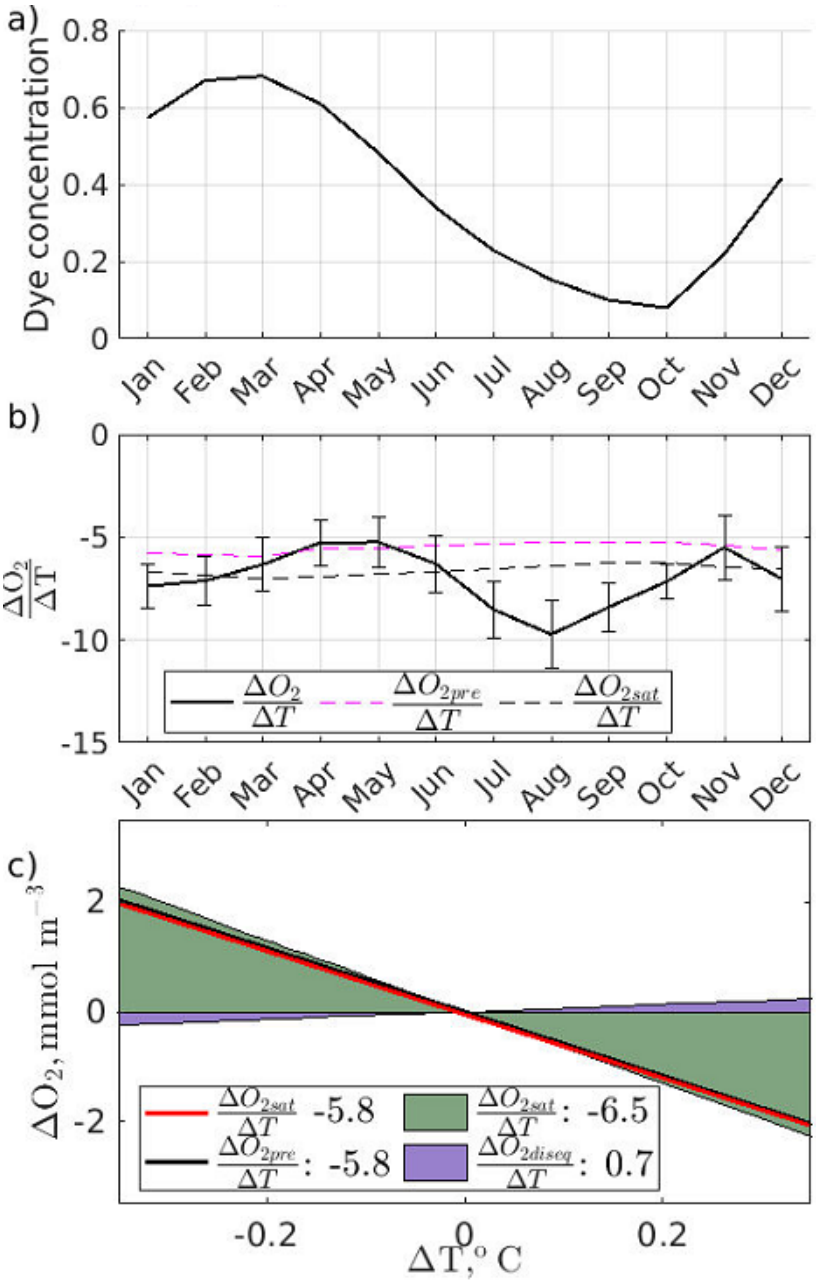

Figure 3.3**.** The mechanisms that drive variability in deep preformed O_2 in the subpolar North Atlantic. (a) The monthly fraction of deep water from the surface in CESM diagnosed from a dye tracer experiment designed to evaluate f_{surf} (Figure 3.1). The passive tracer used is continuously set to 1 at the surface and is reset to 0 in the last time step of each month. (b) $\frac{\Delta O_{2surf}}{\Delta T}$ (b, black line) and $\frac{\Delta O_{2sat}}{\Delta T}$ (b, dashed black line) regression slopes are calculated for each month using fluctuations

in monthly concentrations and temperatures in the surface (0-100m, 35°W-15°W and 50°N-64°N). The errorbars for $\frac{\Delta O_{2surf}}{\Delta T}$ correspond to the 95% confidence interval. $\frac{\Delta O_{2pre}}{\Delta T}$ regression slopes in the deep box (100-700m) are also shown. The Jan-June period corresponds to the highest f_{surf} values (a) and the period where $\frac{\Delta O_{2pre}}{\Delta T}$ in the deep overlaps with $\frac{\Delta O_{2surf}}{\Delta T}$, indicating a high degree of exchange between the surface and deep. (c) The decomposition of $\frac{\Delta O_{2pre}}{\Delta T}$ into $\frac{\Delta O_{2sat}}{\Delta T}$ (green shading) and $\frac{\Delta O_{2diseq}}{\Delta T}$ (purple shading) in CESM. O_{2pre} can be approximated by O_{2sat} in observations and the model $\frac{\Delta O_{2pre}}{\Delta T}$ (c, black line, -5.56 mmol m^{-3} $^oC^{-1}$) and observed WOD18 $\frac{\Delta O_{2sat}}{\Delta T}$ slopes (c, red line -5.79 mmol m^{-3} $^oC^{-1}$) are quite similar. The $\frac{\Delta O_{2pre}}{\Delta T}$ slope is simply the sum of the thermodynamic $\frac{\Delta O_{2sat}}{\Delta T}$ slope (c, green shading, -6.33 mmol m^{-3} $^oC^{-1}$) and the kinetic disequilibrium effect (c, purple shading, 0.78 mmol m^{-3} $^oC^{-1}$).

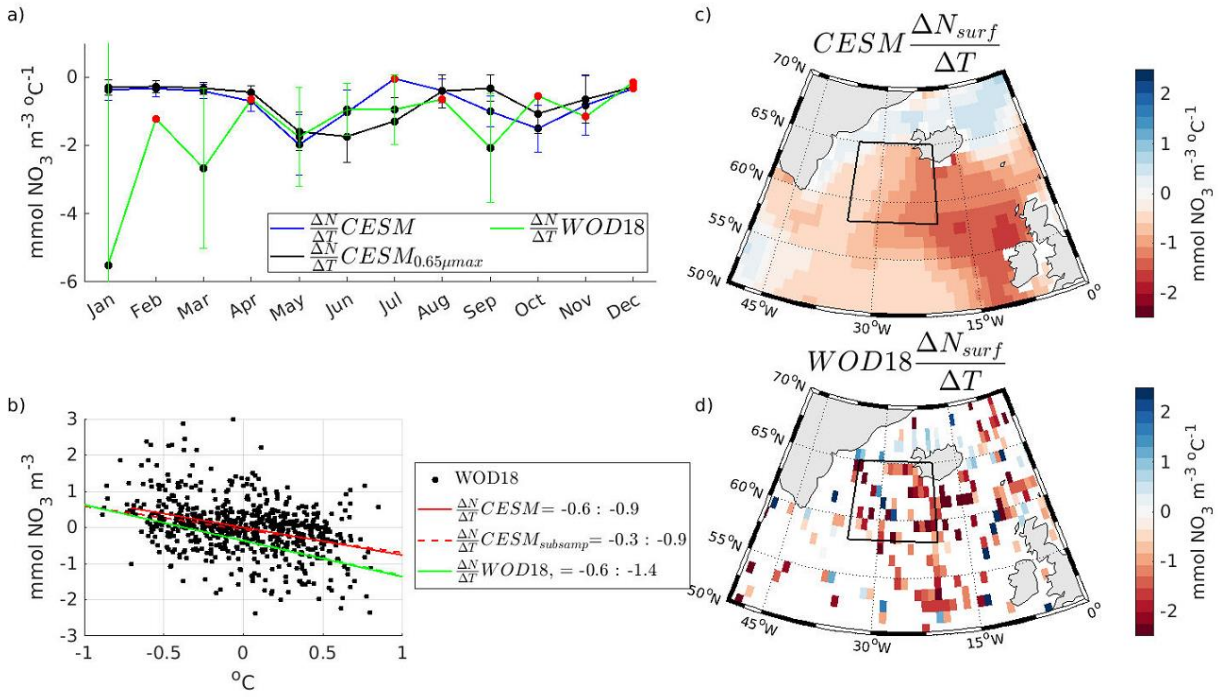

Figure 3.4**.** The spatial and temporal variability of the correlation between nitrate and temperature in the subpolar North Atlantic. All regression slopes are calculated using climatological anomalies as described in the text from 0-50m and between 15°W-35°W and 56°N-65°N. (a) Monthly $\frac{\Delta N_{surf}}{\Delta T}$ slopes in two model simulations (a, blue and black lines) and in WOD18 (a, green line), with 95% confidence intervals represented as the bars. Black dots indicate statistically significant relationships (p<0.05) and 6 of the 8 months with significant correlations agree between the model and the data. Reducing maximum local phytoplankton growth rates by 35% (from 4.8 d^{-1} to 3.1 d^{-1}) produces a statistically significant $\frac{\Delta N_{surf}}{\Delta T}$ slope in the summer months that is a better fit to data. (b) Monthly regression slopes calculated using monthly anomalies in CESM with full model output (b, red line) and subsampled data (b, dashed red line) have overlapping 95% confidence intervals with the data (b, green line). The locations in WOD18 where the interannual $\frac{\Delta N_{surf}}{\Delta T}$ regression slope is statistically significant (p<0.05) are shown (b, black dots). (c,d) The

spatial distribution of the $\frac{\Delta N_{surf}}{\Delta T}$ regression slopes in CESM (c) and WOD18 (d). Significant coverage gaps are present in the data, but the sign of the correlation and the magnitude are in general agreement between the two.

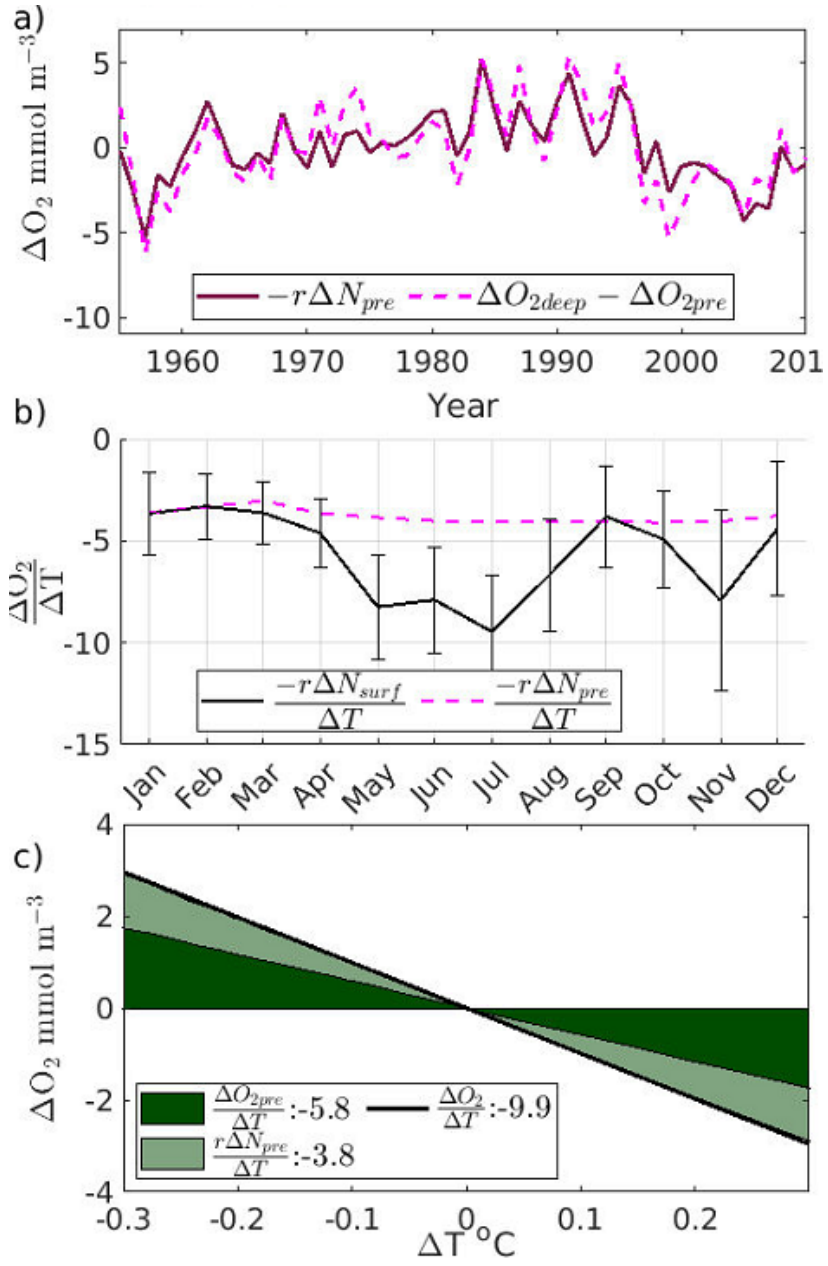

Figure 3.5**.** Accounting for ΔO_{2res} with ΔN_{pre} and surface nitrate. The relationship between annual anomalies of surface nitrate (0-50m, 35°W-15°W and 56°N-65°N), N_{pre} and thermocline ΔO_2 (100-700m, 35°W-15°W and 50°N-64°N) in CESM in the deep box (Figure 3.3c,d). (a) The comparison of ΔO_{2res} (calculated as $\Delta O_{2deep} - \Delta O_{2pre}$; dashed pink line) to $-r\Delta N_{pre}$ (the brown line), which shows that $-r\Delta N_{pre}$ is an accurate tracer for ΔO_{2res}. (b) The comparison of monthly $\frac{\Delta N_{surf}}{\Delta T}$ regression

slopes thermocline $\frac{\Delta N_{pre}}{\Delta T}$ (100-700m). $\frac{\Delta N_{surf}}{\Delta T}$ and $\frac{\Delta N_{pre}}{\Delta T}$ diverge in May, which suggests that the critical months where surface nitrate anomalies drive $\frac{\Delta N_{pre}}{\Delta T}$ in the deep occur in early spring. (c) The decomposition of the total $\frac{\Delta O_2}{\Delta T}$ slope in the thermocline into its $\frac{\Delta O_{2pre}}{\Delta T}$ (c, dark green) and $-r\frac{\Delta N_{pre}}{\Delta T}$ components, which together can account for the whole slope. The small discrepancy between $\frac{\Delta O_2}{\Delta T}$ and $\frac{\Delta O_{2pre}}{\Delta T} + -r\frac{\Delta N_{pre}}{\Delta T}$ must be due to ΔN (see Eqn 2).

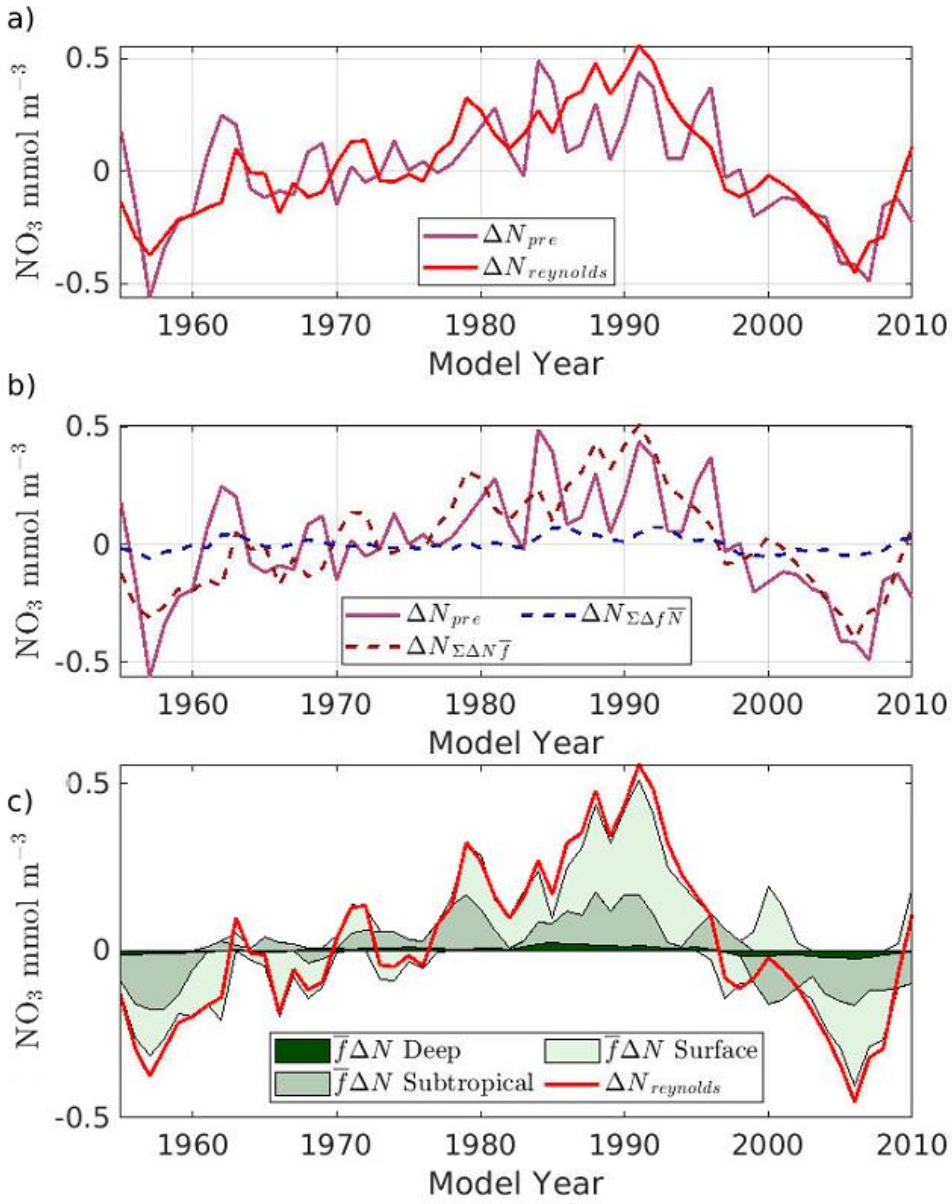

Figure 3.6. Reynolds decomposition of 100-700m annual ΔN_{pre}. We used passive tracers to evaluate the fractional input of the three source water endmembers in the North Atlantic (surface: 0-100m, 40w-10w, 56°N-64°N [NO_3], subtropics: 20°W-10°W, 50°N, 100-700m [NO_3], and the deep: 40°w-10°w, 50°n-64°n, 700m [NO_3]). (a) The reconstruction of ΔN_{pre} with mean and anomaly terms where $\Delta N_{pre} = N_{pre} - \overline{N_{pre}} = \sum \Delta f \overline{N} + \sum \bar{f} \Delta N$. We exclude the $\sum \Delta f \Delta N$ terms in the Reynold's decomposition and reproduce most of the variability in ΔN_{pre} (a, purple line) with

this method. (b) The sum of the products of the long-term mean and anomalies of endmember fractions and nitrate (b: $\sum \Delta f \bar{N}$ blue dashed line; $\sum \bar{f} \Delta N$, purple dashed line) compared to ΔN_{pre} (b, purple lines) shows that ΔN_{pre} is almost entirely due to $\sum \bar{f} \Delta N$. We show that the subpolar surface $\bar{f} \Delta N$ term (c, light green shading) is the largest contributor to the $\Delta N_{reynolds}$ time series (c, red line) with a nontrivial contribution from the subtropical $\bar{f} \Delta N$ term (c, green shading). The main control on ΔN_{pre} is the NO_3 concentration anomaly in the surface, which is at least partially recirculated via the gyre circulation and is implicitly included in the subtropical endmember. Anomalies in endmember source fractions do not impart interdecadal variability (b) in sync with deep O_2 (Figure 3.2) or surface NO_3 (Figure 3.5).

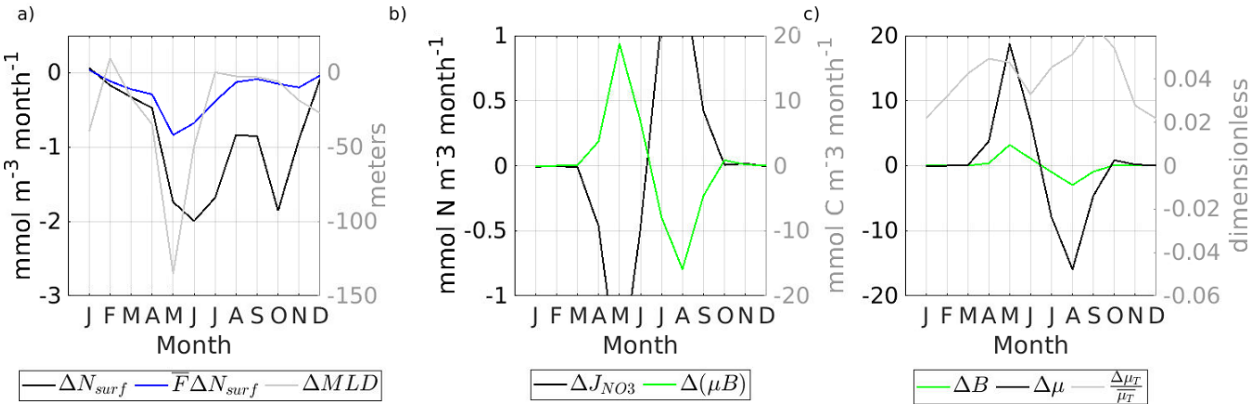

Figure 3.7**.** The ecological driving mechanism of the enhanced spring bloom during warm years. All panels display differences between warm years (e.g. 1958-1962) and cold years (e.g. 1989-1994) and are plotted using spatial averages in the surface box (see the black outline in Figure 3.4). (a) Monthly time series of ΔN_{surf} (ΔN_{surf} = $N_{surf,\ warm}$- $N_{surf,cold}$; black line) compared to ΔN_{surf} weighted by the mean surface endmember mixing ratio in the deep ($\Delta \bar{F} N_{surf}$, blue line) and ΔMLD (gray line). Early shoaling of the mixed layer coincides with anomalously low nitrate in warm years and $\Delta \bar{F} NO_3$ highlights the role of the months from April through July. (b) The monthly time series of changes in nitrate uptake by phytoplankton (ΔJNO_3; black line) compared to the change in net primary productivity between warm and cold years (Δ(μB); green line). The low nitrate in warm years is associated with enhanced ecological nitrogen uptake driven by higher net primary production during warm years. (c) The early accumulation of anomalously large biomass in warm years (green line) is driven by faster growth rates (black line). The increase in growth rates of approximately 5% per degree C (gray line) along with a shoaling mixed layer drives the positive biomass anomaly in warm years at the onset of the spring bloom.

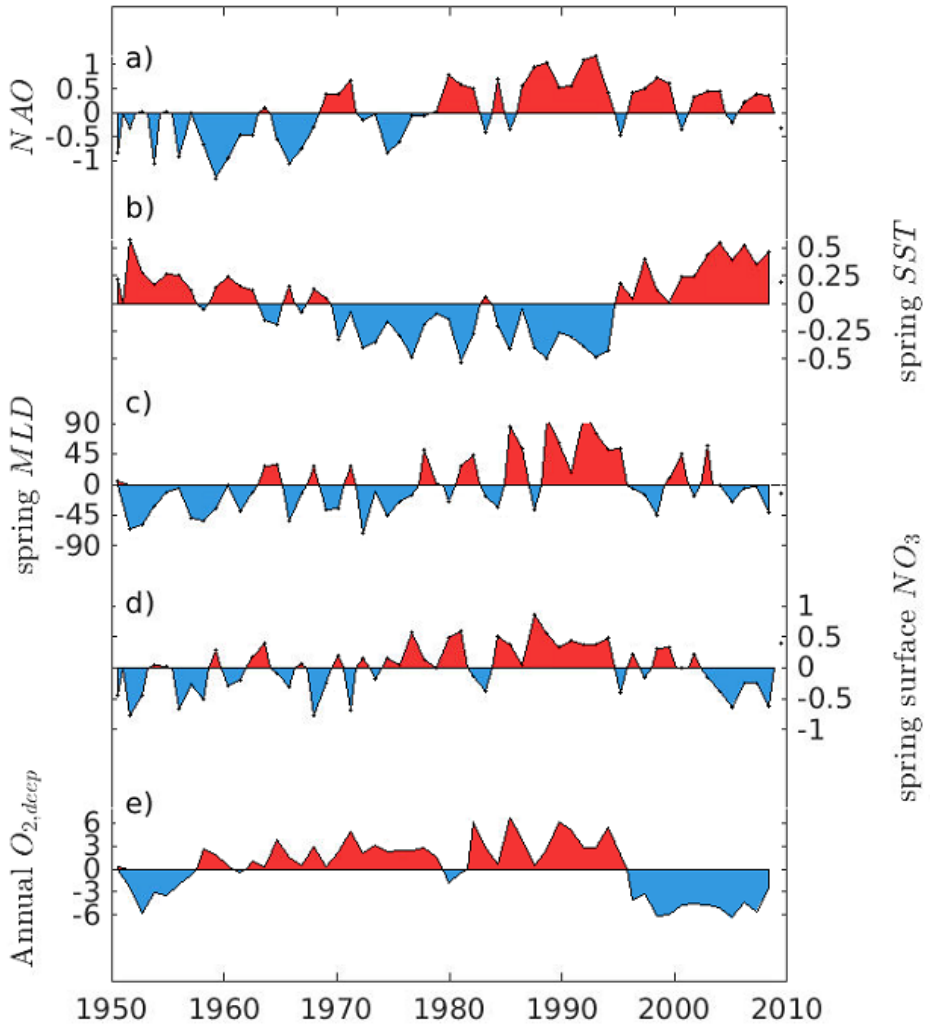

Figure 3.8**.** Subpolar North Atlantic variability correlated with the North Atlantic Oscillation (NAO). (a) NAO calculated using the months December-March. (b) March sea surface temperature in the top 50m. (c) March mixed layer depth. (d) March surface nitrate in the top 50m. (e) Annually averaged O_2 in the deep box used for this analysis (100-700m, 35^{o}W-15^{o}W and 50^{o}N-64^{o}N). NAO switches from mostly negative to mostly positive over the observational record and positive (negative) phases are generally associated with positive (negative) sea-springtime surface temperature anomalies (b) averaged over our study region (black box, Figure 3.4). During warm periods of the record, the MLD at the onset of the spring bloom (March) is shallower (c), which drives negative NO_3 anomalies as explained in the text (d). This biological signal, combined

with temperature-forced changes in gas equilibria produce a corresponding O_2 anomaly time series in the thermocline (0-700m, e) that varies synchronously with the other climate-related tracers.

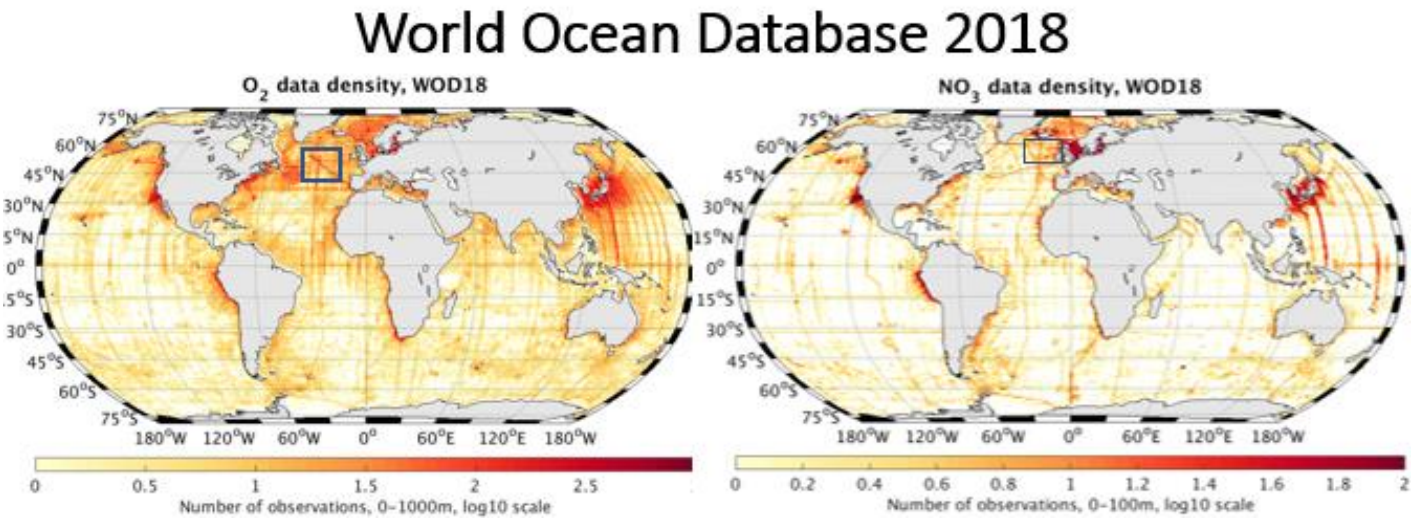

Supplemental Figure 3.1. Number of observations available in the top 0-1000m in the World Ocean Database 2018 for oxygen and nitrate. The North Atlantic a deep water formation region with relatively high data density of both nitrate and oxygen observations.

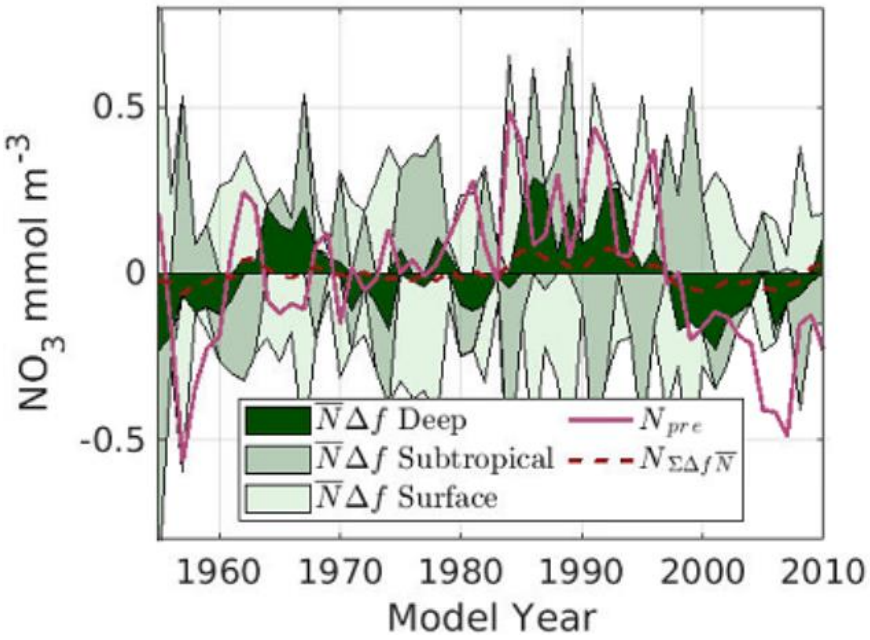

Supplemental Figure 3.2. The component of the Reynolds decomposition that corresponds to the annual 100-700m Δf. We used passive tracers to evaluate the fractional input of the three source water endmembers in the North Atlantic (surface: 0-100m, 40w-10w, 56°N-64°N [NO_3], subtropics: 20°W-10°W, 50°N, 100-700m [NO_3], and the deep: 40°w-10°w, 50°n-64°n, 700m [NO_3]). The deep $\overline{N}\Delta f$ term (c, dark green shading) is the most consistent with the interdecadal variability of ΔN_{pre}, but it is relatively small compared to the $\bar{f}\Delta N$ terms described in the text. The other $\overline{N}\Delta f$ terms that correspond to the subtropical input (medium green shading) and the subpolar surface ocean (light green shading) act in opposition to each other and do not exhibit the same interdecadal variability as ΔN_{pre}.

Chapter 4

THE STRENGTH AND EFFICIENCY OF THE BIOLOGICAL CARBON PUMP IN THE TROPICAL PACIFIC

Abstract

The biological carbon pump in the equatorial Pacific is an important sink of CO_2 as carbon is converted to particulate and dissolved organic matter and exported to the deep. Satellite chlorophyll-based estimates predict enhanced biological productivity along the equator relative to the subtropics, similar to many global coupled biogeochemical-circulation models. However, estimates from these various sources often differ from each other and conflict with direct geochemical measurements. We present results from a 25km resolution ROMS simulation that reproduces hydrographic and float-based observations of temperature, salinity, and oxygen supersaturation in the Equatorial Pacific and evaluate the accuracy of integrating ANCP down to the maximum annual mixed layer depth using the carbon mass balance. By varying the maximum growth rate of phytoplankton in a suite of ROMS simulations, we demonstrate that only the simulations with zonally averaged equatorial NCP values of 6.5±0.5 mol C m^{-2} yr^{-1} (4^oS to 4^oN) and off-equatorial NCP values of 4±0.2 mol C m^{-2} yr^{-1} (4^oS to 15^oS combined with 4^oN to 15^oN) reproduce the empirical sea-surface nitrate distribution in the tropical Pacific. We show that at steady state, the carbon sequestered in the tropical Pacific in a high-resolution model constrained by data is 3.26 mol C m^{-2} yr^{-1}. Of that carbon flux, ~52% (1.7 mol C m^{-2} yr^{-1}) is in the form of dissolved organic carbon and the remaining 48% (1.56 mol C m^{-2} yr^{-1}) is sequestered as DIC. Of the total net organic matter production in the model (4.7 mol C m^{-2} yr^{-1}), roughly 30% does not result in a net increase in regional long term carbon sequestration and therefore must either efflux

to the atmosphere or be recycled by phytoplankton. Finally, we use Lagrangian particle tracking experiments to define depth horizons that correspond to water parcel sequestration timescales ranging from 0 (τ_z^{0yr}) to 2 years (τ_z^{2yr}). We show that 77% of net respired carbon production in the western equatorial Pacific occurs in water above τ_z^{2yr} (2.0 of 2.6 mol C m^{-2} yr^{-1}), compared to only 12% in the eastern equatorial Pacific (0.5 of 4.2 mol C m^{-2} yr^{-1}). Respired carbon produced in the eastern Pacific is therefore significantly more likely to remain sequestered on long timescales.

4.1 Introduction

The ocean plays an important role in the global carbon cycle as it removes large amounts of CO_2 from the atmosphere by transferring carbon from the surface to the deep ocean. A key component of the ocean's ability to export carbon to the deep is the biological carbon pump, where biological activity converts dissolved inorganic carbon in the surface ocean into organic matter that can be exported below the surface ocean and sequestered from the atmosphere on timescales of months to years (Giering & Humphreys, 2018). The net production of organic matter by an ecosystem is referred to as Net Community Production (NCP) and is a result of the difference between net carbon fixation by autotrophs (net primary productivity; NPP) and heterotrophic respiration. The organic carbon produced in the surface ocean can be transferred to the deep ocean as sinking particles, the advection of neutrally buoyant dissolved organic matter, or through vertical motion of swimming organisms such as zooplankton. Where and how much organic matter is produced influences how much carbon is exported from the surface ocean and the timescales on which it is kept out of contact with the atmosphere for months to decades.

Estimates of the strength of the biological carbon pump vary across models, satellite algorithms, and geochemical estimates, which range from 7 to 13 Pg C when accounting for the export of dissolved organic matter (Quay et al., 2020). The biological carbon pump is a function of both NPP and the fraction of organic carbon that is exported below the surface ocean, so uncertainty in estimating NPP contributes directly to uncertainty in estimating the strength of the biological carbon pump. Globally, satellite-derived estimates of net primary production agree to within 4% of each other (50 Pg C ±2; Quay et al., 2020), although regional estimates of NPP vary by a factor of 2-3 in equatorial and high latitude oceans (Figure 4.1b). Models and satellites predict a strong biological pump at the equator, where upwelled nutrients feed local production (Field et

al., 1998; Laufkötter et al., 2016), but both modern global circulation models (GCMs; Figure 4.1a) and satellite algorithms (Figure 4.1b) disagree on the relative magnitude of equatorial NPP compared to high latitudes. While equatorial productivity is elevated relative to subtropical productivity across GCMs and satellites, both the absolute magnitude of equatorial NPP and latitudinal NPP gradients are uncertain, which drives uncertainty in estimates of the equatorial biological carbon pump.

Even if the strength of the biological carbon pump were perfectly known, not all organic carbon produced in the surface ocean is sequestered equally (DeVries et al., 2012). For the purpose of this analysis a water parcel is considered sequestered if it is remains below the mixed layer and carbon is considered sequestered if it is prevented from escaping to the atmosphere within the model domain. The length of time a water parcel remains below the mixed layer can vary on the order of months to millennia and sequestration is therefore dependent on the timescale of interest.

The amount of organic carbon sequestered and the duration of its sequestration in any region is controlled by how much organic carbon is produced, where it is respired, and how long the water containing that respired carbon is kept out of contact with the atmosphere once it leaves the surface ocean. While physics controls how long subsurface water parcels remain away from the surface, other factors such as particle sinking rates and the rate of organic matter degradation dictate where that organic carbon is respired in the water column. For example, in regions where significant portions of organic carbon is respired above the annual maximum mixed layer, the mixed layer deepening during winter reentrains locally respired carbon and prevents it from being sequestered on timescales longer than one year (Körtzinger et al., 2008; Palevsky et al., 2016; Palevsky & Doney, 2018, 2021). In mode water formation regions, the carbon that escapes reentrainment by the deep winter mixed layer is likely to be remain below the surface and out of

contact with the atmosphere for much longer than one year. The effective reduction in the amount of carbon exported in these regions due to reentrainment can be accounted for by integrating NCP down to the annual maximum mixed layer.

However, in regions where there is strong upwelling and horizontal advection, such as in the equatorial Pacific, locally respired carbon may be brought back to the surface on timescales that are not dependent on the depth of the winter mixed layer. In regions dominated by horizontal and vertical advection and not mixed layer variability, the transport of a water parcel to the surface ocean could take longer than a year but still occur on relatively short timescales. Even the carbon that is sequestered for one year is therefore not guaranteed to be climatically relevant. In model studies of the equatorial current system, particle tracking experiments demonstrated that water parcels could be recirculated up to 6 times over two years, (e.g. Figure 11 in Liu et al., 1994) which suggests that a single water parcel may have multiple opportunities to release locally respired carbon back to the atmosphere as CO_2 in this region.

In Part I, we evaluate tropical Pacific NCP in a model constrained primarily by nitrate data and use an independent estimate of carbon sequestration to evaluate the accuracy of integrating net organic carbon production to different integration depths in the tropical Pacific in ROMS. In Part II, we evaluate how much carbon is sequestered on timescales from 0 to 2 years using the combination of the steady state carbon mass balance and a Lagrangian particle tracking algorithm (Pyticles; Gula et al., 2014).

4.2 Equatorial circulation dynamics

Empirical observations reveal that the surface ocean in the eastern Pacific is colder, more nutrient rich, and less saturated with respect to oxygen than the west. (Figure 4.2a-c). The “equatorial cold tongue” varies in intensity inter- and intra-annually and is sustained by the nutrient

rich water that is upwelled to the surface (Ray et al., 2018). The dominant vertical flow is upwelling produced by the pattern of wind stress along the equator that upwells water from the Equatorial Undercurrent (EUC). The EUC is a strong eastward flowing subsurface current that plays a major role in oxygen and nutrient supply to the eastern Pacific (Cromwell et al., 1954; Rosales Quintana et al., 2021). The water being upwelled to the surface is undersaturated with respect to O_2 due to the combination of cold temperatures (and therefore high equilibrium O_{2sat}) and accumulated respiration since the last time the water outcropped. Based on analysis of nitrogen isotopes, equatorial surface nitrate has been shown to be dominated by the upwelling of EUC water and not by other sources such as the westward surface transport of high nutrient water from more eastern sources (Rafter & Sigman, 2016).

In addition to the influence of the EUC, a complex array of zonal, meridional, and vertical circulations impacts the distribution of biogeochemical tracers such as nutrients, chlorophyll, and temperature. To the north and south of the equator, shallow overturning cells have the potential to subduct recently upwelled water (Liu et al., 1994). In addition to vertical motion associated with these overturning cells, water is advected meridionally by Tropical Instability Waves, westward propagating eddy-like perturbations that carry water to and away from the equator (TIWs; Jochum & Murtugudde, 2006). TIWs also impart vertical velocities, where an arbitrary location at the surface can experience upwelling or downwelling as a TIW passes. This alternating series of downwelling and upwelling water brings water back into the interior, where it can be incorporated into the Equatorial Undercurrent (EUC) and carried back east. The shallow parts of the EUC experience both local recirculation via the equatorial cells and incorporation of tropical surface waters from above (Liu et al., 1994). This complex exchange of surface and subsurface water that results from the interaction of the EUC, TIWs, and the prevailing westward surface flow causes

water parcel recirculation during their westward transit (Liu et al., 1994). Evaluating carbon export explicitly in this system is therefore complicated by 3-D recirculation and choosing a time period and depth horizon for integrating NCP is not a straightforward task.

4.3 Methods

To evaluate carbon sequestration in the tropical Pacific, we use an eddy-permitting ROMS (Shchepetkin & McWilliams, 2005) with an embedded ecosystem model (Moore et al., 2004). The model has been extensively validated against numerous observations in the eastern North Pacific (Durski et al., 2017; Renault et al., 2016) and the configuration used in this study was checked against thermocline temperature (Supplemental Figure 4.1). The model domain covers the tropical Pacific from 15^{o}S to 15^{o}N, with a horizontal resolution of 25 km and 42 vertical sigma levels. The ecosystem model has three functional groups of phytoplankton (small phytoplankton, diatoms, and diazotrophs), with multiple growth-limiting nutrients (nitrate, phosphate, ammonium, silicate, and iron), zooplankton grazers, and an implicit particle flux (Armstrong et al., 2001). The routing of organic carbon pools into dissolved organic carbon (DOC) and dissolved inorganic carbon (DIC) is prescribed for individual ecosystem processes such as grazing and mortality, where the grazing and mortality of smaller phytoplankton produces a higher fraction of DOC relative to DIC when compared to the grazing and mortality of diatoms. A climatology derived from a hindcast configuration of the Community Earth System Model (Yeager et al., 2018) was used for the biogeochemical boundary conditions and initial conditions are from the World Ocean Atlas 2018 (WOA18, Garcia et al 2019) . Monthly climatological surface winds and buoyancy forcing are derived from a global climatology based on Quikscat scatterometer data (Risien & Chelton, 2008). The model was spun up for 30 years until thermocline nutrient inventories stabilized. We chose a remineralization length scale of 200m and a q_{10} of 2.0 for the implicit particle flux profile (similar

to the *q10* in Doney et al., 1996), which was required to match the subsurface nitrate inventories (Supplemental Figure 4.2).

In the equatorial Pacific surface ocean, productivity is limited by iron availability (Landry et al., 2000) in contrast to the subtropical gyres, where nutrient limitation transitions to being controlled by nitrate availability (Saito et al., 2014). While iron is a key limiting nutrient, especially in the eastern Pacific, iron biogeochemistry is complex as it is the result of many sources including hydrothermal vents, dust, and sediments. Models represent iron biogeochemistry differently and produce disparate iron distributions throughout the water column (Tagliabue et al., 2016). Furthermore, iron biogeochemistry is further complicated by the need for substantial iron recycling (Fe:C) to account for the rate of nitrate removal in the equatorial Pacific (Rafter et al., 2017). In contrast, nitrate removal from the surface ocean as it upwells produces a vertical and poleward nitrate distribution that results from the interplay of nitrate residence times in the surface ocean and the net biological removal of nitrate. Based on these considerations, we leverage the effective latitudinal gradient between equatorial and subtropical Pacific surface nitrate to constrain equatorial and off-equatorial NCP.

NCP and the rate of carbon sequestration both depend on the growth rate of phytoplankton who are responsible for photosynthetic uptake of DIC. The growth rate of phytoplankton in the model is controlled by nutrient and light availability and is slower at lower temperatures. When nutrients are replete, additional nutrients do not drive increases in productivity. By varying the maximum growth rate of phytoplankton (μ_{max}), we produced a suite of simulations that span a wide range of NCP. We present model results from four simulations with μ_{max} ranging from 0 d^{-1} to 1.5 d^{-1} that were extended for an additional 30 years to reach steady state tracer inventories. The ecosystem was turned off completely in one abiotic simulation ("no BEC", where all ecosystem

terms are 0, including μ_{max}). This suite of model simulations was used to constrain model NCP and the results are discussed below.

4.3.1 Estimating carbon export in the model

The net biological production of oxygen (J_{O2}) and the oxygen consumed during the aerobic degradation of organic matter are stoichiometrically related to carbon production and consumption by the Redfield ratio (Anderson & Sarmiento, 1994; Körtzinger et al., 2001; Takahashi et al., 1985). Due to this stoichiometric relationship, net biological carbon production can be estimated by annually integrating J_{O2} (the rate of $O_{2,production} - O_{2,consumption}$) from the surface to some depth. The theoretical upper bound on biological carbon export is JO_2 integrated above the compensation depth (NCP_{comp}), where net biological O_2 production transitions to net consumption. The fraction of NCP_{comp} that escapes to the atmosphere (Φ) is a measure of how much locally respired carbon is lost to the atmosphere instead of sequestered. As discussed above, carbon respired above the depth of the maximum annual mixed layer (NCP_{MLD}) has the potential to be reentrained, which reduces the effective carbon export over the annual cycle in areas where this is a significant effect. We define the mixed layer by evaluating the depth at which water is 0.03 kg m^{-3} different than the surface density and we evaluate this quantity for each grid cell on a monthly basis. To assess the accuracy of NCP_{MLD} in accounting for the effective Φ in the tropical Pacific and to evaluate how much of the carbon exported below the surface ocean remains there, we need to quantify carbon sequestration directly in the model ($(1-\Phi)NCP_{comp}$). We accomplish this by comparing the abiotic and biotic carbon mass balance in the full model domain.

In the tropical Pacific (15°S-15°N in this analysis), the net flux of CO_2 is to the atmosphere (Ishii et al., 2014). The carbon that supports this CO_2 efflux is ultimately supplied from below by the net supply of dissolved inorganic carbon in the deep at the model's open ocean boundaries.

The biological process of converting dissolved inorganic carbon in the surface ocean of the tropical Pacific into dissolved and particulate organic carbon reduces the concentration of DIC in the surface ocean and therefore the net flux of CO_2 to the atmosphere. In the absence of biology, there is still a net supply of DIC in the deep because of the open ocean boundary conditions (T_{DIC}^{abio}, Figure 4.3a) and the outgoing flux of CO_2 at the surface ocean is equal and opposite to the net supply of DIC to the model domain ($FG_{CO2}^{abio} = -T_{DIC}^{abio}$; Figure 4.3a). The outgoing CO_2 flux without biology is larger because there is no biological carbon pump acting to reduce the surface DIC concentration. Overall, biology acts to transfer carbon that would escape via gas exchange from the surface ocean in the tropical Pacific into organic carbon that can leave the surface ocean horizontally (as DOC) or vertically (as vertically advected DOC and sinking POC). Vertical export of DOC to the subsurface can occur in areas away from the upwelling zone within the model domain (e.g. subduction in the subtropical gyre or downwelling to the north and south of the equator) or by diffusion, but most of the vertical loss of organic carbon to the deep occurs as POC. If that vertically exported organic carbon is respired in water that does not come into contact with the atmosphere again within the model domain, then it is sequestered.

The outgoing CO_2 flux is therefore a useful tool for measuring the impact of the biological carbon pump in the model. Any mole of organic carbon produced by the ecosystem that is not respired within reach of surface gas exchange results in a net reduction in the outgoing CO_2 flux relative to the abiotic simulation ($C_{sequestered} = \Delta FG_{CO2} = FG_{CO2}^{bio} - FG_{CO2}^{\text{abio}}$). The following equations refer to the carbon mass balance for the full water column from the ocean surface to the ocean floor and over the entire model domain from 15°S to 15°N (Figure 4.3a,b). The carbon mass balance in the abiotic simulation is very simple: The net advective and diffusive carbon supply of

DIC in the abiotic simulation (T_{DIC}^{abio}) at the open ocean boundaries is balanced at steady state by the net efflux of CO_2 at the surface (FG_{CO2}^{abio}).

$$\frac{dDIC_{abio}}{dt} = T_{DIC}^{abio} + FG_{CO2}^{abio} \quad (4.1)$$

With the ecosystem turned on, the full time-dependent evolution of carbon over the entire water column within the model domain can be written as the sum of the net flux of dissolved inorganic and dissolved organic carbon across the model boundaries at 15°S and 15°N ($T_{DIC} + T_{DOC}$) and the air-sea flux of CO_2 (FG_{CO2}).

$$\frac{dC}{dt} = T_{DIC} + T_{DOC} + FG_{CO2} \quad (4.2)$$

The net source of DIC to the model domain via transport (T_{DIC}) must be in balance with the net sinks of DIC. T_{DIC} integrated over the full model domain includes both the net influx of DIC in the deep and the net efflux of DIC in the surface. T_{DIC} is therefore directly influenced by processes that export DIC from the surface ocean to the deep and by processes that convert DIC to organic carbon. The primary way that DIC is transferred to the deep is through the export of POC, which means that T_{DIC} contains information about POC export in the biotic simulations. Ultimately, DIC that is converted to organic carbon by phytoplankton in the surface ocean (NCP) must be respired inside or outside of the model domain. Organic carbon can exit the model domain as dissolved organic carbon (T_{DOC}) if it reaches the model boundaries before the DOC is respired or as particulate organic carbon if it reaches the ocean floor as particulate matter. However, the flux of particulate organic carbon at the ocean floor is small and so we exclude it from Equation 4.2. DIC produced by the respiration of organic carbon within the model domain in the surface ocean (or by respiration in subsurface water that is brought to the surface) can escape to the atmosphere via gas exchange as CO_2. Alternatively, the respiration of organic carbon below the surface ocean (primarily via the degradation of POC) that produces DIC that remains out of contact

with the atmosphere within the model domain directly influences the net transport of DIC in the deep (i.e. the deep component of T_{DIC}). it.

The organic carbon that leaves the surface ocean as sinking particulate matter or vertically advected DOC is respired by heterotrophs (R_h in Figure 4.3b) in water that either remains out of contact with the atmosphere (i.e. the carbon is sequestered) or in water that is transported back to the surface ocean and is released back to the atmosphere as CO_2. The fraction of NCP that is lost to the atmosphere within the model domain is denoted by Φ in Figure 4.3b. The addition of respired carbon in the subsurface as organic matter is consumed increases the concentration of DIC in the deep and ultimately reduces the net transport of DIC into the domain (T_{DIC}) by weakening the gradient between the incoming high DIC water and the deep water in the model domain. Together, the changes in transport of DIC and DOC must balance the reduction in outgoing CO_2 flux at the surface of the ocean in the biotic simulation compared to the abiotic simulation ($\Delta FG_{CO2}^{bio-abio}$).

The impact of the biological carbon pump on outgoing CO_2 is shown by Equation 4.3, where all Δ terms are written as the difference between the biotic and abiotic simulations. An alternate solution that demonstrates that Equation 4.3 can be derived from a 2-box model system is shown in the Supplemental Discussion.

$$\Delta FG_{CO2}^{bio-abio} = \frac{\Delta dDIC}{dt} - \Delta T_{DIC} - \Delta T_{DOC} \qquad (4.3)$$

$\Delta FG_{CO2}^{bio-abio}$ represents the organic carbon that is respired out of reach of the atmosphere within the model domain ((1-Φ)NCP) and we use this analysis to decompose the outgoing carbon fluxes into the fluxes driven by DOC and DIC. Generally, any carbon that is prevented from escaping to the atmosphere within the model domain by the biological carbon pump must be represented by either a change in either ΔT_{DOC} or ΔT_{DIC}. We calculate ΔT_{DOC} at steady state and use the residual between $\Delta FG_{CO2}^{bio-abio}$ and ΔT_{DOC} to evaluate the remaining carbon flux that is due

to the biological carbon pump. As discussed above, since T_{DIC} in the biotic simulation is directly influenced by the export of organic carbon to the deep, then the difference between DIC transport in the biotic and abiotic simulations (ΔT_{DIC}) includes the impact of sinking POC on carbon sequestration.

4.3.1 Lagrangian Particle Tracking

To evaluate the efficiency of water parcel sequestration (and therefore carbon sequestration), we computed water parcel trajectories in an offline Lagrangian particle tracking model, Pyticles (Gula et al., 2014). Pyticles uses a 4th-order Runge-Kutta scheme to calculate the 3D advection of massless and dimensionless particles. The position (*P*) of a water 'particle' at time i+1 is computed from its position and velocity at time i:

$$P(x,y,z)_{i+1} = P(x,y,z)_i + \vec{u}(x,y,z)_i * dt \tag{4.4}$$

where $\vec{u}(x,y,z)$ is the interpolated 3D velocity, $P(x,y,z)_i$ and $P(x,y,z)_{i+1}$ are the initial and final particle positions for each internal timestep (*dt*) of 120 seconds. The interpolation scheme used to calculate velocities uses both past and future velocities from 5-day archived flow fields to calculate more accurate velocities at the time that the particle position is updated. The time it takes for water parcels to travel from any grid cell in the model to the mixed layer is also the amount of time it takes for that water parcel to deliver its DIC content to the mixed layer, where it can potentially be removed by biology and gas exchange. Particles were seeded once a month for a year distributed in 17 vertical layers in the top 500m, with a higher particle density toward the surface. Particles were seeded in every latitudinal cell and every fourth meridional cell and were tracked for 2 years with output saved at a 5-day frequency. To generate a more continuous field of particle trajectories, we also consider every 5-day snapshot of the first year as new particle seedings

and track the particles from their new locations for 2 years. Particles that exit the domain or collide with the ocean floor are no longer tracked.

4.4 Results: Part I

4.4.1 Constraining ROMS with WOA18 nitrate and O_2 supersaturation

A large source of nutrients to the surface ocean in the Equatorial Pacific is wind-driven upwelling of water from the Equatorial Undercurrent, which carries waters from both hemispheres that mix in the west and are carried to the east (Goodman et al., 2005; Rodgers et al., 2003; Tsuchiya, 1981; Wang et al., 2019). As subsurface water in the EUC travels east, wind-driven divergence causes water and nutrients to upwell to the surface. The supply of nitrate is especially high in the eastern part of the basin, where surface nitrate supply is additionally bolstered by upwelling along the eastern margin through the dynamically linked Peru upwelling system (Rosales Quintana et al., 2021; Vergara et al., 2016). Much of the available nitrate dissolved in the surface waters to the north, south, and west of the strongest upwelling is controlled by supply and removal of nitrate that upwells along the equator. Surface nitrate concentrations within a few degrees of the equator can be used in combination with off-equatorial nitrate concentrations to constrain the strength of the biological pump required to reproduce the observed nitrate distribution. To this end, we define two averaging regions: an equatorial region (5^oS-5^oN) and an off-equatorial region (14.5^oS-14.5^oN) and conducted a suite of model simulations that span a broad range of NCP (see Methods).

NCP is controlled both by the supply of nutrients to the ecosystem as well as how quickly organisms can grow when nutrients are readily available. Simulations with higher μ_{max} therefore have higher NCP in the eastern equatorial Pacific as phytoplankton are able to grow more rapidly and consume more nitrate before it can be carried away to the north, south, and west. Higher

maximum growth rates lead to the depletion in equatorial surface NO_3 and a corresponding decrease in off-equatorial NO_3 as nitrate upwelled at the equator is prevented from reaching the subtropics (Figure 4.4a,c). Off-equatorial nitrate depletion in high μ_{max} runs therefore still occurs even though NCP is very low away from the equator. At low μ_{max} values, the surface nitrate inventory is elevated both near and far from the equatorial system and at a μ_{max} of zero, the nitrate concentrations in both regions are roughly equal. NO_3 concentrations are quite sensitive to changes in μ_{max} in range of 0-1.5 d^{-1}, where nitrate provides a tight constraint on the range of possible NCP_{MLD} (6-7 mol C m^{-2} yr^{-1} near the equator and 4 +/- 0.2 mol C m^{-2} yr^{-1} away from the equator). The simulation that best reproduces the range of available surface nitrate observations has a μ_{max} of 0.75 d^{-1}.

Biological production of O_2 provides another fingerprint that can potentially be used to constrain NCP as enhanced production offsets the upwelling of undersaturated water and has the potential to produce observable supersaturation that can be used to estimate productivity (Bushinsky & Emerson, 2015; Emerson & Stump, 2010). Unfortunately, although variations in μ_{max} span the entire envelope of observed nitrate, none of the simulations are able to produce $\%O_{2sat}$ values that fall below the observed range of $\%O_{2sat}$ (Figure 4.4b,d). This means that the $\%O_{2sat}$ criterion is not very useful for evaluating how well any given μ_{max} simulation is simulating the real ocean. However, the $\mu_{max=0.75}$ simulation that matches the observed nitrate range also falls within the empirical $\%O_{2sat}$ window. These observations together indicate that the model reproduces available observations of regional tracers for a narrow range of NCP. An advantage to using an ocean model here is that it also allows us to evaluate how well different measures of annually integrated NCP serve as a measurement of carbon export.

4.4.2 Leveraging the carbon mass balance to evaluate carbon export

The basin-scale carbon mass balance in the surface ocean the tropical Pacific is controlled by competing fluxes of upwelled high DIC water along the equator, removal of carbon through the biological export of organic carbon, gas efflux to the atmosphere, and transport of DIC into and out of the model domain. The incoming water that feeds the EUC at the model boundaries already has high DIC content because of the accumulated influence of respiration on those water masses before they enter the model domain. Therefore, the no BEC simulation (see Methods) represents the maximum possible efflux of CO_2 at the ocean surface produced by the combination of physical transport of inorganic carbon from the model boundaries. In this case, the net DIC transport into the model at the ocean boundaries is balanced by the flux to the atmosphere at an area mean rate of -4.2 mol C m^{-2} yr^{-1} (FG_{CO2}^{ABIO}). (Figure 4.5a). This value should be adjusted by 0.26 mol C m^{-2} yr^{-1} to -4.46 mol C m^{-2} yr^{-1} to account for the incoming DOC flux from the model boundaries. This adjustment is necessary because the incoming DOC flux in the abiotic simulation is a net carbon supply that exists in the full ecosystem simulations that isn't degraded while the ecosystem is off.

The surface DIC inventory at steady state includes a CO_2 concentration that is in excess of atmospheric equilibrium in the equatorial Pacific, which produces a net efflux to the atmosphere (Ishii et al., 2014). As μ_{max} increases, the rates of both carbon uptake by phytoplankton and subsequent organic carbon export out of the upper ocean increase. For every mole of carbon removed by the ecosystem that does not return to the surface to be rereleased to the atmosphere, the outgoing air-sea CO_2 flux relative to the no BEC simulation must decrease by the same amount (Figure 4.5a, dashed line). The effective CO_2 flux by the ecosystem (FG_{CO2}^{BIO}) is therefore less negative than FG_{CO2}^{ABIO} and the difference $\Delta FG_{CO2}^{BIO-ABIO}$ is a positive carbon flux that is equal to basin-scale organic carbon sequestration.

The quantity $\Delta FG_{CO2}^{BIO-ABIO}$ represents the amount of carbon prevented from escaping to the atmosphere by ecosystem processes. As described above (see Methods), $\Delta FG_{CO2}^{bio-abio}$ must be fully accounted for by biologically driven DOC and DIC transport (Equation 3), which together equal the total amount of carbon sequestered that is not re-released to the atmosphere within the model domain. The best-fit model simulation based on the nitrate constraint in Figure 4.4a and 4.4b has a μ_{max} of 0.75 d^{-1}, which is the only simulation that falls within the observed surface nitrate window (the green shading in Figure 4.4). By comparing this simulation's FG_{CO2} to FG_{CO2}^{abio}, we find that $\Delta FG_{CO2}^{bio-abio}$ for the model simulation that reproduces the surface nitrate inventory in the tropical Pacific is 3.26 mol C m^{-2} yr^{-1}. The model is in steady state with respect to the net rate of dissolved organic carbon production ($J_{DOC} = \int_{\infty}^{0}(DOC_{sources} - DOC_{sinks})dz$), so T_{DOC} is equal to $-J_{DOC}$, which is -1.7 mol C m^{-2} yr^{-1}. This leaves 1.56 mol C m^{-2} yr^{-1} that must be explained by $\frac{\Delta dDIC}{dt}$, the difference in non-steady state terms between the biotic and abiotic simulations, and ΔT_{DIC}, the carbon sequestered by primarily particulate organic carbon that isn't respired within reach of the atmosphere (see Equation 3).

Generally, $\frac{\Delta dDIC}{dt}$ is expected to be small after sufficiently long model runs as the model approaches steady state. However, the DIC inventory in the deep ocean is not at steady state in the model, even after 30 years. Since J_{DOC} (and therefore T_{DOC} in Equation 3) and FG_{CO2} are at steady state, then as $\frac{\Delta dDIC}{dt}$ approaches zero in very long model runs, ΔT_{DIC} must subsume that change. By extending the model for another 20 years, we confirmed that as $\frac{\Delta dDIC}{dt}$ continues to approach zero, ΔT_{DIC} changes by an equal amount and the other terms remain constant. Based on this, we can consider $\frac{\Delta dDIC}{dt}$ to be zero and find that ΔT_{DIC} must account for the remaining 1.56 mol C m^{-2} yr^{-1} carbon flux.

We can use the results of the above analysis to determine the fraction of NCP that escapes to the atmosphere (Φ in Figure 4.3b) as well as the relative fractions of NCP that is sequestered as DOC leaving the model domain (T_{DOC}) and as DIC exported below the surface ocean, where it exits via subsurface advection (T_{DIC}). Comparing these quantities to NCP_{comp} (4.7 mol C m^{-2} yr^{-1}), it is clear that 33% of the net organic carbon production results in carbon sequestration in the form of ΔT_{DIC} ($\frac{1.56}{4.7}$), 36% leaves the model domain as DOC ($\frac{1.7}{4.7}$), and the remaining 31% must be lost to the atmosphere within the domain. That means that the effective Φ of the tropical Pacific is 0.31. Of the remaining 69% of NCP_{comp}, roughly half leaves the model domain as DOC where it may eventually result in a net efflux of CO_2 to the atmosphere outside of the model domain. Whether the DOC that exits the model domain ultimately results in a loss of carbon to the atmosphere or carbon sequestration is determined by the fraction of T_{DOC} that is respired within reach of the atmosphere and is therefore a function of the relative rates of subduction and degradation of DOC. Unfortunately, we are unable to assess the fraction of T_{DOC} respired out of contact with the atmosphere because it occurs outside of the model domain.

$\Delta FG_{CO2}^{bio-abio}$ can be used as a benchmark for determining how well NCP_{MLD} estimates the true tropical Pacific carbon sequestration in the model, despite the complicated circulation dynamics. NCP_{MLD} agrees well with the basin-scale carbon sequestration across all μ_{max} simulations (to within 13% in the best fit simulation with μ_{max} of 0.75 d^{-1}; Figure 4.5b), consistent with one dimensional models that use NCP_{MLD} as a measure of carbon export (Bushinsky & Emerson, 2015; Palevsky et al., 2016; Palevsky & Doney, 2018). The domain average from (15°S to 15°N) of $\Delta FG_{CO2}^{bio-abio}$ (3.26 mol C m^{-2} yr^{-1}) is similar to other estimates of global zonal average annual NCP in models and satellite products (2.9±2 mol C m^{-2} yr^{-1}; Emerson 2014).

In addition to the differences between NCP_{MLD}, NCP_{comp}, and $\Delta FG_{CO2}^{bio-abio}$, zonal averages highlight equatorial peaks in NCP (Figure 4.6) and even larger differences between NCP_{MLD} and NCP_{comp}. NCP_{comp} reaches zonal mean values of up to 13 mol C m^{-2} yr^{-1}, much of which must not contribute to carbon sequestration. To evaluate regional differences in both NCP and carbon sequestration, we evaluate particle tracking experiments in combination with model rates of respired carbon production in Part 2 below.

4.5 Results: Part II

How much carbon is removed from the atmosphere and how long it remains out of contact with the atmosphere are questions critical to understanding how different regions of the ocean take up and retain carbon from the atmosphere. Whether carbon remains below the surface ocean and is therefore considered "sequestered" is a matter of timescale: as described above, carbon released via respiration above the annual mixed layer depth may be sequestered for months, but it is not likely to be sequestered for more than a year. Analysis of sequestration timescales using a coarse resolution data-constrained global ocean circulation model (DeVries et al., 2012; DeVries & Primeau, 2011) highlight the role of sequestration timescale (τ) in evaluating carbon export and the efficiency of carbon sequestration. Devries et al. (2012) define sequestration efficiency for a given timescale τ as the ratio of organic matter production that remains away from the surface for that length of time. Devries et al. (2012, their Figure 1) show that the fraction of organic matter production that does not reach the surface ocean in one year or less (τ = 1 year) is relatively zonally homogeneous constant across the equatorial Pacific with up to 70-80% of organic matter being sequestered. However, on longer timescales (e.g. τ = 10 years), more organic matter production is sequestered in the eastern equatorial Pacific (40-50%) than in the west (30-40%).The difference

in regional sequestration efficiencies demonstrates the importance of evaluating the eastern and western Pacific separately.

Whether respired carbon in a water parcel in the thermocline remains sequestered on short or long timescales can be captured by that water parcel's ventilation timescale, a measure of the time it takes for that water parcel to outcrop. In a simple 1-D system, water at depths shallower the annual maximum mixed layer will have ventilation timescales less than one year, while the ventilation timescale of the deeper water will be governed by vertical exchange rates that can be very slow. The simple mental model of evaluating carbon sequestration efficiency also works in a more complicated 3-D circulation system, where water with longer ventilation timescales will have a higher likelihood of sequestering carbon for a year or longer.

We use a particle tracking experiment to evaluate how long it takes for water parcels to travel from any grid cell in the model to the mixed layer. The particles were seeded once a month for a year distributed in 17 vertical layers in the top 500m, with a higher particle density toward the surface. Particles were also seeded in every latitudinal cell and every fourth longitudinal cell and they are tracked for 2 years with 10 minute internal particle tracking timesteps and output is saved every 5 days. Every 5 days, we additionally track the particles at their new locations for 2 years, for the purpose of smoothing tracer distributions. Particles that exit the domain or collide with the ocean floor are no longer tracked. By recording how long it takes for particles to cross the mixed layer anywhere along their two-year trajectories, we define our own sequestration timescale (τ). The maximum τ from these particle tracking results is 2 years, since that is the length of our particle tracking experiments. τ only refers to the particles that cross the mixed layer and is therefore less relevant for deep water where only a small fraction of particles reaches the surface. In the model, the depth where 50% of particles seeded at that depth reach the mixed layer shoals

from 200m in the west to 100m in the east along the equator and reaches a minimum of ~50m at 2^{o}N and 2^{o}S (Supplemental Figure 4.3). For simplicity, we will refer to τ horizons based on this sequestration timescale where τ_z^{1yr} refers to the depth horizon that corresponds to a τ of 1 year.

τ_z is a direct result of the physical circulation and therefore reflects the important physical features that drive equatorial circulation. Of these, one of the most defining characteristics of equatorial circulation is the EUC, whose core shoals from about 200m in the western Pacific to about 50-100m in the eastern Pacific and is the source of much of the water that upwells to the surface along the equator in the Pacific. As expected, water right at the equator where upwelling occurs has shorter sequestration timescales than the water to the north and south (Figure 4.7a,c), where upwelling can only occur if that water is reincorporated into the upwelling water via recirculation. It is not surprising that τ_z^{1yr} is as deep as 200m in the western Pacific, since much of the water upwelled to the surface is from the EUC and the core of the EUC is deeper in the west (about 150-200m) than in the east (about 50-100m). Below the overturning cells directly north and south of the equator (at about 100m), τ is longer than 1 year, but still less than 2 years in the eastern Pacific since that water can be reincorporated into the EUC. Particles seeded as deep as 300-400m can still reach the surface across the entire basin along the equator (Figure 4.7d), but these are rare events (Supplemental Figure 4.3d).

The sections of τ_z suggest that respired carbon production below 100m is more likely to remain away from the surface for a year or more in the eastern Pacific in comparison to the western Pacific, consistent with the sequestration efficiencies described in Devries et al. (2012). While the depth of the annual maximum mixed layer is deeper in the west, it is too shallow to explain the still relatively short sequestration timescales below the top 100m in the model, which coincide with the deeper core of the EUC.

Short sequestration timescales (and therefore high Φ in Figure 4.3b) make the local biological carbon pump less effective at sequestering carbon. To evaluate the net impact of the biological carbon pump on DIC in the tropical Pacific, we again use the abiotic simulation in Part I. We define here Δ*DIC* as the difference between the DIC concentration in the biotic and abiotic simulations *(*$\Delta DIC = DIC_{bio} - DIC_{abio}$). Δ*DIC* represents the net impact of photosynthesis and respiration at any location in the water column and its subsequent advection and diffusion by model physics. The distribution of Δ*DIC* in the east, west, and over the full model domain is a result of regional differences in the balance of biological production and consumption of DIC, efflux to the atmosphere, and the physical circulation of DIC and DOC (Figure 4.8).

Physical transport can cause Δ*DIC* to reach vertical maximum or minimum concentrations in areas that are not necessarily sites of rapid organic matter degradation or production, respectively. Below the compensation depth, as long as respiration rates are nonzero, biological processes cause Δ*DIC* to increase (because $DIC_{bio} > DIC_{abio}$). In the surface ocean, net organic matter production decreases DIC_{bio} (and therefore tends to make Δ*DIC* more negative). The influence of the competing signals of respiration and photosynthesis is circulated by physics and the resulting ΔDIC distribution is a tracer of the net impact of biology on DIC and its subsequent transport. The vertical concentration gradient in Δ*DIC* is maintained in general by the biological pump and CO_2 gas exchange. Areas where Δ*DIC* is the most positive are areas where the respiratory signal associated with the biological carbon pump has the largest impact on the concentration of DIC.

To begin to connect τ to the 3-dimensional distribution of respired carbon and evaluate how the physical circulation impacts the distribution of Δ*DIC*, we show Δ*DIC* along the same select transects (Figure 4.8). The maximum positive values of Δ*DIC* are in the eastern Pacific below the

EUC and near the eastern boundary upwelling systems along the coast (Figure 4.8c,d), especially below 250m. ΔDIC is highest in the deep, where the net removal of respired carbon is slow due to sluggish circulation. ΔDIC reaches its most negative values near the surface and in the western reaches of the EUC (150-200m, Figure 4.8a), where advection and upwelling together reduce ΔDIC in the EUC. The larger ΔDIC in the eastern Pacific and below the equator suggest relatively more storage of respired carbon in the eastern equatorial Pacific compared to both the south Pacific (Figure 4.8b) and the western equatorial Pacific. The east-west difference observed here is consistent with what one might expect from satellite-derived maps of annually integrated NCP that depict rates in the eastern equatorial Pacific on the order of 3-4 mol C m^{-2} yr^{-1}, which is roughly twice as large as the rates in the west, which are in the range of 1.5-2 mol C m^{-2} yr^{-1} (Westberry et al., 2012).

While sections of ΔDIC can be used to infer many connections between physics and the biological impact on DIC, we define a new quantity, J_{DIC*}, to quantitatively assess the fraction of respired carbon that is sequestered on different timescales. Below the compensation depth, where J_{DIC} is positive, we define the rate J_{DIC*}, which is a measure of the amount of net heterotrophy in the water column. J_{DIC*} is zero above the compensation depth where J_{DIC} is negative, so the full water column integral of J_{DIC*} is equal to J_{DIC} integrated from the ocean floor to the compensation depth ($\int_{\infty}^{0} J_{DIC*} dz = \int_{\infty}^{z_{comp}} J_{DIC} dz$). The vertical distribution of J_{DIC*} at any location contains information about how likely that respired carbon is to reach the surface on a given timescale. J_{DIC*} is at its highest where the decline in particulate organic carbon flux with depth is at its steepest and where the rate of DOC degradation is at its highest, but organic matter degradation continues throughout the water column (Supplemental Figure 4.4). Sections of the cumulative column integral of J_{DIC*} highlight the relationship between depth and the net biological production of

respired carbon. In Figure 4.9, the plotted value shows J_{DIC*} integrated from the ocean floor to that depth. By comparing the values at 100m in Figure 4.9, it is clear that up to 10-12 mol C m^{-2} yr^{-1} is respired below 100m in the eastern Pacific, (Figure 4.9c,d), whereas only about 1-2 mol C m^{-2} yr^{-1} is respired below 100m in the west (Figure 4.9a) and south (Figure 4.9b). In general, J_{DIC*} that occurs in water where τ is very long produces DIC* that is more likely to remain below the surface ocean on long timescales. The high rates of column integrated J_{DIC*} that occur directly to the north and south of the equator and below the τ_z^{1yr} horizon (e.g. at 100°W in Figure 4.9c), therefore suggest that carbon export near the equator may be very efficient. In contrast, a large fraction of DIC* production in the west (Figure 4.9a) occurs above the τ_z^{1yr} horizon and is not likely to produce DIC* that is sequestered on long timescales.

The fraction of $\int_z^{z=0} J_{DIC*} dz$ that occurs below a given τ_z can be calculated explicitly in the model and is a measure of the fraction of respired carbon that remains out of contact with the mixed layer for at least that long. $\int_\infty^{z=0} J_{DIC*} dz$ is much higher in the eastern equatorial Pacific, reaching values ranging from ~8-15 mol C m^{-2} yr^{-1} (Figure 4.10a). In contrast, $\int_\infty^{z=0} J_{DIC*} dz$ west of 140°W reaches maximum values of only ~5 mol C m^{-2} yr^{-1}. Of those totals, 4-10 mol C m^{-2} yr^{-1} and 1-2 mol C m^{-2} yr^{-1} of $\int_\infty^z J_{DIC*} dz$ occur below τ_z^{1yr} (Figure4.10b,c; see Supplemental Figure 4.5 for τ_z^{2yr}).

The western equatorial Pacific clearly has a significantly higher relative fraction of respired carbon production that occurs in water that outcrops on short timescales, which is consistent with the transect analysis above. The source of this respired carbon can be in the form of particulate organic carbon (POC) and/or DOC. The distribution of the source of DIC therefore depends on the impact of the circulation on DOC and the relative rates of production of DOC and POC. The

fraction of NCP that is routed into DOC production can be calculated directly in the model at any location and we show the result in Figure 4.10a. About 40-50% of NCP goes into DOC production along the equator in the east and the DOC produced is advected westward and poleward in the surface ocean away from the eastern equatorial region. To the north and south of the equator, a larger fraction of NCP is in the form of DOC. In those regions (i.e. 5ºN and 5ºS), the poleward advection of DOC that is advected locally decreases NCP as it contributes an additional source of respiration that is not offset locally by organic matter production. The result of the net transport of DOC away from the eastern equatorial region is that a higher fractional source of respired carbon is a result of DOC degradation (Figure 4.11b) in the west compared to the east. Almost none of the respired carbon production highlighted in the transect analyses above in the eastern equatorial Pacific are a result of DOC degradation and is therefore driven by respiration of POC.

4.6 Discussion

The strength of the biological carbon pump and the fraction of NCP that is sequestered in the tropical Pacific is highly variable, with the highest NCP and the largest $\int_{\infty}^{0} J_{DIC^*} dz$ found in the eastern equatorial Pacific. Using the particle tracking results, we can compute the amount of respired carbon production (J_{DIC^*}) that occurs below the depth horizons corresponding to timescales ranging from 0-2 years and we choose three averaging regions to highlight regional differences (Figure 4.12). By integrating respired carbon production below τ_z^{1yr}, we find that the basin-scale carbon export (15ºS-15ºN) is on the order of 2 mol C m^{-2} yr^{-1} (a value of 1 on the x-axis in Figure 4.12). Given the air-sea CO_2 flux for the model domain (-1.2 mol C m^{-2} yr^{-1} from Figure 4.5a in the best case model simulation), a carbon export flux of 2 mol C m^{-2} yr^{-1} below τ_z^{1yr}, and the net supply of 4.2 mol C m^{-2} yr^{-1} to the upper ocean (from T_{DIC} in abiotic simulation), then we can compute the fraction of T_{DIC} that is routed into each pool. 28% of the incoming DIC supply

to the tropical Pacific is lost to the atmosphere via gas exchange, 48% of that incoming DIC is respired in the deep as a result of (primarily particulate) organic carbon respired below τ_z^{1yr}, and the remaining 24% is lost horizontally as DOC. However, since the carbon mass balance in section 4.4.2 predicts basin-scale carbon sequestration of 1.56 mol C m^{-2} yr^{-1}, then 0.44 mol C m^{-2} yr^{-1} of the carbon respired below τ_z^{1yr} must return to the surface ocean within the model domain. This suggests that the timescale of carbon sequestration that is climatically relevant for the tropical Pacific is longer than 1 year. In fact, it must also be longer than 2 years because the carbon export flux respired below $\tau_z^{2yr}$is 1.7 mol C m^{-2} yr^{-1} (Figure 4.12), which is still 0.14 mol C m^{-2} yr^{-1} too high.

There are also distinct regional differences in the amount of carbon respired below the 1-year and 2-year timescale horizons. We find that in the western Pacific (e.g. 180°W-140°W; Figure 4.12, red line) , the fraction of J_{DIC*} that occurs below ($\frac{\int_{\infty}^{\tau_z^{1yr}} J_{DIC*}\,dz}{\int_{\infty}^{0} J_{DIC*}\,dz}$ is roughly equal to the fraction of J_{DIC*} that occurs below τ_z^{2yr} (a value of 2 on the x-axis in Figure 4.12) is equal to 0.6 mol C m^{-2} yr^{-1} or ~23% of the total net respiration below the compensation depth. This value is quite small relative to previous geochemical estimates of western equatorial Pacific carbon export on the order of 1.5 ± 0.2 mol C m^{-2} yr^{-1} derived from triple isotope measurements of gas fluxes (Stanley et al., 2010). This difference is due to the difference between using explicit particle transit times and the mixed layer depth (as in Stanley et al., 2010) because water well below the mixed layer in the western equatorial Pacific is brought to the surface on short timescales (Figure 4.7a). The annual maximum mixed layer in the western equatorial Pacific coincides with a sequestration timescale of about 0.25 years (e.g. the red line and black contours in Figure 4.7a). The carbon export below

the 0.25 year timescale horizon (the x-axis in Figure 4.12), is about 1.5 mol C m^{-2} yr^{-1} in the west (the y-axis in Figure 4.12), which is quite similar to the mixed layer estimate in Stanley et al (2010).

The eastern Pacific (e.g. 120°E-90°W, Figure 4.12, blue line) has both much higher rates of respired carbon production ($\int_{\infty}^{0} J_{DIC^*} dz$ = 5.4 mol C m^{-2} yr^{-1}; the y axis in Figure 4.12 at τ=0) and a smaller fraction that occurs above short timescale horizons ($\frac{\int_{\infty}^{\tau} J_{DIC^*} dz}{\int_{\infty}^{0} J_{DIC^*} dz}$, Figure 4.10d). Our values of 4.2 mol C m^{-2} yr^{-1} (or 77% of $\int_{\infty}^{0} J_{DIC^*} dz$) that is below the τ_z^{1yr} horizon in the eastern equatorial Pacific is within the range of total organic carbon export estimates compiled in the US-JGOFS process study at 140°W in Quay et al., (1997) that were 5 and 20 mmol C m^{-2} d^{-1} in spring and fall (or 1.7 and 6.7 mol C m^{-2} yr^{-1}).

Similar to DeVries et al. (2012), we find that respired carbon is significantly more likely to remain away from the surface for longer timescales in the eastern equatorial Pacific and the 77% reported here agrees well with their 1 year sequestration efficiency. The regional difference we find is distinctly different from the sequestration efficiency maps in Devries et al. (2012), but the regional difference in carbon export fluxes on a 1 year timescale (0.6 in the west compared to 4.2 in the east) is very similar to that predicted by satellite products as in Westberry et al. (2008). Empirical estimates of NCP in the eastern equatorial Pacific besides satellite estimates are scarce and most don't extend beyond 140°W. However, our value of 4.2 mol C m^{-2} yr^{-1} falls squarely in the range of empirical estimates summarized in Emerson (2014). Our results suggest that satellite-derived NCP estimates that show pronounced equatorial carbon export fluxes reflect real regional differences in carbon sequestration and that the eastern equatorial Pacific plays an outsized role in the carbon mass balance.

4.7 Figures

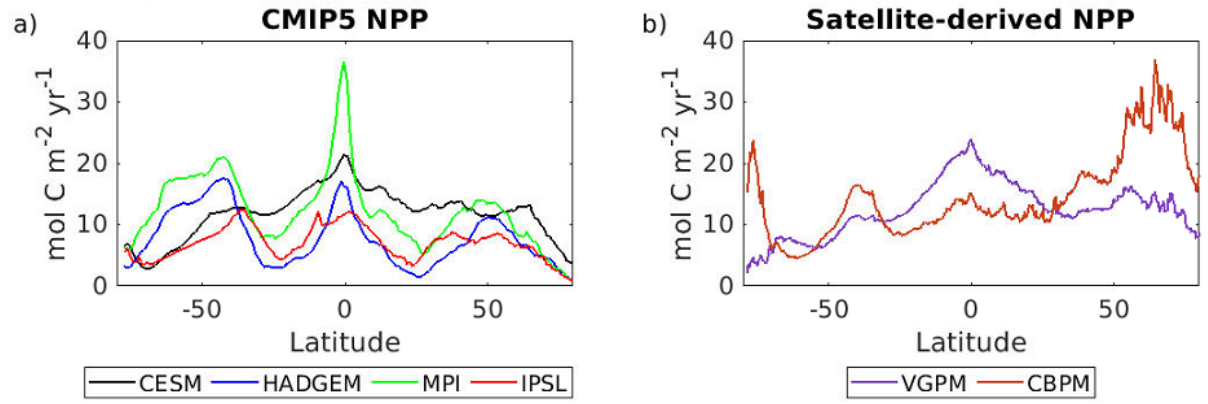

Figure 4.1. Zonal mean net primary productivity in CMIP5 ocean models and two satellite algorithms. (a) The global zonal average of integrated net primary productivity of all phytoplankton size classes in four CMIP5 ocean models from 1955-2000 (MPI-ESM-LR, HADGEM2-ESM-LR, IPSL-CM5A-LR, and CESM1-BGC; Taylor et al., 2012). (b) The global zonal average of two satellite-derived net primary productivity products (VGPM; Behrenfeld & Falkowski, 1997, CBPM; Westberry et al., 2008).

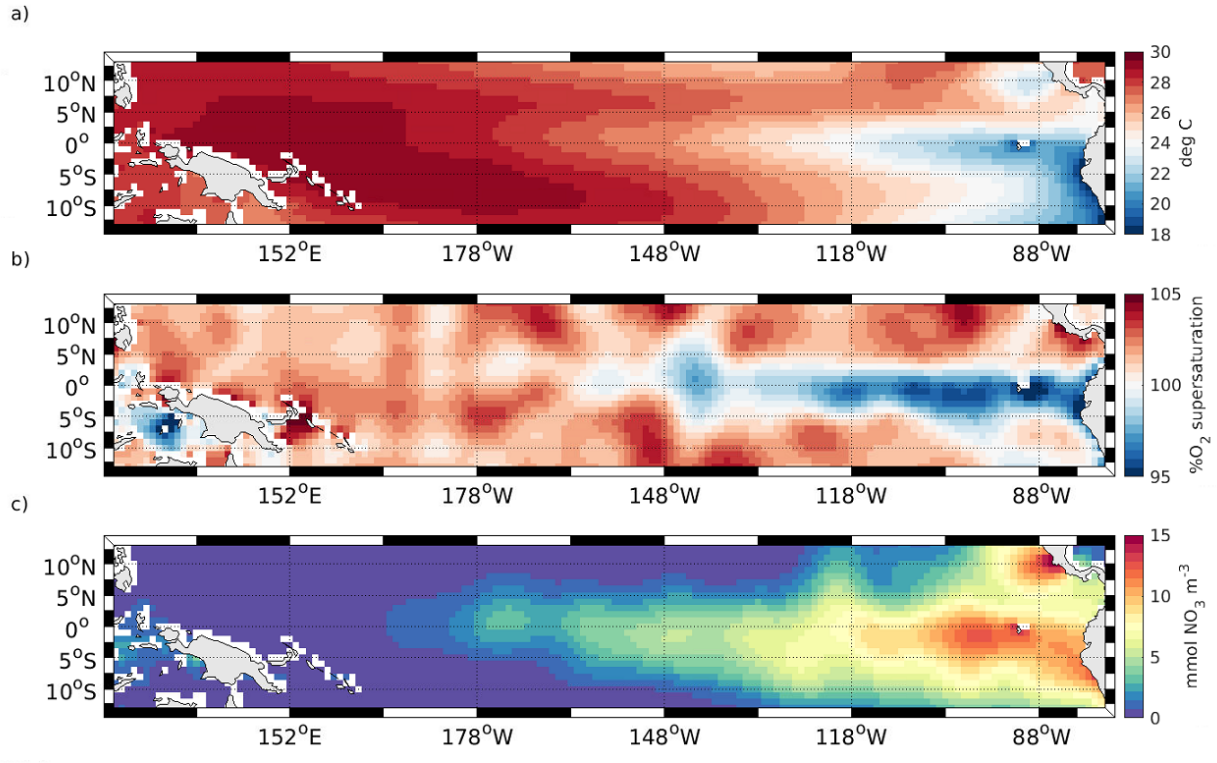

Figure 4.2. Annual mean surface characteristics in the equatorial Pacific based on World Ocean Atlas 2018 data. a) The top 50m annual average temperature. b) Oxygen supersaturation calculated as $(O_2\text{-}O_{2sat})/O_{2sat}$ where O_{2sat} is the oxygen concentration at saturation and O_2 is the in-situ oxygen concentration. c) The top 50m annual average NO_3.

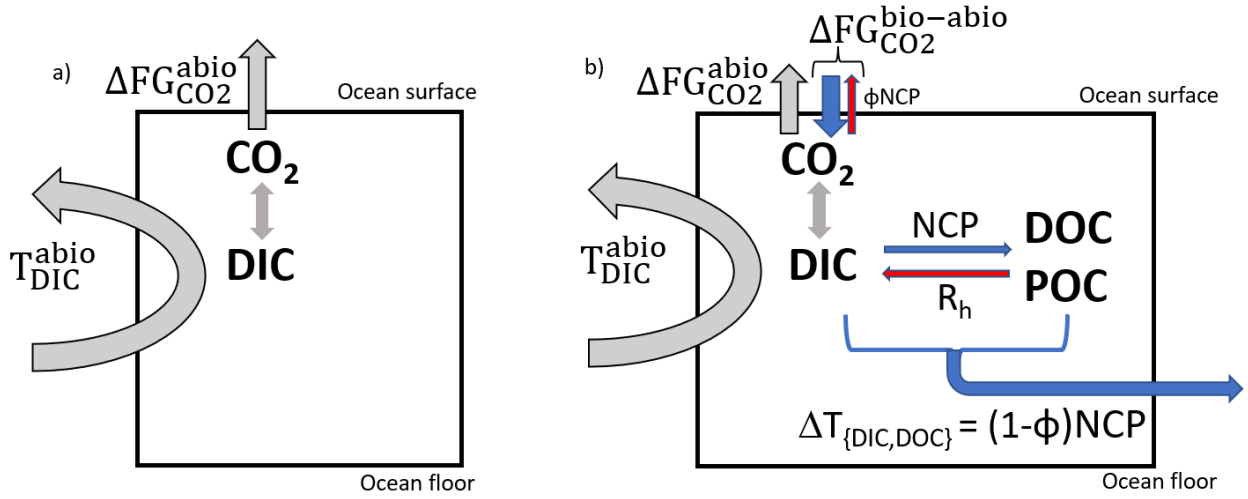

Figure 4.3. Conceptual model for the tropical Pacific carbon cycle for the full model domain (15°S-15°N and from the ocean surface to the ocean floor). a) The abiotic carbon mass balance. T_{DIC}^{abio} refers to the net advective supply of DIC to the model domain, where subsurface and surface transport are net sources and sinks of DIC, respectively. The net supply of DIC to the model domain is balanced by the loss of CO_2 by gas exchange at the surface (FG_{CO2}^{abio}). b) The carbon mass balance with the full model ecosystem. The biological uptake of DIC produces organic matter (NCP), which reduces the surface DIC concentration and reduces the outgoing gas flux of CO_2. A fraction of the respiration of DOC and POC by heterotrophs (R_h) can occur in water that is brought in contact with the atmosphere within the model domain, resulting in a fraction of NCP that escapes back to the atmosphere as CO_2 and does not contribute to carbon export (ϕ). The respiration of DOC and POC by heterotrophs (R_h) that occurs in water that remains out of contact with the atmosphere causes a change in the net transport of carbon due to biological processes (ΔT_{bio}) that is equal to $(1-\phi)$NCP.

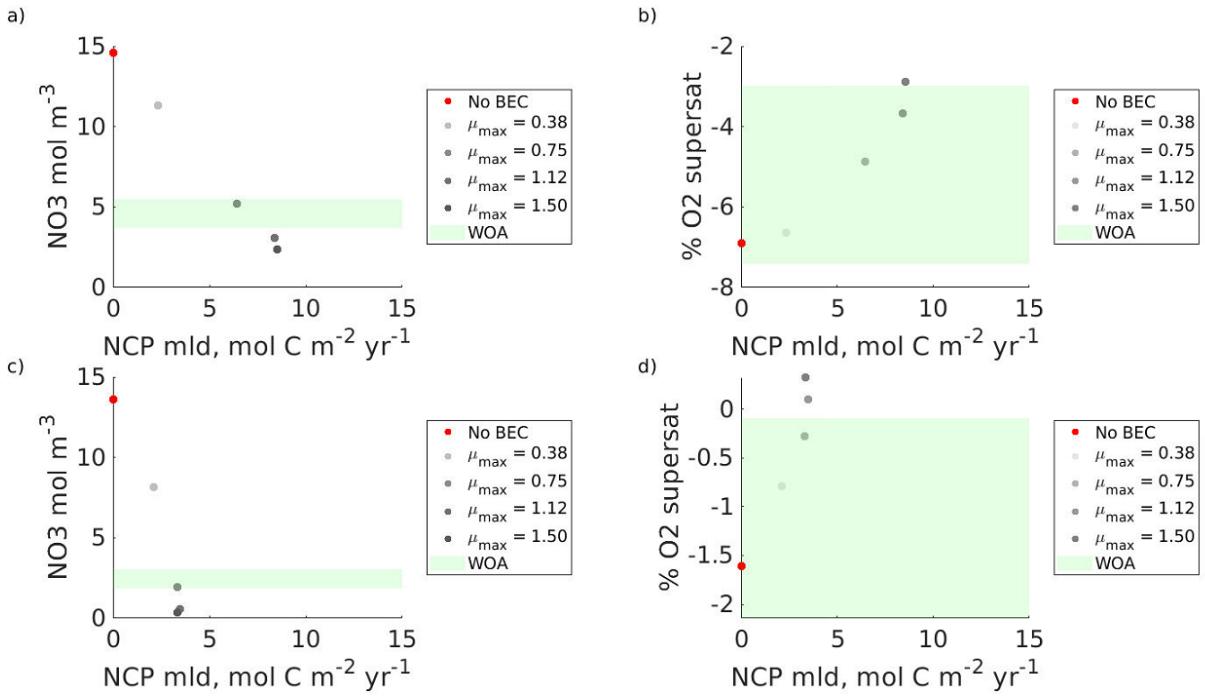

Figure 4.4. Constraining NCP in ROMS with observed NO_3 and $\%O_2$ supersaturation in the World Ocean Atlas 2018 (WOA18). Empirical constraints in the eastern Pacific in an equatorial region (3a,b; 140°E-80°W, 4°S-4°N) and off-equatorial region (3c,d; 140°E-80°W, 15°S-4°S + 4°N-15°N). The gray dots in each figure correspond to a run with a different maximum growth rate (μ_{max}), which ranges from 0.38 to 3.00 d^{-1} in these runs with darker grays corresponding to higher μ_{max}. The green shading in each figure is constructed using the seasonal minimum and maximum nitrate concentrations (a,c) or $\%O_{2sat}$ (b,d) in each region over the top 50m of the ocean in WOA18. The NCP used in these plots is NCP integrated to the annual maximum mixed layer, which is a standard measure of NCP in the literature.

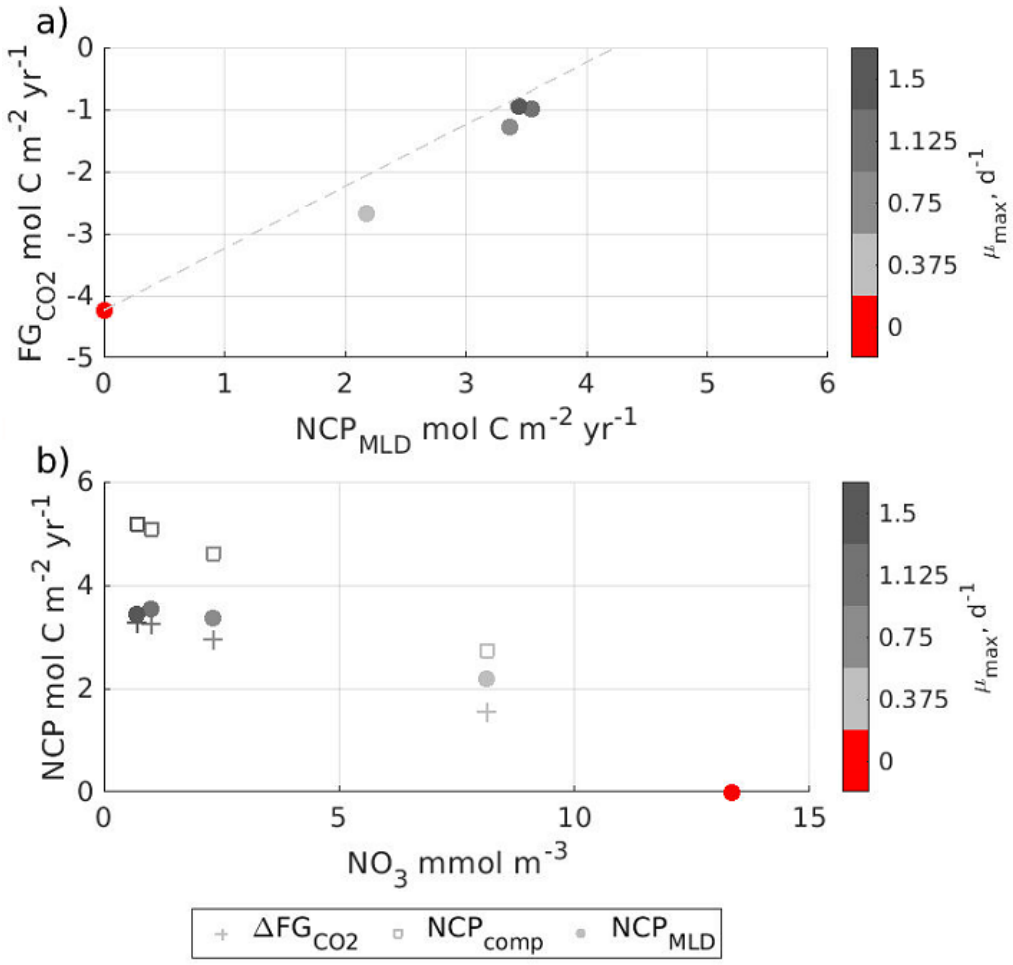

Figure 4.5. The relationship between air-sea CO_2 flux and NCP (mol C m^{-2} yr^{-1}) over the whole model domain (140°E-80°W, 15°S-15°N). The range in NCP on the x axis is forced by changing the maximum rate of phytoplankton growth in the model (μ_{max}), from 0.38 d-1 to 1.5 d-1, as indicated by the color bar. The red shading corresponds to the abiotic simulation where all ecosystem processes are turned off and corresponds to a μ_{max} of 0. While a μ_{max} of 0.75 d^{-1} (the second lightest gray shading) reproduces observed surface nitrate (see text and Figure 4.4), the full range can be used to demonstrate the connection between NCP and outgoing air-sea CO_2 flux and to evaluate the utility of different NCP tracers for evaluating the magnitude of carbon sequestration. Carbon sequestration is equal to $(1-\phi)$NCP in Figure 4.3, which can be estimated by $\Delta FG_{CO2}^{bio-abio}$ and is depicted as the crosses in b.

(a). Values on the y axis indicate air-sea CO2 flux, where negative values indicate a flux from the ocean to the atmosphere. The red dot is a ROMS model run where ecosystem activity is turned off (No BEC, NCP = 0). The dashed line is the hypothetical relationship between NCP_{MLD} and the difference in air sea flux with μ_{max} equal to zero and μ_{max} > zero ($\Delta FG_{CO2}^{bio-abio}$) if a one mole increase in NCP_{MLD} resulted in a $\Delta FG_{CO2}^{bio-abio}$ of exactly one mole. The gray dots are the ROMS model results.

(b) Values on the x axis correspond to the nitrate concentrations in the top 50m across the range of μ_{max} simulations. Each set of symbols corresponds to a different estimate of carbon export, where open squares and circles are derived from net biological O_2 production integrated to the compensation depth and maximum annual mixed layer respectively. The crosses are the areal mean biological induced change in CO_2 flux ($\Delta FG_{CO2}^{bio-abio}$), which is calculated as $\Delta FG_{CO2}^{bio-abio}$. For the best fit model simulation (μ_{max} = 0.75 d^{-1}), NCP_{MLD} and $\Delta FG_{CO2}^{bio-abio}$ differ by roughly 14% when integrated over the full model domain. This indicates that 14% of the carbon that is predicted to contribute to carbon export when integrating to the annual maximum mixed layer is in fact released back to the atmosphere within the model domain.

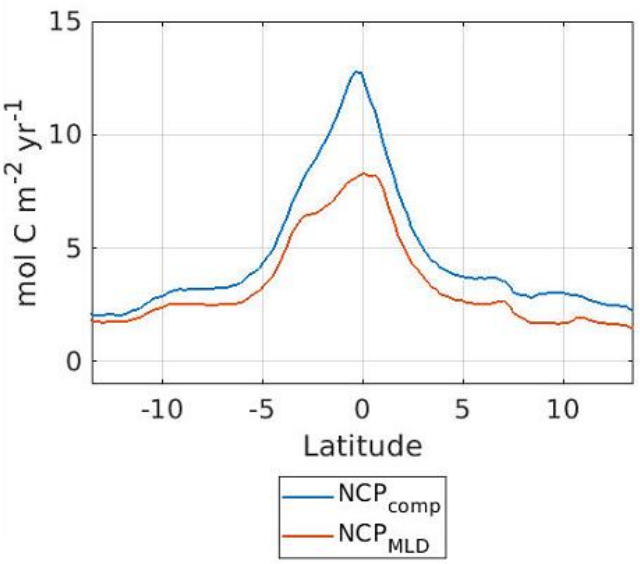

Figure 4.6. Zonally averages NCP_{MLD} and NCP_{comp}. NCP_{comp} and NCP_{MLD} are calculated as annual rates $\int_0^{z_{comp}} r_{C:O} J_{O2} dz$ and $\int_0^{z_{MLD}} r_{C:O} J_{O2}\, dz$ where $r_{C:O}$ is the carbon to oxygen Redfield ratio in ROMS-BEC (1.2821) and J_{O2} is the net ecosystem production of O_2.

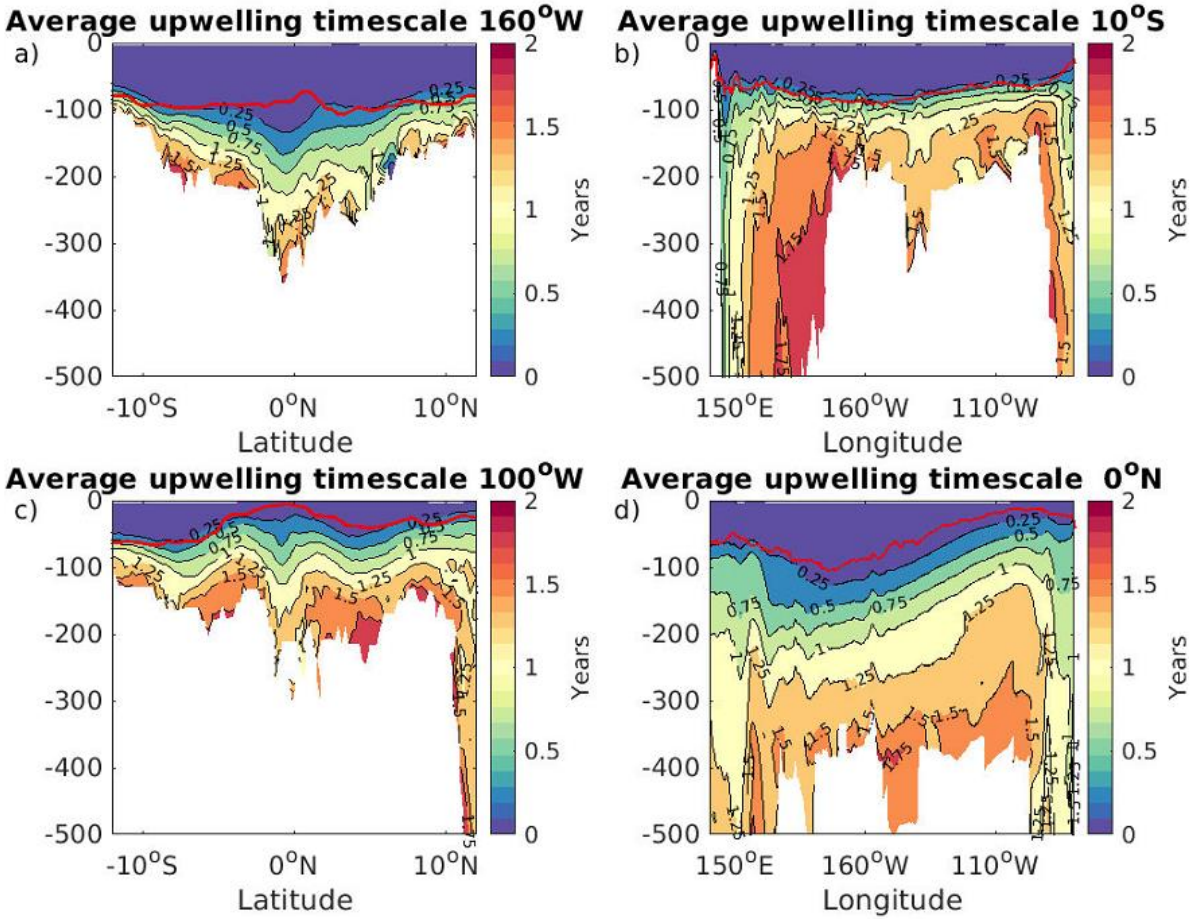

Figure 4.7. Average time that it takes for particles to reach the mixed layer. (a,c) 1-degree zonal averages at 160°W and 100°W and (b,d) 1-degree meridional transects at 10°S and 0°N. The red line in each plot is the annual maximum mixed layer depth. Particles are seeded once a month for one year with one particle per grid cell in the top 500m and tracked for 3 years. 5-day snapshots are used as repeat seedings for a total of over 40,000,000 particles. Particles that stay below the mixed layer for 2 or more years are excluded from these upwelling time averages.

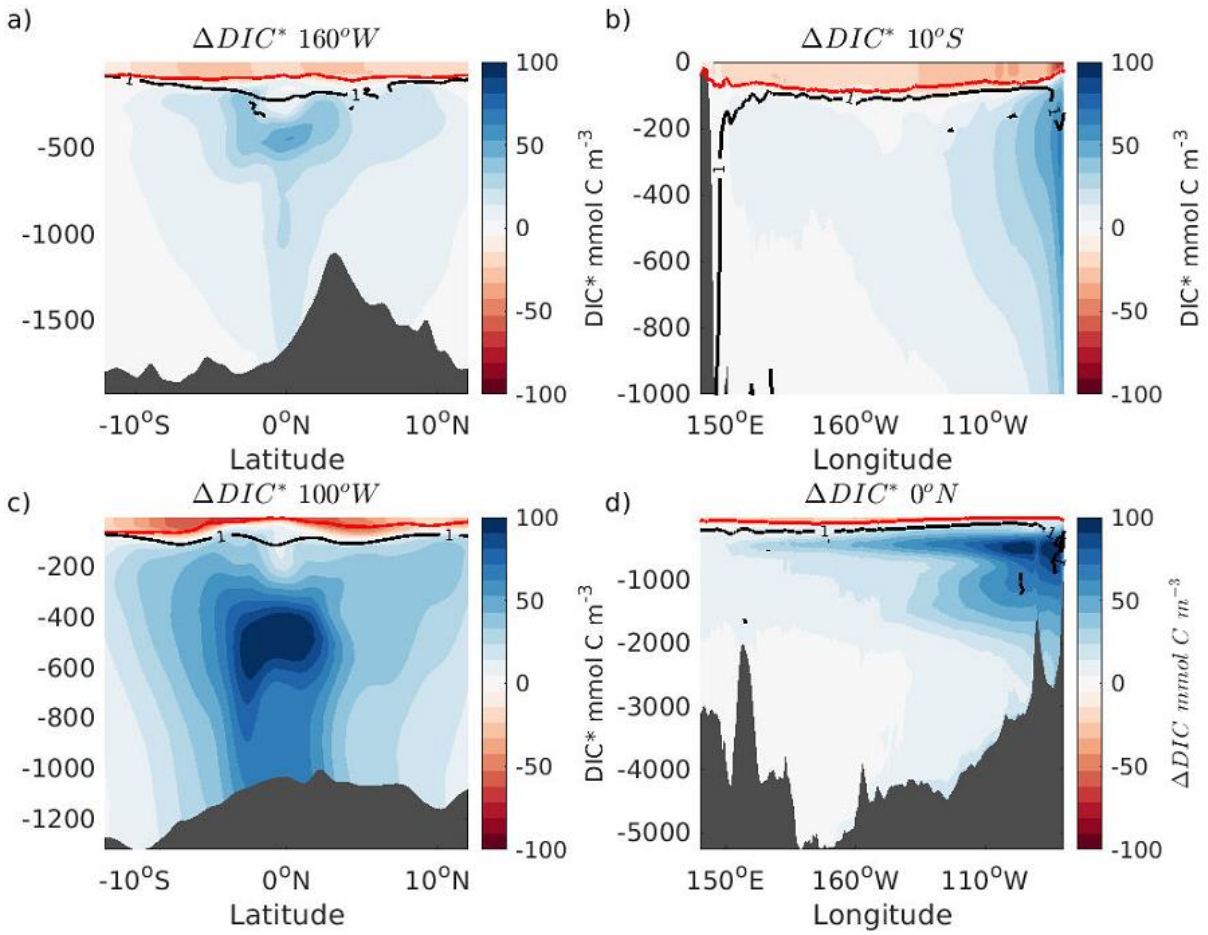

Figure 4.8. Annual mean Δ*DIC* (*DIC*$_{bio}$ – *DIC*$_{abio}$) after 30 years. (a,c) 1-degree zonal averages of Δ*DIC* at 160°W and 100°W and (b,d) 1-degree meridional transects at 10°S and 0°N. The red line in each plot is the annual maximum mixed layer depth and the black lines are the 1-year timescale horizon from Figure 4.7.

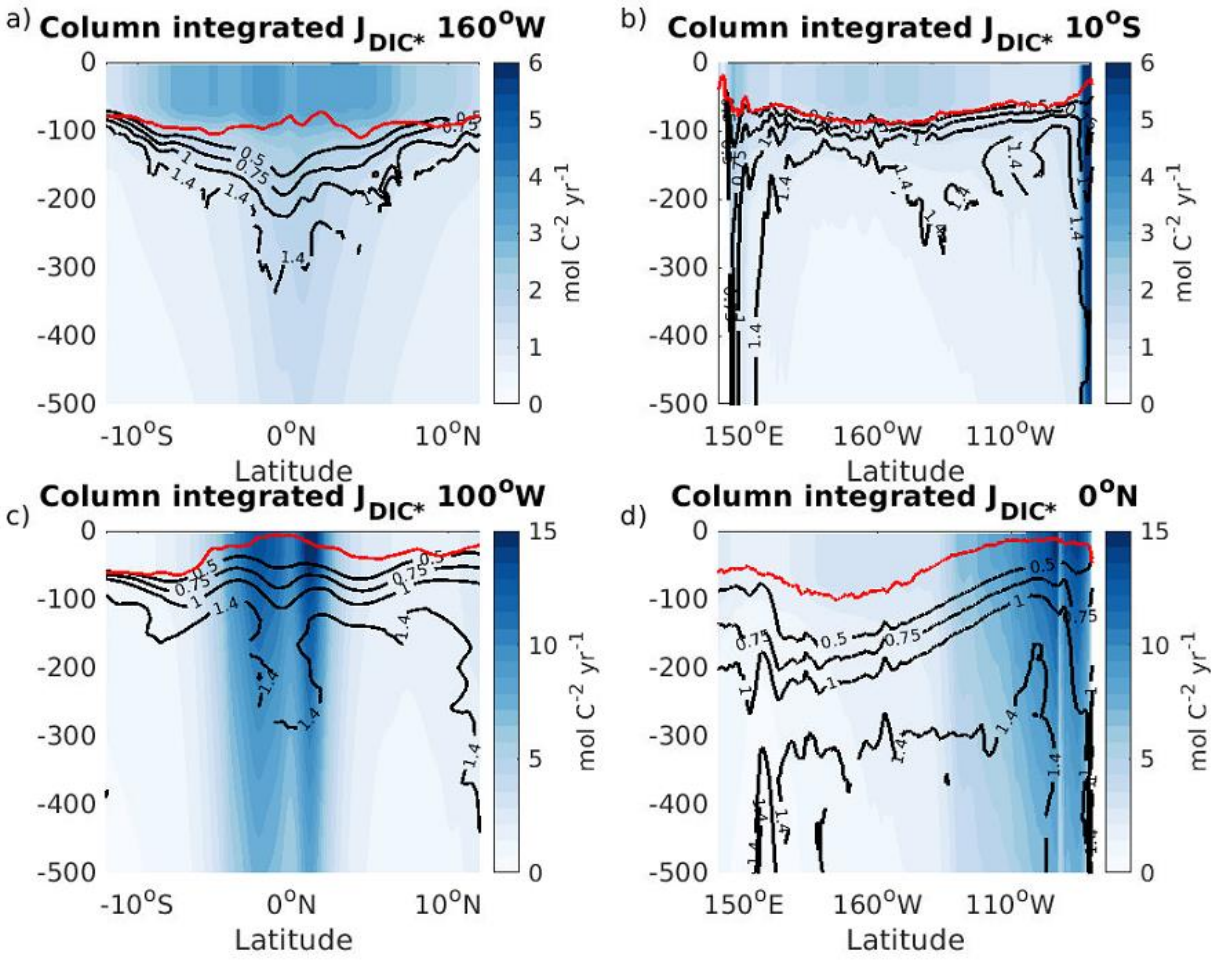

Figure 4.9. The cumulative column integral of J_{DIC^*} ($\int_{\infty}^{z} J_{DIC^*}\, dz$) evaluated at depths from 0-500m. (a,c) 1-degree zonal averages of $\int_{\infty}^{500m} J_{DIC^*}\, dz$ to $\int_{\infty}^{0} J_{DIC^*}\, dz$ at 160°W and 100°W and (b,d) 1-degree meridional transects at 10°S and 0°N. The red line in each plot is the annual maximum mixed layer depth and the black lines correspond to the τ depth horizons for different sequestration timescales (Figure 4.7). The shading at a given depth corresponds to the integral of J_{DIC^*} from the ocean floor to that depth.

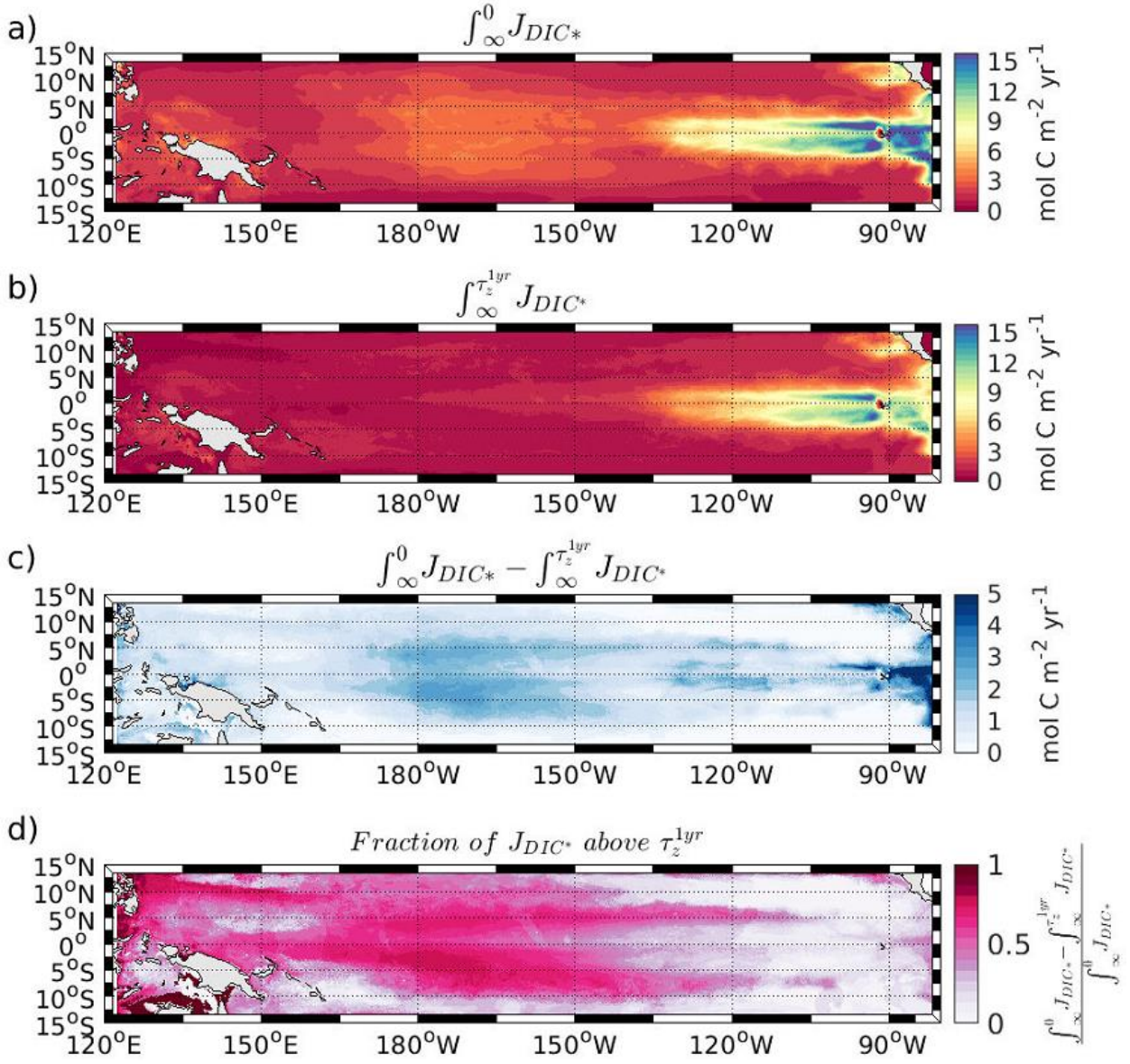

Figure 4.10. The relative rate and fraction of respired carbon production below the 1-year sequestration timescale horizon. (a) $\int_{\infty}^{0} J_{DIC*} dz$, where J_{DIC*} is defined as J_{DIC} where J_{DIC}<0. (b) J_{DIC*} integrated below the 1-year sequestration timescale horizon (τ_z^{1yr}). (c) The cumulative column integral of J_{DIC*} above τ_z^{1yr} ($\int_{\infty}^{0} J_{DIC*} dz$ - $\int_{\infty}^{\tau_z^{1yr}} J_{DIC*} dz$. (d) The fraction of respired carbon production that occurs above τ_z^{1yr}.

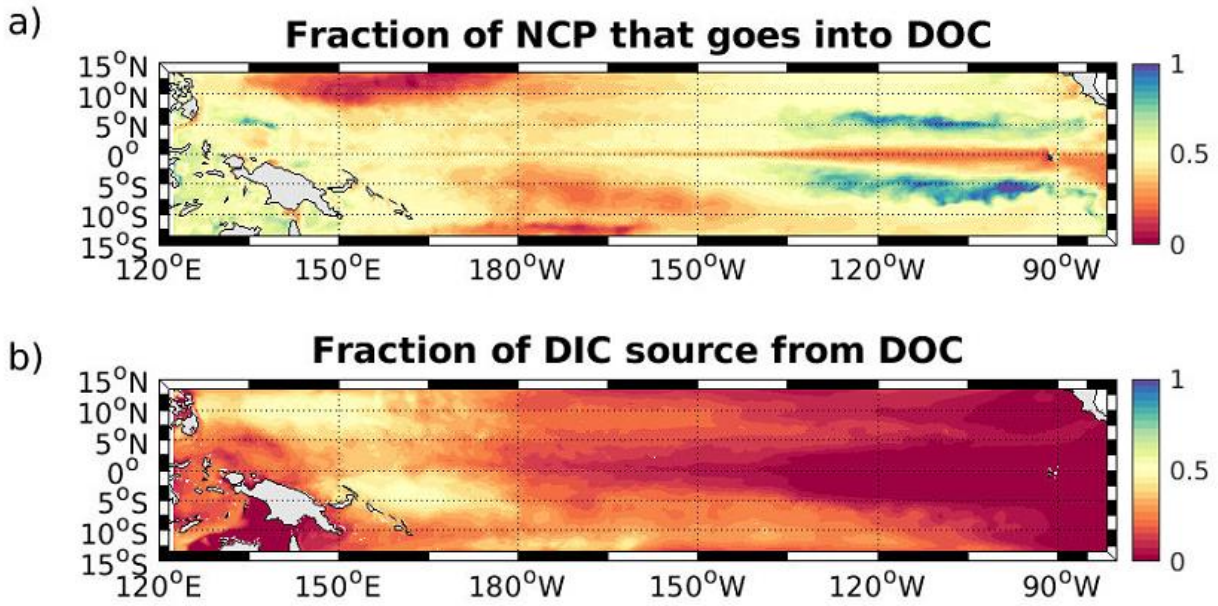

Figure 4.11. The relative fractions of production and consumption of DIC and DOC. (a) Relative magnitude of net DOC production compared to net organic matter production (NCP) shown as $\frac{\int_{\infty}^{0} J_{DOC}>0}{\int_{z_{comp}}^{0} J_{DIC}}$. (b) The fraction of net respired carbon production below the compensation depth attributed to net DOC degradation ($\frac{\int_{\infty}^{0} J_{DOC}<0}{\int_{\infty}^{z_{comp}} J_{DIC}}$).

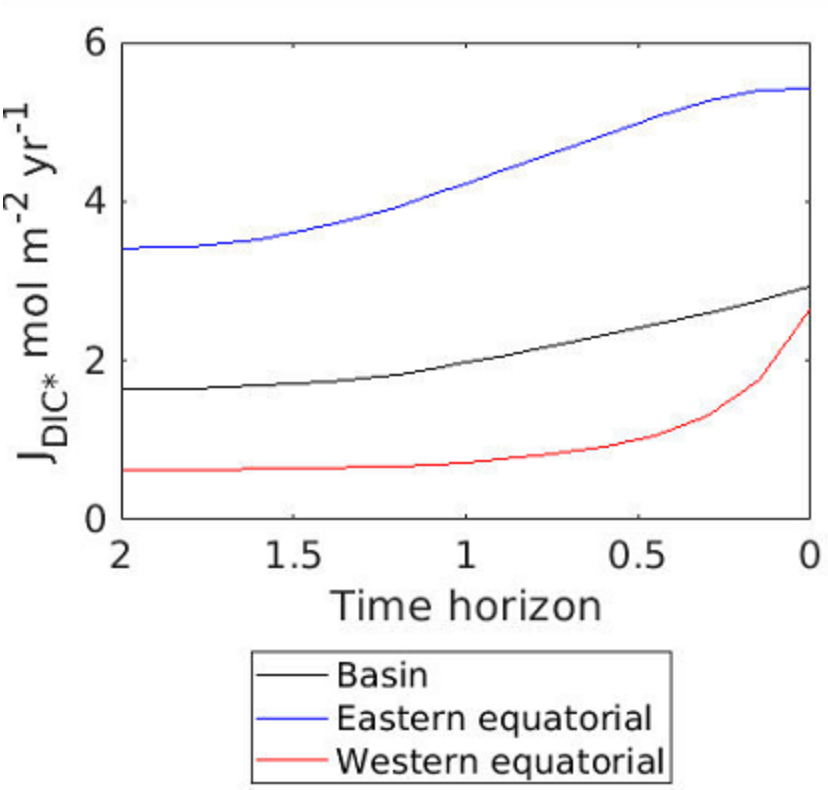

Figure 4.12. The amount of respired carbon production that remains out of contact with the atmosphere on timescales of 0 to 2 years for three averaging regions: the full model domain (black line), an eastern box (120°E-90°W, blue line), and a western box (180°W-140°W, red line). The y axis is $\int_{\infty}^{z} J_{DIC^*}$, where z is defined as the depth horizon that corresponds to the specified sequestration timescale horizon defined using particle tracking results, as described in the text (e.g. $\int_{\infty}^{2yr} J_{DIC^*}$ is the column integrated J_{DIC^*} below the 2 year sequestration timescale horizon τ_z^{2yr}). The range in sequestration timescale horizons for this analysis is shown on the x axis.

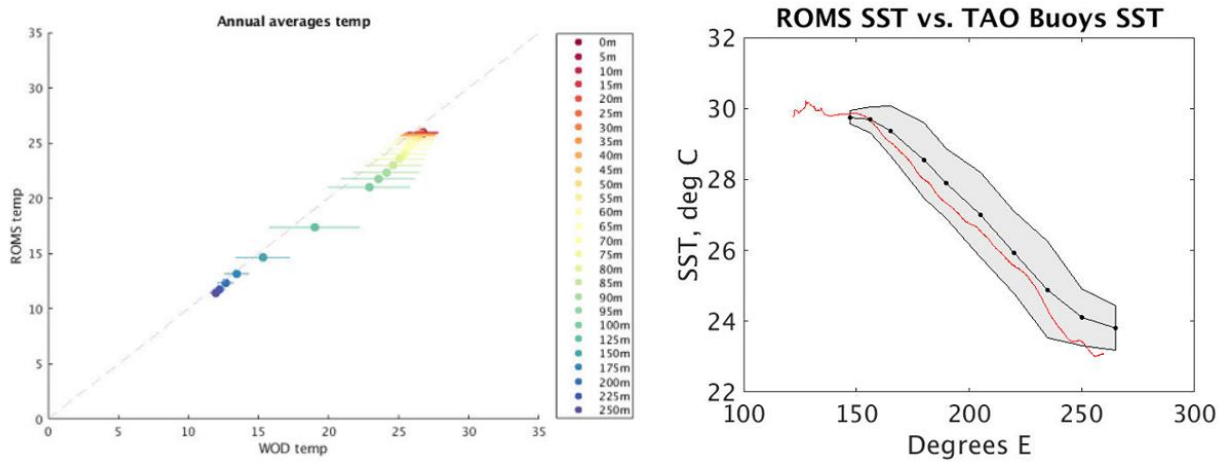

Supplemental Figure 4.1. Temperature in ROMS compared to WOA and TAO buoys. a) Temperature at 140^{o}W within 2.5^{o} north and south of the equator from the surface to 250m. b) Sea-surface temperature on ROMS sampled at the locations of the TAO buoys and then meridionally averaged. Gray area = +/- 1 standard deviation for annual averages from TAO buoys. Years with missing data in any month are not included in the means or standard deviation estimates.

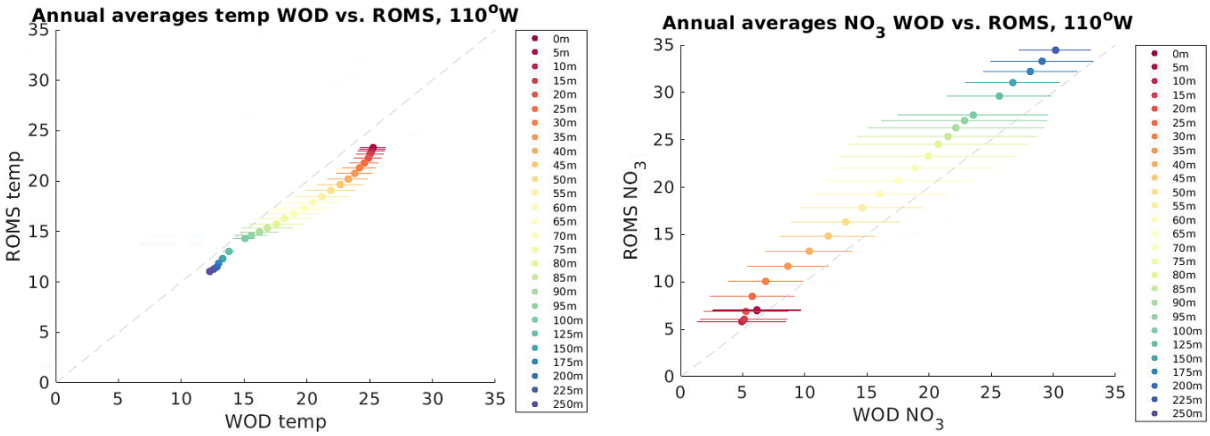

Supplemental Figure 4.2. ROMS and WOA NO_3 and temperature comparison at 110°W within 5° north and south of the equator from the surface to 250m. Each point corresponds to annually averaged $[O_2]$ or $[NO_3]$ at a specific depth with error bars depicting ±1σ. The model output is from years 55 of the "best-case" simulation arrived at through extensive sensitivity tests to the half-saturation constant for iron uptake by phytoplankton, the attenuation profile of particulate organic matter, and the respiration timescale of DOM. The observational data is from the World Ocean Database 2013 (WOD13). The model has somewhat enriched near-surface nitrate and somewhat enriched surface and deep $[O_2]$, but overall model-observation agreement is quite good.

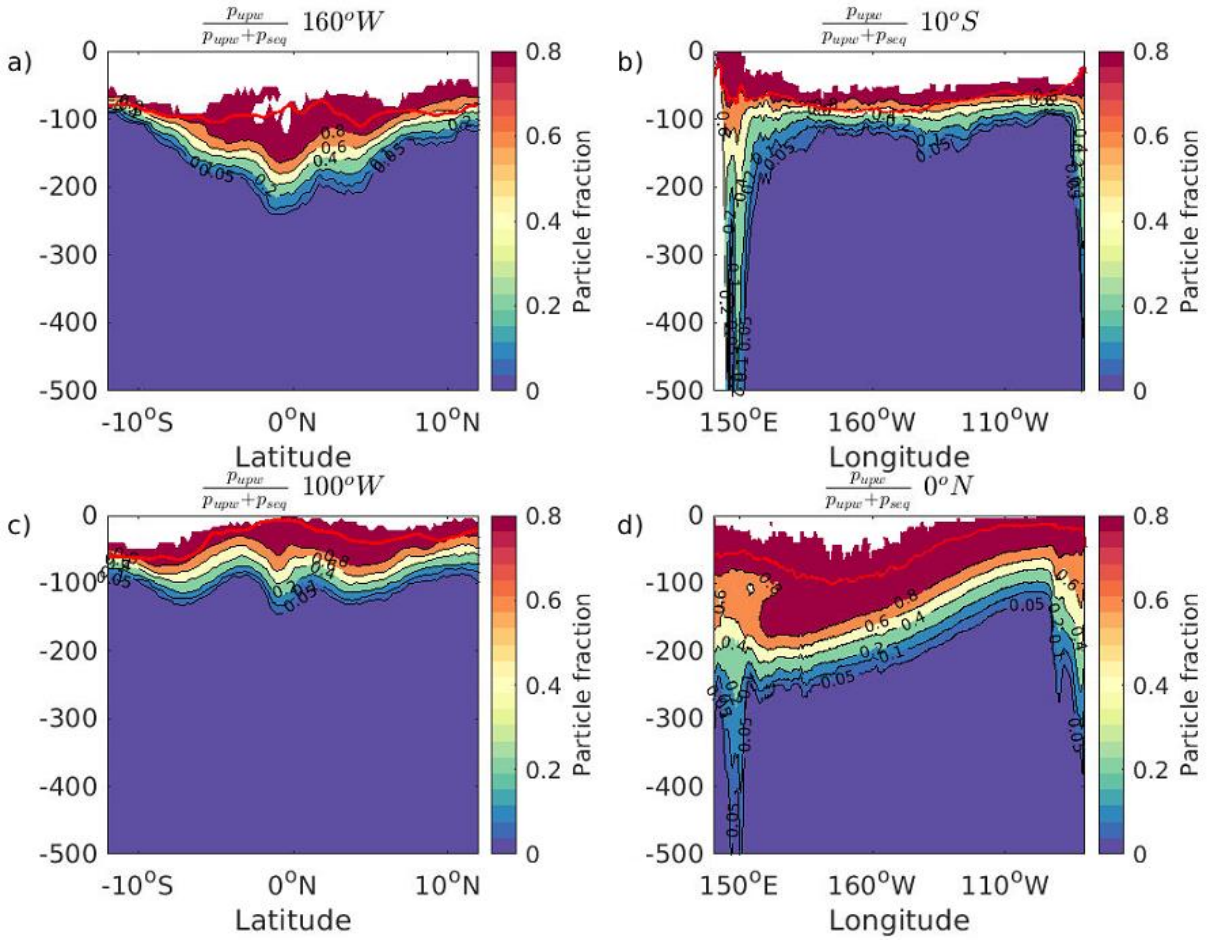

Supplemental Figure 4.3. The fraction of particles that reach the mixed layer in 2 years or less. (a,c) 1-degree zonal averages of $\frac{p_{upw}}{p_{upw}+p_{seq}}$ at 160°W and 100°W and (b,d) 1-degree meridional transects at 10°S and 0°N. p_{upw} at an arbitrary location in the water column is the number of particles that originate there that reach the mixed layer anywhere along their trajectory within two years, while p_{seq} is the number of particles that do not. The fraction $\frac{p_{upw}}{p_{upw}+p_{seq}}$ at any location is therefore the fraction of particles that originate there that are not sequestered for 2 years or longer. The red line in each plot is the annual maximum mixed layer depth.

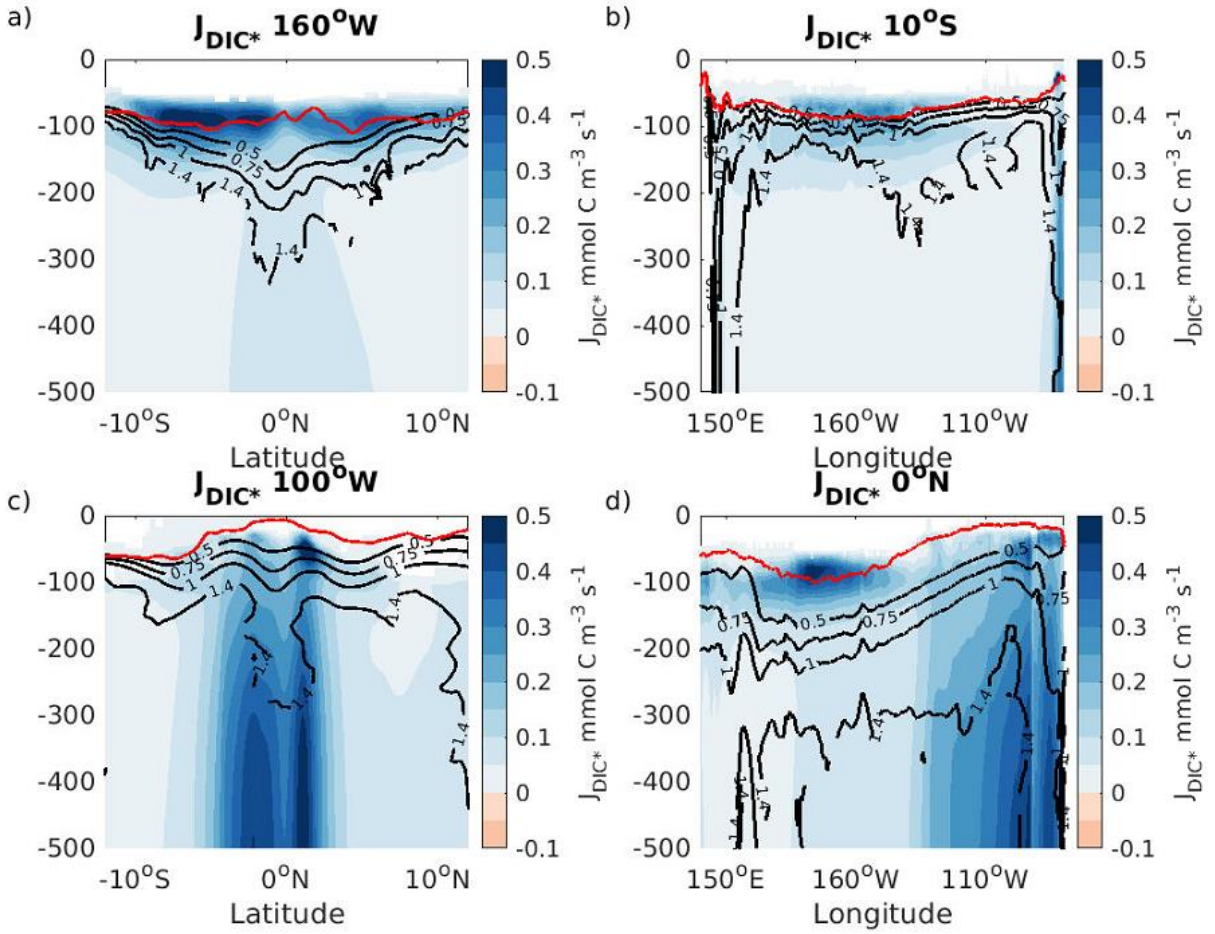

Supplemental Figure 4.4. The rate of net respired carbon production in mol C m^3 s^{-1} (J_{DIC*}, where J_{DIC*} is J_{DIC} in net heterotrophic water). (a,c) 1-degree zonal averages of J_{DIC*} at 160°W and 100°W and (b,d) 1-degree meridional transects at 10°S and 0°N. The red line in each plot is the annual maximum mixed layer depth and the black lines correspond to the τ depth horizons for different sequestration timescales (Figure 4.7).

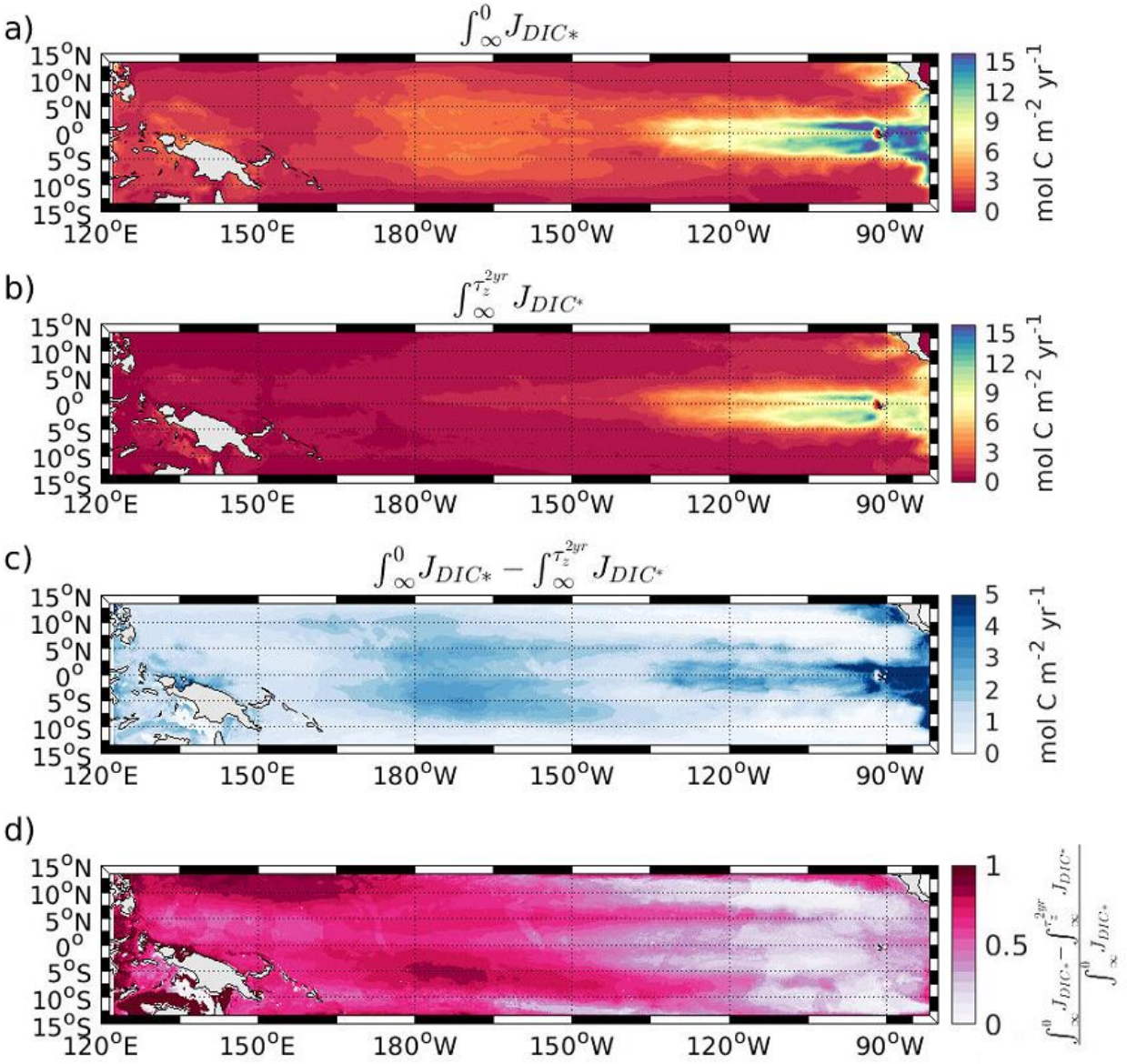

Supplemental Figure 4.5. The relative rate and fraction of respired carbon production below the 2-year sequestration timescale horizon. (a) $\int_{\infty}^{0} J_{DIC^*} dz$, where J_{DIC^*} is defined as J_{DIC} where J_{DIC}<0. (b) J_{DIC^*} integrated below the 2-year sequestration timescale horizon (τ_z^{2yr}). (c) The cumulative column integral of JDIC* above τ_z^{2yr} ($\int_{\infty}^{0} J_{DIC^*} dz$ - $\int_{\infty}^{\tau_z^{2yr}} J_{DIC^*} dz$. (d) The fraction of respired carbon production that occurs above τ_z^{2yr}.

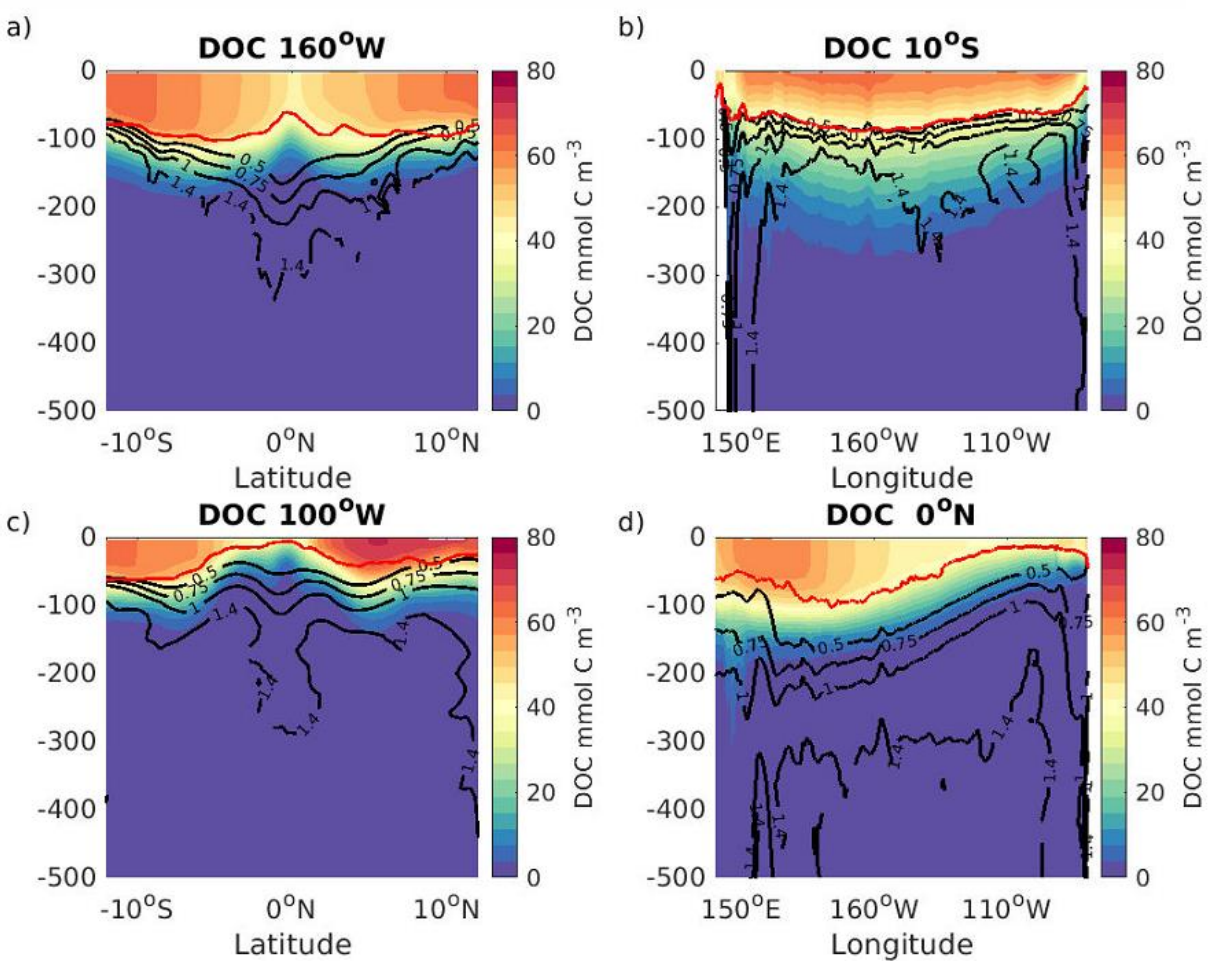

Supplemental Figure 4.6. The distribution of [DOC] in the tropical Pacific in ROMS. (a,c) 1-degree zonal averages of DOC at 160°W and 100°W and (b,d) 1-degree meridional transects at 10°S and 0°N. The red line in each plot is the annual maximum mixed layer depth and the black lines correspond to the τ depth horizons for different sequestration timescales (Figure 4.7).

4.8 Supplemental Discussion

The following equations are the full derivation of Equation 3 in section 4.3 of the text using a 2-box model that represents the full water column in the area from 15°S to 15°N in the tropical Pacific.

Definitions:

$f_{DOC} \equiv$ the fraction of NCP that goes into DOC

h = horizontal; v = vertical; s = surface; d = deep

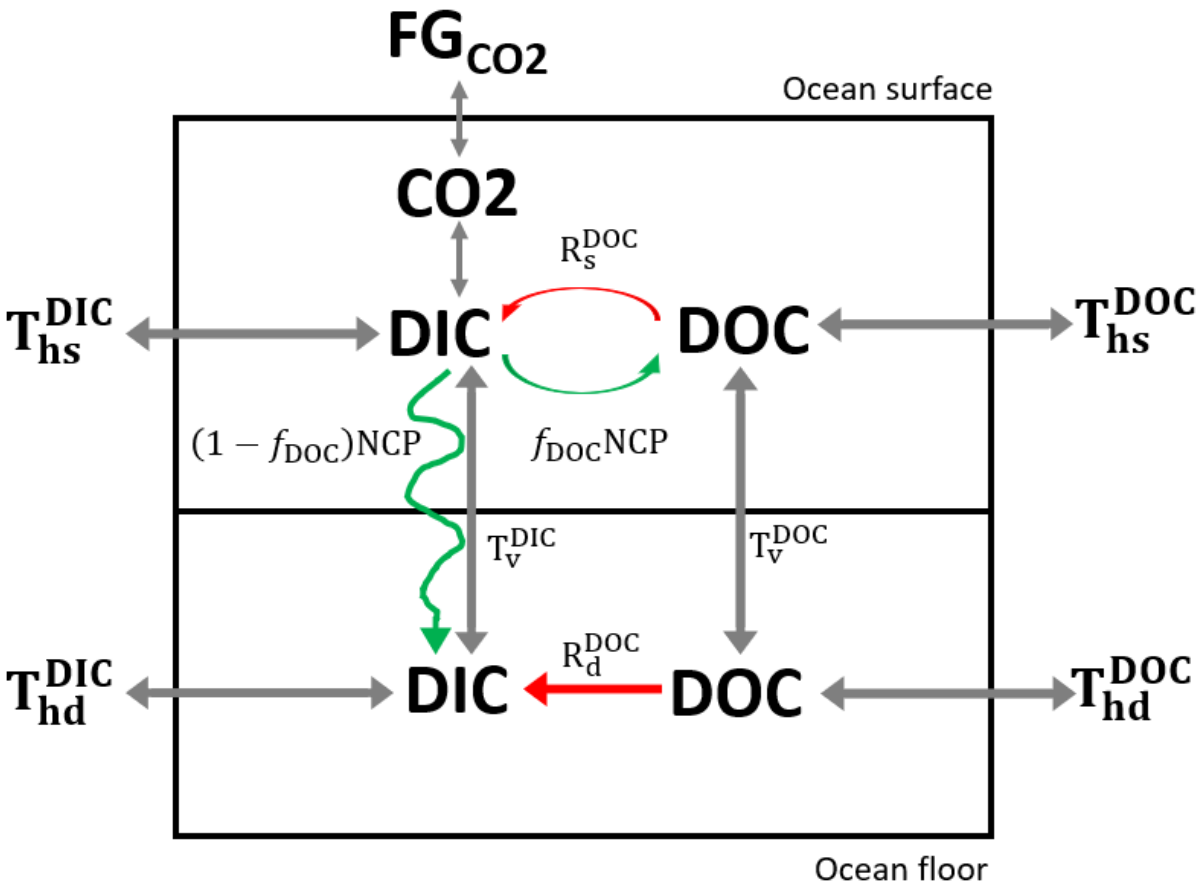

The biotic DIC and DOC mass balance in the surface box:

$$\frac{dDIC_s}{dt} = T_{hs}^{DIC} + T_v^{DIC} - NCP + R_s^{DOC} + FG_{CO2}$$

$$\frac{dDOC_s}{dt} = T_s^{DOC} + T_v^{DOC} + f_{DOC}NCP - R_s^{DOC}$$

The biotic DIC and DOC mass balance in the deep box:

$$\frac{dDIC_d}{dt} = T_{hd}^{DIC} - T_v^{DIC} + (1 - f_{DOC})NCP + R_d^{DOC}$$

$$\frac{dDOC_d}{dt} = T_{hd}^{DOC} - T_v^{DOC} - R_d^{DOC}$$

The biotic DIC and DOC mass balance for the full system (surface+deep):

$$\frac{dDIC}{dt} = \frac{dDIC_d}{dt} + \frac{dDIC_s}{dt}$$

$$= T_{hs}^{DIC} + T_{hd}^{DIC} + \cancel{T_{vd}^{DIC} - T_{vd}^{DIC}} + (\cancel{1} - f_{DOC})NCP - \cancel{NCP} + R_s^{DOC} + FG_{CO2}$$

$$\frac{dDIC}{dt} = T_{hs}^{DIC} + T_{hd}^{DIC} - f_{DOC}NCP + R_s^{DOC} + R_d^{DOC} + FG_{CO2}$$

$$\frac{dDOC}{dt} = \frac{dDOC_d}{dt} + \frac{dDOC_s}{dt} = T_s^{DOC} + T_{hd}^{DOC} \cancel{- T_v^{DOC} + T_v^{DOC}} + f_{DOC}NCP - R_s^{DOC} - R_d^{DOC}$$

$$\frac{dDOC}{dt} = T_{hs}^{DOC} + T_{hd}^{DOC} + f_{DOC}NCP - R_s^{DOC} - R_d^{DOC}$$

The combined biotic carbon mass balance for the full system (surface+deep):

$$\frac{dC}{dt} = \frac{dDOC}{dt} + \frac{dDIC}{dt}$$

$$\frac{dC}{dt} = T_{hs}^{DIC} + T_{hd}^{DIC} + T_{hs}^{DOC} + T_{hd}^{DOC} + FG_{CO2} \cancel{+ f_{DOC}NCP - f_{DOC}NCP} + \cancel{R_s^{DOC} - R_s^{DOC}} + \cancel{R_d^{DOC}} \cancel{- R_d^{DOC}}$$

$$\frac{dC}{dt} = T_{hs}^{DIC} + T_{hd}^{DIC} + T_{hs}^{DOC} + T_{hd}^{DOC} + FG_{CO2}$$

The abiotic DIC and DOC mass balance in the surface box:

$$\frac{dDIC_s}{dt} = T_{hs,abio}^{DIC} + T_{v,abio}^{DIC} + FG_{CO2,abio}$$

$$\frac{dDOC_s}{dt} = T_{hs,abio}^{DOC} + T_{v,abio}^{DOC}$$

The abiotic DIC and DOC mass balance in the deep box:

$$\frac{dDIC_d}{dt} = T_{hd,abio}^{DIC} - T_{v,abio}^{DIC}$$

$$\frac{dDOC_d}{dt} = T_{hd,abio}^{DOC} - T_{v,abio}^{DOC}$$

The combined abiotic carbon mass balance for the full system (surface+deep):

$$\frac{dC_{abio}}{dt} = T_{hs,abio}^{DIC} + T_{hd,abio}^{DIC} + T_{hs,abio}^{DOC} + T_{hd,abio}^{DOC} + FG_{CO2,abio}$$

The difference between the biotic and abiotic full carbon mass balance for the surface+deep:

$$\frac{\Delta dC}{dt} = \frac{dC_{bio}}{dt} - \frac{dC_{abio}}{dt} = \Delta T_{hs}^{DIC} + \Delta T_{hd}^{DIC} + \Delta T_{hs}^{DOC} + \Delta T_{hd}^{DOC} + \Delta FG_{CO2}$$

At steady state, $\frac{\Delta dC}{dt} = 0$

$$\Delta FG_{CO2} = -\Delta T_{hs}^{DIC} - \Delta T_{hd}^{DIC} - \Delta T_{hs}^{DOC} - \Delta T_{hd}^{DOC}$$

In both the biotic and abiotic cases, there is a net supply of DIC to the model domain in the deep ocean and a net transport of DIC out of the surface ocean, so $T_{hs}^{DIC} < 0$ and $T_{hd}^{DIC} > 0$ in both scenarios. Since NCP acts to transfer DIC from the surface to the deep, $T_{hs,bio}^{DIC} > T_{hs,abio}^{DIC}$, which means that $\Delta T_{hs}^{DIC} > 0$. Note that since both $T_{hs,bio}^{DIC}$ and $T_{hs,abio}^{DIC}$ are negative, a positive ΔT_{hs}^{DIC} indicates a net decrease in the outgoing transport of DIC in the surface. The transfer of DIC to the deep also increases the concentration of deep DIC, driving a positive ΔT_{hd}^{DIC} and therefore a net decrease in the incoming transport of DIC in the deep. The fraction of NCP that goes into DOC ($f_{DOC}NCP$) in the surface ocean that is not respired there causes a net increase in the transport of DOC out of the model domain ($\Delta T_{hs}^{DOC} < 0$) and any DOC that is transported to the deep and not respired there increases the outgoing DOC transport in the deep ($\Delta T_{hs}^{DOC} < 0$). Together, the effect of biology on both DOC and DIC decrease the outgoing DIC transport in the surface ocean and convert it into an increase in the outgoing surface transport of DOC and an increase in deep [DIC] that causes a net decrease in the net supply of DIC to the deep via transport. In other words, the change in the transport terms is a tracer of the influence of NCP on the overall system, which can be solved for explicitly in the model via the difference between biotic and abiotic simulations.

We can combine the surface and deep transport terms ($\Delta T_{DIC} = \Delta T_{hs}^{DIC} + \Delta T_{hd}^{DIC}$), which leaves us with Equation 3 from the text.

$$\Delta FG_{CO2} = -\Delta T_{hs}^{DIC} - \Delta T_{hd}^{DIC} - \Delta T_{hs}^{DOC} - \Delta T_{hd}^{DOC} = -\Delta T_{DIC} - \Delta T_{DOC}$$

BIBLIOGRAPHY

Anderson, L. A., & Sarmiento, J. L. (1994). Redfield ratios of remineralization determined by nutrient data analysis. *Global Biogeochemical Cycles*, *8*(1), 65–80. https://doi.org/10.1029/93GB03318

Armstrong, R. A., Lee, C., Hedges, J. I., Honjo, S., & Wakeham, S. G. (2002). A new, mechanistic model for organic carbon fluxes in the ocean based on the quantitative association of POC with ballast minerals. *Deep-Sea Research Part II-Topical Studies in Oceanography*, *49*(1–3), 219–236. (ISI:000173008600010).

Aumont, O., Orr, J. C., Monfray, P., Madec, G., & Maier-Reimer, E. (1999). Nutrient trapping in the equatorial Pacific: The ocean circulation solution. *Global Biogeochemical Cycles*, *13*(2), 351–369. https://doi.org/10.1029/1998GB900012

Behrenfeld, M. J., & Falkowski, P. G. (1997). Photosynthetic rates derived from satellite-based chlorophyll concentration. *Limnology and Oceanography*, *42*(1), 1–20. https://doi.org/10.4319/lo.1997.42.1.0001

Bianchi, D., Dunne, J. P., Sarmiento, J. L., & Galbraith, E. D. (2012). Data-based estimates of suboxia, denitrification, and N_2O production in the ocean and their sensitivities to dissolved O_2: DATA-BASED SUBOXIA AND DENITRIFICATION. *Global Biogeochemical Cycles*, *26*(2), n/a-n/a. https://doi.org/10.1029/2011GB004209

Bjerknes, J. (1964). Atlantic Air-Sea Interaction. In H. E. Landsberg & J. Van Mieghem (Eds.), *Advances in Geophysics* (Vol. 10, pp. 1–82). Elsevier. https://doi.org/10.1016/S0065-2687(08)60005-9

Bopp, L., Resplandy, L., Orr, J. C., Doney, S. C., Dunne, J. P., Gehlen, M., … Vichi, M. (2013). Multiple stressors of ocean ecosystems in the 21st century: projections with CMIP5 models. *Biogeosciences*, *10*(10), 6225–6245. https://doi.org/10.5194/Bg-10-6225-2013

Bopp, L., Resplandy, L., Untersee, A., Le Mezo, P., & Kageyama, M. (2017). Ocean (de)oxygenation from the Last Glacial Maximum to the twenty-first century: Insights from Earth System models. *Philosophical Transactions of the Royal Society A: Mathematical, Physical and Engineering Sciences*, *375*(2102), 20160323. https://doi.org/10.1098/rsta.2016.0323

Boyer, T. P., Antonov, J. I., Baranova, O. K., Coleman, C., Garcia, H. E., Grodsky, A., … Zweng, M. M. (2013). *World Ocean Database 2013*. [Report]. Retrieved from NOAA Printing Office website: https://www.oceanbestpractices.net/handle/11329/357

Boyer, T. P., Baranova, O. K., Coleman, C., Garcia, H. E., Grodsky, A., Locarnini, R. A., Mishonov, A. V., Paver, C. R., Reagan, J. R., Seidov, D., Smolyar, I. V., Weathers, K. W., & Zweng, M. M. (2018). *WORLD OCEAN DATABASE 2018*. 207.

Bushinsky, S. M., & Emerson, S. (2015). Marine biological production from in situ oxygen measurements on a profiling float in the subarctic Pacific Ocean. *Global Biogeochemical Cycles*, *29*(12), 2050–2060. https://doi.org/10.1002/2015GB005251

Cabré, A., Marinov, I., Bernardello, R., & Bianchi, D. (2015). Oxygen minimum zones in the tropical Pacific across CMIP5 models: mean state differences and climate change trends. *Biogeosciences*, *12*(18), 5429–5454. https://doi.org/10.5194/bg-12-5429-2015

Carton, J., & Giese, B. (2008). A reanalysis of ocean climate using Simple Ocean Data Assimilation (SODA). Monthly Weather Review, *136*(8), 2999–3017.

Codispoti, L. A. (2010). Interesting Times for Marine N2O. *Science*, *327*(5971), 1339–1340. https://doi.org/10.1126/Science.1184945

Contreras, R. F. (2002). Long-term observations of tropical instability waves. *Journal of Physical Oceanography*, *32*, 2715–2722.

Cram, J. A., Weber, T., Leung, S. W., McDonnell, A. M. P., Liang, J.-H., & Deutsch, C. (2018). The Role of Particle Size, Ballast, Temperature, and Oxygen in the Sinking Flux to the Deep Sea. Global Biogeochemical Cycles, *32*(5), 858–876. https://doi.org/10.1029/2017GB005710

Cravatte, S., Kestenare, E., Marin, F., Dutrieux, P., & Firing, E. (2017). Subthermocline and Intermediate Zonal Currents in the Tropical Pacific Ocean: Paths and Vertical Structure. *Journal of Physical Oceanography*, *47*(9), 2305–2324. https://doi.org/10.1175/JPO-D-17-0043.1

Deutsch, C., Brix, H., Ito, T., Frenzel, H., & Thompson, L. (2011). Climate-Forced Variability of Ocean Hypoxia. *Science*, *333*(6040), 336–339. https://doi.org/10.1126/science.1202422

Cromwell, T., Montgomery, R. B., & Stroup, E. D. (1954). Equatorial Undercurrent in Pacific Ocean Revealed by New Methods. *Science*, *119*(3097), 648–649. https://doi.org/10.1126/science.119.3097.648

Deutsch, C., Berelson, W., Thunell, R., Weber, T., Tems, C., McManus, J., … van Geen, A. (2014). Centennial changes in North Pacific anoxia linked to tropical trade winds. *Science*, *345*(6197), 665–668. https://doi.org/10.1126/science.1252332

Deutsch, C., Ferrel, A., Seibel, B., Pörtner, H.-O., & Huey, R. B. (2015). Climate change tightens a metabolic constraint on marine habitats. *Science*, *348*(6239), 1132–1135. https://doi.org/10.1126/science.aaa1605

Devol, A. H. (1978). Bacterial oxygen uptake kinetics as related to biological processes in oxygen deficient zones of the oceans. *Deep Sea Research*, *25*(2), 137–146.

DeVries, T., & Primeau, F. (2011). Dynamically and Observationally Constrained Estimates of Water-Mass Distributions and Ages in the Global Ocean. *Journal of Physical Oceanography*, *41*(12), 2381–2401. https://doi.org/10.1175/JPO-D-10-05011.1

DeVries, T., Primeau, F., & Deutsch, C. (2012). The sequestration efficiency of the biological pump. *Geophysical Research Letters*, *39*(13). https://doi.org/10.1029/2012GL051963

DeVries, T., Deutsch, C., Rafter, P. A., & Primeau, F. (2013). Marine denitrification rates determined from a global 3-D inverse model. *Biogeosciences*, *10*(4), 2481–2496. https://doi.org/10.5194/bg-10-2481-2013

DeVries, Tim, & Deutsch, C. (2014). Large-scale variations in the stoichiometry of marine organic matter respiration. *Nature Geoscience*, *7*(12), 890–894. https://doi.org/10.1038/ngeo2300

DeVries, T., Deutsch, C., Primeau, F., Chang, B., & Devol, A. (2012). Global rates of water-column denitrification derived from nitrogen gas measurements. *Nature Geoscience*, *5*(8), 547–550. https://doi.org/10.1038/ngeo1515

Diaz, R. J., & Rosenberg, R. (2008). Spreading Dead Zones and Consequences for Marine Ecosystems. *Science*, *321*(5891), 926–929. https://doi.org/10.1126/science.1156401

Dietze, H., & Loeptien, U. (2013). Revisiting "nutrient trapping" in global coupled biogeochemical ocean circulation models. Global Biogeochemical Cycles, *27*(2), 265–284. https://doi.org/10.1002/gbc.20029

Doney, S. C., Glover, D. M., & Najjar, R. G. (1996). A new coupled, one-dimensional biological-physical model for the upper ocean: Applications to the JGOFS Bermuda Atlantic Time-series Study (BATS) site. *Deep Sea Research Part II: Topical Studies in Oceanography*, *43*(2), 591–624. https://doi.org/10.1016/0967-0645(95)00104-2

Durski, S. M., Barth, J. A., McWilliams, J. C., Frenzel, H., & Deutsch, C. (2017). The influence of variable slope-water characteristics on dissolved oxygen levels in the northern California Current System. *Journal of Geophysical Research: Oceans*, *122*(9), 7674–7697. https://doi.org/10.1002/2017JC013089

Duteil, O., Böning, C. W., & Oschlies, A. (2014). Variability in subtropical-tropical cells drives oxygen levels in the tropical Pacific Ocean: oxygen and subtropical-tropical cells. *Geophysical Research Letters*, *41*(24), 8926–8934. https://doi.org/10.1002/2014GL061774

Duteil, O., Oschlies, A., & Böning, C. W. (2018). Pacific Decadal Oscillation and recent oxygen decline in the eastern tropical Pacific Ocean. *Biogeosciences*, *15*(23), 7111–7126. https://doi.org/10.5194/bg-15-7111-2018

Eddebbar, Y. A., Long, M. C., Resplandy, L., Rödenbeck, C., Rodgers, K. B., Manizza, M., & Keeling, R. F. (2017). Impacts of ENSO on air-sea oxygen exchange: Observations and mechanisms. *Global Biogeochemical Cycles*, *31*(5), 901–921. https://doi.org/10.1002/2017GB005630

Emerson, S. (2014). Annual net community production and the biological carbon flux in the ocean. *Global Biogeochemical Cycles*, *28*(1), 14–28. https://doi.org/10.1002/2013GB004680

Emerson, S., & Stump, C. (2010). Net biological oxygen production in the ocean—II: Remote in situ measurements of O2 and N2 in subarctic pacific surface waters. *Deep Sea Research Part I: Oceanographic Research Papers*, *57*(10), 1255–1265. https://doi.org/10.1016/j.dsr.2010.06.001

Field, C. B., Behrenfeld, M. J., Randerson, J. T., & Falkowski, P. (1998). Primary Production of the Biosphere: Integrating Terrestrial and Oceanic Components. *Science*, *281*(5374), 237–240. https://doi.org/10.1126/science.281.5374.237

Firing, E., Wijffels, S. E., & Hacker, P. (1998). Equatorial subthermocline currents across the Pacific. *Journal of Geophysical Research: Oceans*, *103*(C10), 21413–21423. https://doi.org/10.1029/98JC01944

Frenger, I., Bianchi, D., StühRenberg, C., Oschlies, A., Dunne, J., Deutsch, C., … Schütte, F. (2018). Biogeochemical Role of Subsurface Coherent Eddies in the Ocean: Tracer Cannonballs, Hypoxic Storms, and Microbial Stewpots? *Global Biogeochemical Cycles*, *32*(2), 226–249. https://doi.org/10.1002/2017GB005743

Garcia, H., Locarnini, R. A., Boyer, T. P., & Antonov, J. I. (2014). *World Ocean Atlas 2013, Volume 3: Dissolved Oxygen, Apparent Oxygen Utilization, and Oxygen Saturation* (S. Levitus & A. Mishonov, Eds.). NOAA Atlas NESDIS.

Garcia, H., Locarnini, R. A., Boyer, T. P., Antonov, J. I., Baranova, O. K., Zweng, M. M., & Johnson, D. R. (2010). *World Ocean Atlas 2009 Volume 3: Dissolved Oxygen, Apparent Oxygen Utilization, and Oxygen Saturation* (S. Levitus, Ed.). U.S. Government Printing Office, Washington D.C.

Giering, S. L. C., & Humphreys, M. P. (2018). Biological Pump. In W. M. White (Ed.), *Encyclopedia of Geochemistry: A Comprehensive Reference Source on the Chemistry of the Earth* (pp. 111–116). Springer International Publishing. https://doi.org/10.1007/978-3-319-39312-4_154

Getzlaff, J., & Dietze, H. (2013). Effects of increased isopycnal diffusivity mimicking the unresolved equatorial intermediate current system in an earth system climate model. Geophysical Research Letters, *40*(10), 2166–2170. https://doi.org/10.1002/grl.50419

Gnanadesikan, A., Dunne, J. P., & John, J. (2012). Understanding why the volume of suboxic waters does not increase over centuries of global warming in an Earth System Model. *Biogeosciences*, *9*(3), 1159–1172. https://doi.org/10.5194/bg-9-1159-2012

Gnanadesikan, A., D. Bianchi, & M.-A. Pradal (2013), Critical role for mesoscale eddy diffusion in supplying oxygen to hypoxic ocean waters, *Geophys. Res. Lett.*, 40, 5194–5198. doi:10.1002/grl.50998

Gnanadesikan, A., Dunne, J. P., & John, J. (2012). Understanding why the volume of suboxic waters does not increase over centuries of global warming in an Earth System Model. *Biogeosciences*, *9*(3), 1159–1172. https://doi.org/10.5194/bg-9-1159-2012

Goodman, P. J., Hazeleger, W., Vries, P. de, & Cane, M. (2005). Pathways into the Pacific Equatorial Undercurrent: A Trajectory Analysis. *Journal of Physical Oceanography*, *35*(11), 2134–2151. https://doi.org/10.1175/JPO2825.1

Gruber, N., Clement, D., Carter, B. R., Feely, R. A., van Heuven, S., Hoppema, M., Ishii, M., Key, R. M., Kozyr, A., Lauvset, S. K., Monaco, C. L., Mathis, J. T., Murata, A., Olsen, A., Perez, F. F., Sabine, C. L., Tanhua, T., & Wanninkhof, R. (2019). *The oceanic sink for anthropogenic CO2 from 1994 to 2007*. 8.

Gula, J., Molemaker, M. J., & McWilliams, J. C. (2014). Submesoscale Cold Filaments in the Gulf Stream. *Journal of Physical Oceanography*, *44*(10), 2617–2643. https://doi.org/10.1175/JPO-D-14-0029.1

Heller, M. I., Lam, P. J., Moffett, J. W., Till, C. P., Lee, J.-M., Toner, B. M., & Marcus, M. A. (2017). Accumulation of Fe oxyhydroxides in the Peruvian oxygen deficient zone implies non-oxygen dependent Fe oxidation. *Geochimica et Cosmochimica Acta*, *211*, 174–193. https://doi.org/10.1016/j.gca.2017.05.019

Howard, E. M., Penn, J. L., Frenzel, H., Seibel, B. A., Bianchi, D., Renault, L., Kessouri, F., Sutula, M. A., McWilliams, J. C., & Deutsch, C. (2020). Climate-driven aerobic habitat loss in the California Current System. *Science Advances*, *6*(20), eaay3188. https://doi.org/10.1126/sciadv.aay3188

Hurrell, J. W., Kushnir, Y., Ottersen, G., & Visbeck, M. (Eds.). (2003). *The North Atlantic Oscillation: Climatic Significance and Environmental Impact* (Vol. 134). American Geophysical Union. https://doi.org/10.1029/GM134

Ishii, M., Feely, R. A., Rodgers, K. B., Park, G.-H., Wanninkhof, R., Sasano, D., Sugimoto, H., Cosca, C. E., Nakaoka, S., Telszewski, M., Nojiri, Y., Mikaloff Fletcher, S. E., Niwa, Y., Patra, P. K., Valsala, V., Nakano, H., Lima, I., Doney, S. C., Buitenhuis, E. T., … Takahashi, T. (2014). Air–sea CO₂ flux in the Pacific Ocean for the period 1990–2009. *Biogeosciences*, *11*(3), 709–734. https://doi.org/10.5194/bg-11-709-2014

Ito, T., Follows, M. J., & Boyle, E. A. (2004). Is AOU a good measure of respiration in the oceans? *Geophysical Research Letters*, *31*(17). https://doi.org/10.1029/2004GL020900

Ito, T., & Deutsch, C. (2013). Variability of the oxygen minimum zone in the tropical North Pacific during the late twentieth century: VARIABILITY OF TROPICAL PACIFIC OMZ. *Global Biogeochemical Cycles*, *27*(4), 1119–1128. https://doi.org/10.1002/2013GB004567

Ito, T., Minobe, S., Long, M. C., & Deutsch, C. (2017). Upper ocean O2 trends: 1958–2015. *Geophysical Research Letters*, *44*(9), 4214–4223. https://doi.org/10.1002/2017GL073613

Ito, T., Long, M. C., Deutsch, C., Minobe, S., & Sun, D. (2019). Mechanisms of Low-Frequency Oxygen Variability in the North Pacific. *Global Biogeochemical Cycles*, *33*(2), 110–124. https://doi.org/10.1029/2018GB005987

Jochum, M., & Murtugudde, R. (2006). Temperature Advection by Tropical Instability Waves. *Journal of Physical Oceanography*, *36*(4), 592–605. https://doi.org/10.1175/JPO2870.1

Kalvelage, T., Jensen, M. M., Contreras, S., Revsbech, N. P., Lam, P., Günter, M., … Kuypers, M. M. M. (2011). Oxygen Sensitivity of Anammox and Coupled N-Cycle Processes in Oxygen Minimum Zones. *PLoS ONE*, *6*(12), e29299. https://doi.org/10.1371/journal.pone.0029299

Karstensen, Johannes, Stramma, L., & Visbeck, M. (2008). Oxygen minimum zones in the eastern tropical Atlantic and Pacific oceans. *Progress in Oceanography*, *77*(4), 331–350. https://doi.org/10.1016/j.pocean.2007.05.009

Keeling, R. F., Körtzinger, A., & Gruber, N. (2009). Ocean Deoxygenation in a Warming World. *Annual Review of Marine Science*, *2*(1), 199–229. https://doi.org/10.1146/annurev.marine.010908.163855

Kessler, W. S. (2006). The circulation of the eastern tropical Pacific: A review. Progress in Oceanography, *69*(2–4), 181–217. https://doi.org/10.1016/j.pocean.2006.03.009

Kondo, Y., & Moffett, J. W. (2013). Dissolved Fe(II) in the Arabian Sea oxygen minimum zone and western tropical Indian Ocean during the inter-monsoon period. *Deep Sea Research Part I: Oceanographic Research Papers*, *73*, 73–83. https://doi.org/10.1016/j.dsr.2012.11.014

Körtzinger, A., Hedges, J. I., & Quay, P. D. (2001). Redfield ratios revisited: Removing the biasing effect of anthropogenic CO2. *Limnology and Oceanography*, *46*(4), 964–970. https://doi.org/10.4319/lo.2001.46.4.0964

Körtzinger, A., Send, U., Lampitt, R. S., Hartman, S., Wallace, D. W. R., Karstensen, J., Villagarcia, M. G., Llinás, O., & DeGrandpre, M. D. (2008). The seasonal p CO_2 cycle at 49°N/16.5°W in the northeastern Atlantic Ocean and what it tells us about biological productivity. *Journal of Geophysical Research*, *113*(C4), C04020. https://doi.org/10.1029/2007JC004347

Laffoley, D., & Baxter, J. M. (Eds.). (2019). *Ocean deoxygenation: Everyone's problem. Causes, impacts, consequences and solutions*. IUCN, International Union for Conservation of Nature. https://doi.org/10.2305/IUCN.CH.2019.13.en

Lam, P., Lavik, G., Jensen, M. M., van de Vossenberg, J., Schmid, M., Woebken, D., … Kuypers, M. M. M. (2009). Revising the nitrogen cycle in the Peruvian oxygen minimum zone. *Proceedings of the National Academy of Sciences of the United States of America*, *106*(12), 4752–4757. https://doi.org/10.1073/pnas.0812444106

Landry, M., Constantinou, J., Latasa, M., Brown, S., Bidigare, R., & Ondrusek, M. (2000). Biological response to iron fertilization in the eastern equatorial Pacific (IronEx II). III. Dynamics of phytoplankton growth and microzooplankton grazing. *Marine Ecology Progress Series*, *201*, 57–72. https://doi.org/10.3354/meps201057

Large, W. G., & Yeager, S. (2004). *Diurnal to decadal global forcing for ocean and sea-ice models: the data sets and flux climatologies. TN-460+STR*.

Large, William G., Danabasoglu, G., Doney, S. C., & McWilliams, J. C. (1997). Sensitivity to Surface Forcing and Boundary Layer Mixing in a Global Ocean Model: Annual-Mean Climatology. *Journal of Physical Oceanography*, *27*(11), 2418–2447. https://doi.org/10.1175/1520-0485(1997)027<2418:STSFAB>2.0.CO;2

Laufkötter, C., Vogt, M., Gruber, N., Aumont, O., Bopp, L., Doney, S. C., Dunne, J. P., Hauck, J., John, J. G., Lima, I. D., Seferian, R., & Völker, C. (2016). Projected decreases in future marine export production: The role of the carbon flux through the upper ocean ecosystem. *Biogeosciences*, *13*(13), 4023–4047. https://doi.org/10.5194/bg-13-4023-2016

Li, G., Cheng, L., Zhu, J., Trenberth, K. E., Mann, M. E., & Abraham, J. P. (2020). Increasing ocean stratification over the past half-century. *Nature Climate Change*, *10*(12), 1116–1123. https://doi.org/10.1038/s41558-020-00918-2

Liu, W., Fedorov, A. V., Xie, S.-P., & Hu, S. (2020). Climate impacts of a weakened Atlantic Meridional Overturning Circulation in a warming climate. *Science Advances*, *6*(26), eaaz4876. https://doi.org/10.1126/sciadv.aaz4876

Liu, Z., Philander, S. G. H., & Pacanowski, R. C. (1994). A GCM Study of Tropical–Subtropical Upper-Ocean Water Exchange. *Journal of Physical Oceanography*, *24*(12), 2606–2623. https://doi.org/10.1175/1520-0485(1994)024<2606:AGSOTU>2.0.CO;2

Long, M. C., Ito, T., & Deutsch, C. (2019). Oxygen projections for the future. In *Ocean deoxygenation: Everyone's problem. Causes, impacts, consequences and solutions* (pp. 171–211). 10.2305/IUCN.CH.2019.13.en

Martiny, A. C., Pham, C.T.A., Primeau, F.W., Vrugt, J.A., Moore, J.K., Levin, S.A. & Lomas, M.W. (2013). Strong latitudinal patterns in the elemental ratios of marine plankton and organic matter. *Nature Geoscience*, 6**,** 279-283.

Matear, R. J., & Hirst, A. C. (2003). Long-term changes in dissolved oxygen concentrations in the ocean caused by protracted global warming. *Global Biogeochemical Cycles*, *17*(4). https://doi.org/10.1029/2002GB001997

Mignot, A., Ferrari, R., & Claustre, H. (2018). Floats with bio-optical sensors reveal what processes trigger the North Atlantic bloom. *Nature Communications*, *9*(1), 190. https://doi.org/10.1038/s41467-017-02143-6

Moore, J. K., Doney, S. C., & Lindsay, K. (2004). Upper ocean ecosystem dynamics and iron cycling in a global three-dimensional model: GLOBAL ECOSYSTEM-BIOGEOCHEMICAL MODEL. Global Biogeochemical Cycles, *18*(4), n/a-n/a. https://doi.org/10.1029/2004GB002220

Oschlies, A., Duteil, O., Getzlaff, J., Koeve, W., Landolfi, A., & Schmidtko, S. (2017). Patterns of deoxygenation: Sensitivity to natural and anthropogenic drivers. *Philosophical Transactions. Series A, Mathematical, Physical, and Engineering Sciences*, *375*(2102). https://doi.org/10.1098/rsta.2016.0325

Palevsky, H. I., & Doney, S. C. (2018). How Choice of Depth Horizon Influences the Estimated Spatial Patterns and Global Magnitude of Ocean Carbon Export Flux. *Geophysical Research Letters*, *45*(9), 4171–4179. https://doi.org/10.1029/2017GL076498

Palevsky, H. I., & Doney, S. C. (2021). Sensitivity of 21st Century Ocean Carbon Export Flux Projections to the Choice of Export Depth Horizon. *Global Biogeochemical Cycles*, *35*(2), e2020GB006790. https://doi.org/10.1029/2020GB006790

Palevsky, H. I., Quay, P. D., & Nicholson, D. P. (2016). Discrepant estimates of primary and export production from satellite algorithms, a biogeochemical model, and geochemical tracer measurements in the North Pacific Ocean. *Geophysical Research Letters*, *43*(16), 8645–8653. https://doi.org/10.1002/2016GL070226

Paulmier, A., & Ruiz-Pino, D. (2009). Oxygen minimum zones (OMZs) in the modern ocean. *Progress in Oceanography*, *80*(3–4), 113–128. https://doi.org/10.1016/j.pocean.2008.08.001

Penn, J., Weber, T., & Deutsch, C. (2016). Microbial functional diversity alters the structure and sensitivity of oxygen deficient zones. *Geophysical Research Letters*, *43*(18), 9773–9780. https://doi.org/10.1002/2016GL070438

Penn, J. P., T. S. Weber, B. X. Chang, C. Deutsch (2019). Microbial ecosystem dynamics drive fluctuating nitrogen loss in marine anoxic zones. *PNAS. 201818014, doi:10.1073/pnas.1818014116*.

Qiu, B., Chen, S., & Sasaki, H. (2013). Generation of the North Equatorial Undercurrent Jets by Triad Baroclinic Rossby Wave Interactions. *Journal of Physical Oceanography*, *43*(12), 2682–2698. https://doi.org/10.1175/JPO-D-13-099.1

Quay, P. (1997). Was a carbon balance measured in the equatorial Pacific during JGOFS? *Deep Sea Research Part II: Topical Studies in Oceanography*, *44*, 1765–1781. https://doi.org/10.1016/S0967-0645(97)00093-3

Quay, P., Emerson, S., & Palevsky, H. (2020). Regional Pattern of the Ocean's Biological Pump Based on Geochemical Observations. *Geophysical Research Letters*, *47*(14), e2020GL088098. https://doi.org/10.1029/2020GL088098

Rafter, P. A., & Sigman, D. M. (2016). Spatial distribution and temporal variation of nitrate nitrogen and oxygen isotopes in the upper equatorial Pacific Ocean. *Limnology and Oceanography*, *61*(1), 14–31. https://doi.org/10.1002/lno.10152

Rafter, P. A., Sigman, D. M., & Mackey, K. R. M. (2017). Recycled iron fuels new production in the eastern equatorial Pacific Ocean. *Nature Communications*, *8*(1), 1100. https://doi.org/10.1038/s41467-017-01219-7

Ray, S., Wittenberg, A. T., Griffies, S. M., & Zeng, F. (2018). Understanding the Equatorial Pacific Cold Tongue Time-Mean Heat Budget. Part I: Diagnostic Framework. *Journal of Climate*, *31*(24), 9965–9985. https://doi.org/10.1175/JCLI-D-18-0152.1

Renault, L., Deutsch, C., McWilliams, J. C., Frenzel, H., Liang, J.-H., & Colas, F. (2016). Partial decoupling of primary productivity from upwelling in the California Current system. *Nature Geoscience*, *9*(7), 505–508. https://doi.org/10.1038/ngeo2722

Risien, C. M., & Chelton, D. B. (2008). A Global Climatology of Surface Wind and Wind Stress Fields from Eight Years of QuikSCAT Scatterometer Data. *Journal of Physical Oceanography*, *38*(11), 2379–2413. https://doi.org/10.1175/2008JPO3881.1

Rodgers, K. B., Blanke, B., Madec, G., Aumont, O., Ciais, P., & Dutay, J.-C. (2003). Extratropical sources of Equatorial Pacific upwelling in an OGCM: EQUATORIAL PACIFIC UPWELLING SOURCES. *Geophysical Research Letters*, *30*(2). https://doi.org/10.1029/2002GL016003

Rosales Quintana, G. M., Marsh, R., & Icochea Salas, L. A. (2021). Interannual variability in contributions of the Equatorial Undercurrent (EUC) to Peruvian upwelling source water. *Ocean Science*, *17*(5), 1385–1402. https://doi.org/10.5194/os-17-1385-2021Renault, L., Deutsch, C., McWilliams, J. C., Frenzel, H., Liang, J.-H., & Colas, F. (2016). Partial decoupling of primary productivity from upwelling in the California Current system. *Nature Geosci*, *9*(7), 505–508. https://doi.org/10.1038/ngeo2722

Sabine, C. L., Feely, R. A., Gruber, N., Key, R. M., Lee, K., Bullister, J. L., Wanninkhof, R., Wong, C. S., Wallace, D. W. R., Tilbrook, B., Millero, F. J., Peng, T.-H., Kozyr, A., Ono, T., & Rios, A. F. (2004). *The Oceanic Sink for Anthropogenic CO2*. *305*, 6.

Saito, M. A., McIlvin, M. R., Moran, D. M., Goepfert, T. J., DiTullio, G. R., Post, A. F., & Lamborg, C. H. (2014). Multiple nutrient stresses at intersecting Pacific Ocean biomes detected by protein biomarkers. *Science*, *345*(6201), 1173–1177. https://doi.org/10.1126/science.1256450

Schmidtko, S., Stramma, L., & Visbeck, M. (2017). Decline in global oceanic oxygen content during the past five decades. *Nature*, *542*(7641), 335–339. https://doi.org/10.1038/nature21399

Seshadri, V. (1999). *The inverse Gaussian distribution : statistical theory and applications*. *Springer*, *New York*.

Shchepetkin, A. F., & McWilliams, J. C. (2005). The regional oceanic modeling system (ROMS): a split-explicit, free-surface, topography-following-coordinate oceanic model. *Ocean Modelling*, *9*(4), 347–404. (ISI:000228343700003).

Stanley, R. H. R., Kirkpatrick, J. B., Cassar, N., Barnett, B. A., & Bender, M. L. (2010). Net community production and gross primary production rates in the western equatorial Pacific. *Global Biogeochemical Cycles*, *24*(4). https://doi.org/10.1029/2009GB003651

Stendardo, I., & Gruber, N. (2012). Oxygen trends over five decades in the North Atlantic. *Journal of Geophysical Research: Oceans*, *117*(C11). https://doi.org/10.1029/2012JC007909

Stramma, L., Johnson, G. C., Sprintall, J., & Mohrholz, V. (2008). Expanding Oxygen-Minimum Zones in the Tropical Oceans. *Science*, *320*(5876), 655–658. https://doi.org/10.1126/science.1153847

Stramma, L., Schmidtko, S., Levin, L. A., & Johnson, G. C. (2010). Ocean oxygen minima expansions and their biological impacts. *Deep Sea Research Part I: Oceanographic Research Papers*, *57*(4), 587–595. https://doi.org/10.1016/j.dsr.2010.01.005

Sverdrup, H. U. (1953). On Conditions for the Vernal Blooming of Phytoplankton. *ICES Journal of Marine Science*, *18*(3), 287–295. https://doi.org/10.1093/icesjms/18.3.287

Tagliabue, A., Aumont, O., DeAth, R., Dunne, J. P., Dutkiewicz, S., Galbraith, E., Misumi, K., Moore, J. K., Ridgwell, A., Sherman, E., Stock, C., Vichi, M., Völker, C., & Yool, A. (2016). How well do global ocean biogeochemistry models simulate dissolved iron distributions? *Global Biogeochemical Cycles*, *30*(2), 149–174. https://doi.org/10.1002/2015GB005289

Takahashi, T., Broecker, W. S., & Langer, S. (1985). Redfield ratio based on chemical data from isopycnal surfaces. *Journal of Geophysical Research: Oceans*, *90*(C4), 6907–6924. https://doi.org/10.1029/JC090iC04p06907

Takano, Y., Ito, T., & Deutsch, C. (2018). Projected Centennial Oxygen Trends and Their Attribution to Distinct Ocean Climate Forcings. *Global Biogeochemical Cycles*, *0*(0). https://doi.org/10.1029/2018GB005939

Taylor, K.E., Stouffer, R.J., & Meehl, G.A. (2012). An Overview of CMIP5 and the experiment design. *Bulletin of the American Meteorological Society*, 93, 485-498, doi:10.1175/BAMS-D-11-00094.1

Toggweiler, J. R., Dixon, K., & Broecker, W. S. (1991). The Peru Upwelling and the Ventilation of the South-Pacific Thermocline. *Journal of Geophysical Research-Oceans*, *96*(C11), 20467–20497. (ISI:A1991GQ69300008).

Tsuchiya, M. (1975). Subsurface countercurrents in the eastern equatorial Pacific. *Journal of Marine Research*, *33*(Suppl.), 145–175.

Van Mooy, B., MacGregor, B., Hollander, D., Nealson, K., & Stahl, D. (2001). Evidence for tight coupling between active bacteria and particulate organic carbon during seasonal stratification of Lake Michigan. *Limnology and Oceanography*, *46*(5), 1202–1208. https://doi.org/10.4319/lo.2001.46.5.1202

Vergara, O., Dewitte, B., Montes, I., Garçon, V., Ramos, M., Paulmier, A., & Pizarro, O. (2016). Seasonal variability of the oxygen minimum zone off Peru in ahigh-resolution regional coupled model. *Biogeosciences*, *13*(15), 4389–4410. https://doi.org/10.5194/bg-13-4389-2016

Wang, Q., Wang, F., Feng, J., Hu, S., Zhang, L., Jia, F., & Hu, D. (2019). The Equatorial Undercurrent and Its Origin in the Region Between Mindanao and New Guinea. *Journal of Geophysical Research: Oceans*, *124*(4), 2313–2330. https://doi.org/10.1029/2018JC014842

Ward, B. B., Devol, A. H., Rich, J. J., Chang, B. X., Bulow, S. E., Naik, H., Pratihary, A., and Jayakumar, A. (2009), Denitrification as the dominant nitrogen loss process in the Arabian Sea, *Nature*, *461*,78– 81.

Westberry, T., Behrenfeld, M. J., Siegel, D. A., & Boss, E. (2008). Carbon-based primary productivity modeling with vertically resolved photoacclimation: CARBON-BASED

PRODUCTION MODEL. *Global Biogeochemical Cycles*, *22*(2), n/a-n/a. https://doi.org/10.1029/2007GB003078

Westberry, T. K., Williams, P. J. le B., & Behrenfeld, M. J. (2012). Global net community production and the putative net heterotrophy of the oligotrophic oceans. *Global Biogeochemical Cycles*, *26*(4). https://doi.org/10.1029/2011GB004094

Whitworth III, T., Warren, B. A., Nowlin, J., W. D., Rutz, S. B., Pillsbury, R. D., & Moore, M. I. (1999). On the deep western-boundary current in the Southwest Pacific Basin. *Progress in Oceanography*, *43*(1), 1–54. https://doi.org/10.1016/S0079-6611(99)00005-1

Williams, R. G., McDonagh, E., Roussenov, V. M., Torres-Valdes, S., King, B., Sanders, R., & Hansell, D. A. (2011). Nutrient streams in the North Atlantic: Advective pathways of inorganic and dissolved organic nutrients. *Global Biogeochemical Cycles*, *25*(4). https://doi.org/10.1029/2010GB003853

Wishner, K. F., Seibel, B. A., Roman, C., Deutsch, C., Outram, D., Shaw, C. T., … Riley, S. (2018). Ocean deoxygenation and zooplankton: Very small oxygen differences matter. *Science Advances*, *4*(12), eaau5180. https://doi.org/10.1126/sciadv.aau5180

Wyrtki, K., (1964). Upwelling in the Costa Rica Dome. *Fishery Bulletin, 63,* 355-372.

Visbeck, M. H., Hurrell, J. W., Polvani, L., & Cullen, H. M. (2001). The North Atlantic Oscillation: Past, present, and future. *Proceedings of the National Academy of Sciences*, *98*(23), 12876–12877. https://doi.org/10.1073/pnas.231391598

Yeager, S., & Large, W. (2008). *CORE.2 Global Air-Sea Flux Dataset* [Data set]. UCAR/NCAR - Research Data Archive. https://doi.org/10.5065/D6WH2N0S

Yeager, S. G., Danabasoglu, G., Rosenbloom, N. A., Strand, W., Bates, S. C., Meehl, G. A., Karspeck, A. R., Lindsay, K., Long, M. C., Teng, H., & Lovenduski, N. S. (2018). Predicting Near-Term Changes in the Earth System: A Large Ensemble of Initialized Decadal Prediction Simulations Using the Community Earth System Model. *Bulletin of the American Meteorological Society*, *99*(9), 1867–1886. https://doi.org/10.1175/BAMS-D-17-0098.1